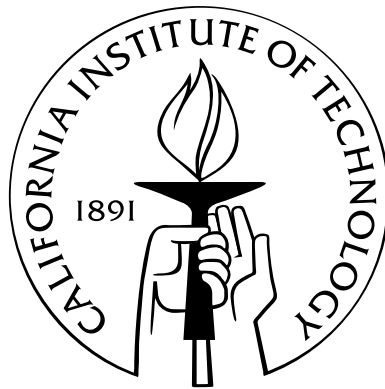


Orbital Dynamics of Kuiper Belt Object Satellites, a Kuiper Belt Family, and Extra-Solar Planet Interiors

Thesis by
Darin Alan Ragozzine

In Partial Fulfillment of the Requirements
for the Degree of
Doctor of Philosophy



California Institute of Technology
Pasadena, California

2009
(Defended May 15, 2009)

To Sarah, Chloe, and Abigail – more important than any thesis

Acknowledgements

This thesis would not have been possible without the help and support from many others.

For the last four years, I have enjoyed the companionship and constant encouragement of my wife, Sarah. I appreciate her companionship immensely. I am so grateful for her willingness to support and celebrate my desire to be a scientist. To her and to my two beautiful daughters, Chloe and Abigail, I have dedicated this thesis.

There is no way to adequately thank my family, particularly my mother and father, for the years of selfless support that have given me. Having my own children has enlightened my understanding of their tens of thousands of hours of loving service rendered on my behalf. Throughout my early years, my family was instrumental in developing my abilities in mathematics and science. I feel that my father, Alan, knew this day would come (when I would receive a doctorate) long before I did, and has helped to prepare me in any way he could. My mother, Kayleen, has always sought my best interests, often at great sacrifice to herself. Mom and Dad: Thank you.

I consider myself very lucky to have had Mike Brown as my advisor. For the rest of my life, I will be grateful for his ideas, guidance, advice, help, and support for these past five years. Not all advisors are as accommodating as he has been; Chapter 2 of this thesis is a testament to his willingness to let me work on other projects. From him, I have learned many aspects of how to be a good scientist. Discussions with and classes from Oded Aharonson, Geoff Blake, Re'em Sari, Dave Stevenson, and Jack Wisdom have also been very helpful. Watching them has helped me to broaden my understanding and has improved the way I approach difficult scientific problems.

I could not have asked for better office-mates than I have had here in South Mudd 154. I will miss greatly the friendship of Margarita Marinova, Kaveh Pahlevan, Alejandro Soto, and Aaron Wolf. From impromptu conversations on a variety of subjects to helpful scientific advice, from social gatherings to intimate conversations, they are what I will remember the most about my time in grad school. I particularly thank Aaron for asking me about how to determine the J_2 of extra-solar planets which resulted in Chapter 2 of this thesis.

Throughout my time here, I have enjoyed working with many students in planetary science and other fields. In particular, other students in Mike's research group have given me many bits of inspiration, advice, and interesting science over the years. I have enjoyed collaborating with and

learning from Kris Barkume and Emily Schaller, as well as many helpful discussions with Meg Schwamb. Outside of Caltech, I would like to thank Dan Fabrycky at the Center for Astrophysics for motivation and many helpful discussions.

One huge advantage of studying planetary science at Caltech, as opposed to other universities, is that the students worry much less about the source of their salaries and research funding. Even so, I most gratefully acknowledge the support of the Moore Foundation and the NASA Earth and Space Sciences Fellowship Program for their significant financial contributions to my graduate career.

Another advantage of studying planetary science at Caltech is our excellent support staff. I would like to thank the Planetary Science Office Staff (particularly Irma Black and Alexandra Tigno) and the technical support staff (particularly Mike Black and Scott Dungan) for their efforts on my behalf. Overall my experience at Caltech has been very positive, partly thanks to kind administrators.

I would like to thank the astronomical community for tools that have made this research possible. In particular, I would like to mention the Astrophysics Data System, the Hubble Space Telescope, the Keck Observatories, the Gemini Observatories, and Caltech's Palomar Observatories. They provide the information needed to move planetary science forward.

Finally, I would like to thank my Heavenly Father for His inspiration, guidance, and love. Concerning this thesis, I would like to thank Him for making Haumea so interesting. From Him I hope to learn the full truths of planetary science someday.

Abstract

This thesis discusses research into four different orbital dynamics problems, where the main goal of each chapter is to characterize the strongest non-Keplerian effect. These problems are introduced and discussed in Chapter 1, to help provide context for the subsequent chapters. In Chapter 2, I discuss a new technique for probing the interior density distributions of extra-solar planets by observing apsidal precession. Using a detailed theoretical and observational model of this precession, I conclude that NASA's *Kepler* mission will be able to detect the presence or absence of a massive core in very hot Jupiters with eccentricities greater than ~ 0.003 . The remaining chapters discuss the orbital dynamics of Kuiper belt objects (KBOs) orbiting the Sun beyond Neptune. The family of dwarf planet Haumea (2003 EL61) is characterized in Chapter 3, including a list of candidate family members sorted by dynamical proximity. Using a numerical integration of resonance diffusion, I also show that the Haumea family is at least 1 Gyr old and is probably primordial. In Chapter 4, I analyze and fit astrometric data for the two satellites of Haumea (Hi'iaka and Namaka) to determine their orbital properties and the masses of Haumea and Hi'iaka. The implications of the new orbital solution are discussed, including the exciting conclusion that Haumea and Namaka are currently starting a season of mutual events. A more general investigation of the orbital and tidal evolution of KBO binaries is given in Chapter 5. A new orbital evolution model is described that accounts for perturbations from the Sun, self-consistent tidal evolution, and non-hydrostatic quadrupoles of solid KBOs. Using this model, I find that the orbital parameters of KBO binaries may have been modified significantly over the age of the solar system. Applied to the Orcus-Vanth binary, this model shows that a short-period circular orbit does not necessarily imply a collisional formation. In all, the work in this thesis has sought to analyze observational data by using the theoretical tools of orbital dynamics.

Contents

Acknowledgements	iv
Abstract	vi
List of Figures	4
List of Tables	5
1 Introduction	6
1.1 Chapter 2: Extra-Solar Planet Interiors	7
1.2 Chapter 3: The Haumea Family	9
1.3 Chapter 4: The Satellites of Haumea	12
1.4 Chapter 5: The Changing Orbits of Kuiper Belt Binaries	14
2 Probing the Interiors of Very Hot Jupiters Using Transit Light Curves	20
Abstract	21
2.1 Introduction	22
2.2 Background Theory	23
2.2.1 Coordinate System and Notation	23
2.2.2 Rotational and Tidal Potentials	24
2.2.2.1 Induced External Gravity Field	26
2.2.3 Apsidal Precession	27
2.2.3.1 Precession Induced by Tidal Bulges	27
2.2.3.2 Precession Induced by Rotational Bulges	29
2.2.3.3 Total Apsidal Precession	29
2.2.4 Modification of the Mean Motion	33
2.2.5 Expectations for Planetary Eccentricities	33
2.3 Transit Light Curves of Apsidal Precession	35
2.3.1 Our Transit Light Curve Model	36

2.3.2	Accuracy of k_{2p} Measurement	37
2.3.3	Comparison to Expected Signal	41
2.3.4	Results for Specific Planets	45
2.4	Potential Confusion of the Apsidal Precession Signal	51
2.4.1	Testing the Effect of Obliquity	51
2.4.2	Transit Timing due to Orbital Decay	52
2.4.3	Confusion Due to Other Planets	54
2.5	Other Methods for Determining k_{2p}	55
2.5.1	Secular Evolution of a Two Planet System	55
2.5.2	Direct Detection of Planetary Asphericity	56
2.6	Conclusions	57
3	Candidates and Age of the Family of Kuiper Belt Object 2003 EL61	65
	Abstract	66
3.1	Introduction	67
3.2	Dynamics	67
3.2.1	Differences between KBO and Asteroid Families	67
3.2.2	Determining Δv	68
3.3	Potential Family Members	70
3.3.1	Collision Center	70
3.3.2	Non-resonant KBOs	70
3.3.3	Resonant KBOs	73
3.4	Age of the Family	76
3.4.1	Diffusion Time of 2003 EL61	76
3.4.2	Diffusion Time of Other Resonant Family Members	77
3.4.3	Future Age Estimates	78
3.5	Discussion	79
4	Orbits and Masses of the Satellites of Dwarf Planet Haumea (2003 EL61)	88
	Abstract	89
4.1	Introduction	90
4.2	Observations and Data Reduction	91
4.3	Orbit Fitting and Results	95
4.3.1	Three Point-Mass Model	96
4.3.2	Including the J_2 of Haumea	100
4.4	Implications of Orbital Solutions	101

4.4.1	Mutual Events and Satellite Sizes	101
4.4.2	Long-term Orbital Integrations	102
4.4.3	Tidal Evolution	103
4.4.3.1	Tidal Evolution of Semi-major Axes	104
4.4.3.2	Tidal Evolution of Eccentricities and Inclinations	105
4.5	Conclusions	107
5	On the Tidal Evolution of Kuiper Belt Binaries	116
	Abstract	117
5.1	Introduction	118
5.2	Collisional Formation and Tidal Evolution Outwards	120
5.2.1	Parameters of the Orcus-Vanth System	120
5.2.2	Tidal Evolution Outwards	121
5.3	Tidal Evolution Inwards	123
5.4	Kozai Cycles with Tidal Friction	124
5.5	Orbital Evolution Models	127
5.6	Application of KCTF Model to Orcus-Vanth	129
5.7	Discussion: General effects of KCTF on KBO binaries	133
5.8	Conclusions	136
5.9	Appendix: The Orbital Evolution Model	136
5.9.1	Introduction to EKE Framework	136
5.9.2	Adding Permanent Asymmetries	137
5.9.3	Tidal Q	139
5.9.4	Potential Improvements to the Model	140

List of Figures

2.1	Fraction of apsidal precession due to planetary quadrupole	32
2.2	Photometric difference signal from k_{2p} , $\omega = 0^\circ$	39
2.3	Excerpts of photometric difference signal, $\omega = 0^\circ$	40
2.4	Photometric difference signal from k_{2p} , $\omega = 90^\circ$	41
2.5	Excerpts of photometric difference signal, $\omega = 90^\circ$	42
2.6	Eccentricities needed to detect interior properties from apsidal precession	46
2.7	Effect of impact parameter on precession signal	47
3.1	Proper orbital elements of 2003 EL61 family members and candidates	83
3.2	Illustration of determining Δv for candidate family members	84
3.3	Fraction of particles diffused in eccentricity	85
3.4	Distribution of eccentricities of 12:7 resonants at half-billion year intervals	86
3.5	Correlation of eccentricity distributions at different ages	87
4.1	Haumea's satellites as viewed from Earth	112
4.2	Observed and model positions of Hi'iaka and Namaka	113
4.3	Residuals of the three-point mass model	114
4.4	Relationship between radius, density, and albedo for Hi'iaka and Namaka	115
5.1	Evolution of the Periapse of a KBO Binary undergoing KCTF	132

List of Tables

2.1	Extra-Solar System Parameters and Results	48
3.1	KBOs Near the 2003 EL61 Family	72
3.2	Diffused KBOs Near the 2003 EL61 Family	75
4.1	Observed Astrometric Positions for the Haumea System	92
4.2	Fitted Parameters of the Haumea System	99
4.3	State Vector for the Haumea System	99

Chapter 1

Introduction

The year 1609 saw two landmark discoveries in the field of planetary science. The observational breakthrough was made by Galileo Galilei who that year turned a telescope to the skies for the first time in human history. His new tool led to the first major discoveries of planetary science: the phases of Venus, the moons of Jupiter, mountains on the Moon, and the rings of Saturn. The theoretical breakthrough was made by Johannes Kepler, who published in *Astronomia Nova* his new theory of planetary motion. Included in this theory was the empirical observation that the planets orbit the Sun in fixed elliptical orbits and that their rate of orbital motion swept out equal areas in equal times. These are now known as Kepler's first and second laws of planetary motion (the third law would come in 1619). Four hundred years later, planetary scientists are still making discoveries based on these two breakthroughs. The results presented in this thesis used telescopes about ten thousand times stronger than Galileo's original refractor, along with powerful analytical tools, originally developed by Isaac Newton, that mathematically codify Kepler's empirical laws.

These observational and theoretical tools are applied to various problems in orbital dynamics. The main goal of orbital dynamics or celestial mechanics is to explain the motion of bodies in space due to their mutual (gravitational) interactions. The simplest non-trivial dynamical system is the orbital motion of two point-masses in space. This two-body problem has a straightforward analytical solution: each object orbits the center of mass in a fixed elliptical orbit. In honor of Johannes Kepler's empirical discovery of this elliptical motion, such orbits are called Keplerian.

Anything more complex than the two-body problem will execute non-Keplerian motion. When attempting to solve these complex dynamical problems, the first goal is to identify the most important aspect that has not yet been included in the solution. Each of the four subsequent chapters in my thesis represents a problem that is slightly more complicated than the two-body problem; in each case, my work was to characterize the dominant non-Keplerian aspect of the problem that had not yet been considered.

1.1 Chapter 2: Extra-Solar Planet Interiors

Chapter 2 studies the orbital motion of planets orbiting other stars. Over 300 such extra-solar planets have been discovered in the last fifteen years; Marcy et al. (2005) estimate that $\sim 12\%$ of stars possess gas giant planets within about 20 AU. Originally, most extra-solar planets were discovered through measuring the stellar radial velocities. When the radial velocity motion matched the Keplerian motion of a star around the center-of-mass of a star-planet system, the presence of the planet could be indirectly inferred. The radial velocity technique had its first major successes beginning in 1995, with the discovery by (Mayor and Queloz, 1995) of a planet orbiting the star 51 Pegasi. Planets like 51 Pegasi b were totally unexpected: it is a Jupiter-like planet in a surprisingly un-Jupiter-like orbit with an orbital period of only 4 days. Planets like 51 Pegasi b are called “hot Jupiters” to emphasize that they orbit their parent stars at a radius ~ 100 times closer than Jupiter in our solar system.

Since the orbits of hot Jupiters are so compact, there is a $\sim 10\%$ chance that these planets will pass in front of their parent star as seen from Earth (as compared to a $\sim 0.1\%$ chance for a planet in a Jupiter-like orbit). As a consequence, the star will diminish in brightness as the dark planet occults a portion of the bright star. The depth of the photometrically observed transit is proportional to the ratio of areas of the planet and star. The first observation of such a transiting planet around HD 209458 (Charbonneau et al., 2000) proved that these objects were similar to Jupiter, because the $\sim 1\%$ depth of the transit corresponds to an object the size of Jupiter (since $\left(\frac{R_{\text{Jup}}}{R_{\text{Sun}}}\right)^2 \approx 0.01$). Using the *Hubble Space Telescope* (HST), precise photometry at the 10^{-4} level can be achieved allowing for a detailed description of many properties of the planetary and stellar system (Winn, 2009). Planets transiting bright stars are the most information-rich planetary objects outside our solar system.

Many transiting planets have radii that are much larger than can be explained by interior models (e.g., Guillot et al., 2006; Burrows et al., 2007), resulting in anomalously tiny densities (as low as $\sim 0.3 \text{ g cm}^{-3}$). Other planets have surprisingly high densities, indicative of very large solid cores (Sato et al., 2005). For both kinds of planets, it may be very difficult or even impossible to determine the correct modifications needed to align planetary interior models with the wide range of observed planetary densities.

Our contribution to this problem was to suggest a model-independent measure of interior structure that would be valuable in order to begin disentangling otherwise unconstrained physics. The interior density distribution of a planet affects the size of rotational and tidal bulges caused by the planet’s spin and the nearby star’s gravitational field, respectively. These effects can all be captured with a single number, k_{2p} , the planetary Love number, which ranges from 0 for a perfectly rigid planet to 1.5 for a fluid totally homogeneous planet. The Love numbers of Jupiter ($k_{2J} \simeq 0.49$) and Saturn ($k_{2S} \simeq 0.32$) differ because Saturn has a relatively larger core of solid elements. The value

of k_{2p} reflects the amount of central condensation of a body and thus, a measurement of k_{2p} is a model-independent probe of planetary interiors. (It is equivalent to measuring J_2 of an extra-solar planet.)

It has been known for decades that a non-zero value of k_2 creates a non-Keplerian orbital precession, i.e., a rotation of the normally-fixed orbital ellipse (Russell, 1928; Cowling, 1938; Sterne, 1939a,b). This subtle non-Keplerian effect can be measured with precise light curve measurements over a long time baseline. In fact, measuring orbital precession in eclipsing binary systems gave the first model-independent indication that stars were highly centrally condensed ($k_{2*} \approx 0.03$). However, until our work in Chapter 2, no one had applied this method to extra-solar planets with the goal of measuring planetary interiors.

One of the surprising conclusions about orbital precession in extra-solar planetary systems is that the planet is actually the dominant source of precession, with the much more massive star contributing a factor of ~ 10 less. The huge tidal bulge raised on the planet by the star, sometimes reaching over 2000 km in size, creates a significant modification to Keplerian motion. The rate of orbital precession is strongly dependent on the star-planet distance, so we focused on planets that were extremely close to their parent stars, known as very hot Jupiters, which have semi-major axes of only ~ 0.02 AU and orbital periods of 1-2 days. For such planets, the orbital precession due to the planetary interior is nearly 100 times more powerful than precession caused by the star or general relativity.

This prominent effect and its usefulness for obtaining model-independent measurements of planetary interiors had not been recognized in the extra-solar planet community. Therefore, we chose to extend our study beyond the theoretical orbital dynamics and to demonstrate that actual measurements of orbital precession of transiting planets were possible. The most powerful photometric tool for measuring k_{2p} in the short-term is NASA's *Kepler* mission, which successfully launched on March 6, 2009 and started taking high quality science data on May 13, 2009. To achieve its main goal of detecting transiting Earth-radius planets in Earth-like orbits, *Kepler* will also obtain exquisite photometry of over 100000 stars, about 30 of which are expected to host hot Jupiters with periods less than 3 days (Beatty & Gaudi, 2008). Chapter 2 contains a full model of *Kepler* photometry on transiting planets in order to demonstrate the ability to detect orbital precession of very hot Jupiters.

By investigating the full photometric signal of orbital precession, Chapter 2 demonstrates that *Kepler* can realistically detect apsidal precession with the accuracy necessary to infer the presence or absence of a massive core in very hot Jupiters with orbital eccentricities as low as $e \simeq 0.003$. Furthermore, the signal due to k_{2p} creates unique transit light curve variations that are generally not degenerate with other parameters or phenomena. In this chapter, we discuss the plausibility of measuring k_{2p} in an effort to directly constrain the interior properties of extra-solar planets. This

chapter is about to be published in the *Astrophysical Journal* under the title, “Probing the Interiors of Very Hot Jupiters Using Transit Light Curves.”

1.2 Chapter 3: The Haumea Family

The remainder of my doctorate research focused on the orbital dynamics of minor planets within our own solar system orbiting beyond Neptune. These icy bodies are called Kuiper belt objects (KBOs) in honor of Gerard Kuiper’s prediction of a distant population of small bodies similar to the asteroid belt (Edgeworth, 1949; Kuiper, 1951). Throughout this thesis, the term KBOs is synonymous with transneptunian objects and refers to the entire population of solar system small bodies with semi-major axes greater than Neptune’s ($a \gtrsim 30$ AU).

The properties of the ~ 1000 known KBOs orbiting beyond Neptune have already changed our understanding of the formation of the outer solar system. For example, the orbital distribution of these bodies point to a past dynamical excitation event during a chaotic episode in solar system history (e.g., Malhotra, 1995; Gomes et al., 2005; Chiang et al., 2007; Levison et al., 2008a) as well as significant orbital migration of the outer planets (e.g., Fernandez and Ip, 1984; Malhotra, 1993; Gomes et al., 2005b). Studying the orbital dynamics of KBOs improves our understanding of the early formation and evolution of the solar system.

For several years, Prof. Michael Brown has led a major observational effort to discover and characterize new KBOs. One of the major aspects of this research was the spectroscopic survey of near-infrared spectra of bright KBOs, summarized by Barkume et al. (2008). These authors found that KBOs fell into three major spectroscopic categories: methane-rich dwarf planets (Eris, Pluto, and Makemake), KBOs with strong water ice spectra (Haumea and others), and KBOs with featureless near-IR spectra (the majority of KBOs). The difference between the methane-rich and featureless categories can be explained by the model of Schaller and Brown (2007), who show that only the largest KBOs are massive enough to prevent a methane atmosphere from escaping.

An explanation of the objects with strong water ice spectra was not as clear. These objects spanned a wide range of sizes and had atypical optical colors (blue or gray gradients, instead of the strong red gradient observed for most KBOs). The key to understanding these objects was in their orbital parameters: they were all clustered within a small region of semi-major axis, eccentricity, and inclination. The only viable hypothesis that can explain a clustering in both surface and orbital properties is that these objects were all once part of the same parent body. In other words, these icy bodies are a collisional family.

A sufficiently energetic collision can impart enough velocity to gravitationally eject many of the impact fragments. These fragments go into nearby orbits and together form a collisional family. Dozens of these families have been identified in the asteroid belt since Hirayama’s original identi-

cations of groups of asteroids nearly a century ago (Hirayama, 1918). Recent modeling has shown that these groups of asteroids with similar orbits and spectra are very well explained by collisional formation (e.g., Durda et al., 2007).

Families in the Kuiper belt are unique, even compared to asteroid families, because they are direct fingerprints of ancient collisions. In the asteroid belt, the Yarkovsky effect and other perturbations degrade the coherence of asteroid families after hundreds of millions of years (Farinella & Vokrouhlicky, 1999; Milani & Farinella, 1994). Kuiper belt families stay mostly coherent over the age of the solar system and can provide a direct view of processes present at the beginning of the solar system.

In Brown et al. (2007), we showed that the dynamical clustering of objects with strong water ice spectra was well explained by a collisional family. The largest remnant of this family is the dwarf planet Haumea, the largest object with a strong water ice spectrum. Our discovery of the first known Kuiper belt family around the dwarf planet Haumea (formerly known as 2003 EL61) has already been called a “milestone” in the study of the Kuiper belt (Morbidelli, 2007), because families are a unique testbed for theories of the dynamical, collisional, and surface properties of KBOs.

The dwarf planet Haumea is, perhaps, the most interesting object in the Kuiper Belt. Early in solar system history (Levison et al., 2008), Haumea experienced a massive collision that imparted its ultra-fast rotation (Rabinowitz et al., 2006), created two moons (Brown et al., 2006; Chapter 4), and shattered its icy mantle, sending fragments into nearby heliocentric orbits (Brown et al., 2007). As discussed above, these fragments were discovered after the largest spectroscopic survey of Kuiper belt objects (Barkume et al., 2008) revealed that six KBOs had remarkably deep water ice absorptions, including Haumea and its brightest satellite (Barkume et al., 2006) and four other KBOs in nearby heliocentric orbits.

The spectroscopic survey that identified the original Haumea family members was limited to the ~ 40 brightest KBOs. The vast majority of KBOs cannot be studied spectroscopically which significantly limits the ability to find new family members observationally. We therefore turned to a dynamical analysis of the Haumea family in an attempt to identify new candidate family members and to characterize the Haumea family in more detail. The results of this work are presented in Chapter 3.

The ejection of orbits from a collision can be simulated dynamically by giving objects an isotropic non-Keplerian velocity “kick” of magnitude Δv from a single collision location in space. This instantly changes the orbital elements of the ejected bodies and creates a unique pattern of semi-major axes, eccentricities, and inclinations. In Chapter 3, we model the orbital element spread of the original Haumea family members to estimate the original collision location. We then take all known KBOs and calculate their proximity to the collision through the estimated value of Δv needed to reach their current orbits. The objects with the lowest value of Δv are good candidates

for membership in the Haumea family. This and other techniques used in Chapter 3 were based on similar techniques used for asteroid families, adapted for application in the Kuiper belt.

Two KBOs, predicted to be family members by the dynamical analysis of Chapter 3, have recently been observed spectroscopically by Schaller & Brown (2008). These authors find that the predicted family members indeed share the same deep water ice spectra characteristic of Haumea family members. Additional Haumea family members will be identified in the future by observing more of the candidates identified in Chapter 3 as well as the discovery of additional KBOs near the center of the family.

Performing this Δv analysis yielded one very unusual result: Haumea is not at the center of the collision. This is surprising, since it is by far the largest family member and also has clearly experienced a giant collision in the past as inferred from its high density, ultra-fast rotation, and two small moons. As discussed in Brown et al. (2007) and modeled in Chapter 3, the reason Haumea is not at the center of the collisional family is that it has diffused from its original orbital location as the result of a weak mean-motion resonance with Neptune. Haumea’s heliocentric orbital period is exactly 12/7 times larger than Neptune’s orbital period. Orbital diffusion within mean-motion resonances had been demonstrated before (it is the origin of the Kirkwood gaps in the asteroid belt, for example). We found empirically that such diffusion nearly conserves the Tisserand parameter $T \approx \cos i \sqrt{1 - e^2}$. The current eccentricity (inclination) of Haumea is higher (lower) than the expected collision center in a way that is consistent with conservation of the Tisserand parameter. Hence, allowing for the non-Keplerian effect of resonance diffusion, the current location of all the known family members are consistent with a tight dynamical cluster ($\Delta v \lesssim 150 \text{ m s}^{-1}$).

Though chaotic in nature, resonance diffusion has an associated timescale. Using the estimated initial location of the center of the Haumea family, Chapter 3 also describes how the age of the Haumea family can be estimated by calculating the time Haumea needs to diffuse to its current location. Through n -body dynamical simulations of the giant planets and objects in the 12:7 resonance, we showed that the Haumea family must be at least 1 Gyr old, with 90% confidence. That is, only 10% of simulated particles moved from the center of the collision to the current location of Haumea within 1 Gyr. Our estimate for the age of the Haumea family is 3.5 ± 2 Gyr. The lack of precision is due to the chaotic nature of resonance diffusion. In Chapter 3, we show that the precision can be increased with the discovery of more resonant Haumea family members. I estimate that future surveys of the Kuiper belt, such as Pan-STARRS and LSST (Trujillo, 2008), will provide enough family members to date the age of the Haumea collision with a precision of 0.5 Gyr by the year 2020. An absolute age determination of the Haumea family will be extremely valuable for constraining models of outer solar system formation.

The ancient nature of the Haumea family fits in well with the general understanding of the formation of the Kuiper belt. Most successful models of outer solar system formation predict that

the primordial Kuiper belt was about 100 times more massive than the Kuiper belt seen today. In the current Kuiper belt, the probability of the collision needed to form the Haumea family is very low, less than 1%. There is a significant increase in collision probability obtained by forming the Haumea family early in the history of the Kuiper belt when the number densities were much higher. The formation of the Haumea family was studied in detail by Levison et al. (2008), who conclude that the most probable origin of the Haumea family is an ancient collision between two scattered-disk objects.

Chapter 3 was published as Ragozzine & Brown (2007) in the *Astronomical Journal* under the title, “Candidate Members and an Age Estimate of the Family of Kuiper Belt Object 2003 *EL*₆₁.”

1.3 Chapter 4: The Satellites of Haumea

The giant impact that formed the collisional family of Haumea (Chapter 3) also presumably formed the two small satellites discovered by Brown et al. (2005) and Brown et al. (2006). These two satellites share the spectral features of Haumea and the other Haumea family members (Barkume et al., 2006; Fraser and Brown, 2009) and it is certainly possible for a single giant impact to produce both satellites and a collisional family, though the Haumea collision has not yet been modeled in detail. Hence, it is likely that the two satellites, named Hi'iaka and Namaka, were formed in a giant collision billions of years ago.

As a result of Kepler's third law (published in 1619), measurements of the orbital period and semi-major axis of a binary system can be combined to yield the total mass. By determining the orbit of the outer brighter satellite Hi'iaka, Brown et al. (2005) found the mass of Haumea to be about 4.2×10^{20} kg or 1/3 the mass of Pluto. These authors also found that the orbit of Hi'iaka had a relatively large semi-major axis ($a \simeq 49000$ km) and a non-zero eccentricity ($e \simeq 0.05$). This orbit is moderately inconsistent with simple tidal models that would predict a smaller separation and a nearly circular orbit for a satellite that tidally evolved outwards after its initial formation near the Roche lobe of Haumea (Brown et al., 2005).

Determining the orbit of the inner fainter satellite, Namaka, was much more difficult. Non-Keplerian perturbations from Hi'iaka and the J_2 of the elongated Haumea (Rabinowitz et al., 2006) are so strong, that it is impossible to fit a reasonable Keplerian model to the observations spanning more than about a month. Over the course of three years and several nights of observation, we eventually asked for and received time on HST to observe the triple system 5 times over the course of 8 days. This was enough to determine a preliminary Keplerian orbit whose parameters could then be used in a fully interacting three-point mass model to determine the orbits of both satellites and the masses of all three bodies. The astrometric data was sufficient to fully characterize the orbits of Hi'iaka and Namaka as well as the masses of Haumea and Hi'iaka, with values given in Chapter 4.

However, the mass of Namaka was only marginally detected and Haumea's J_2 was too degenerate with the mass of Hi'iaka to measure separately.

Even before the full solution was determined, we realized that Namaka's orbit was nearly edge-on, which was confirmed by our solution of the orbital motion. In an analogy to transiting extra-solar planets (Chapter 2), Namaka's orbit currently takes it in front of and behind Haumea as seen from Earth. That is, according to the orbit solution, the Haumea system is currently undergoing mutual events (Fabrycky et al., 2008).

Using the known orbit, the angle between Namaka, Haumea, and the Earth (in the case of occultations) or the Sun (in the case of shadowing) falls well below the ~ 13 milliarcseconds (~ 500 km) of the projected shortest axis of Haumea. Observing multiple mutual events can yield accurate and useful measurements of several system properties as shown by the results of the Pluto-Charon mutual event season (e.g. Binzel & Hubbard, 1997). The depth of an event where Namaka occults Haumea leads to the ratio of albedos and, potentially, a surface albedo map of Haumea, which is known to exhibit color variations as a function of rotational phase, indicative of a variegated surface (Lacerda et al., 2008; Lacerda, 2008). Over the course of a single season, Namaka will traverse several chords across Haumea allowing for a highly accurate measurement of Haumea's size, shape, and spin pole direction (e.g., Descamps et al., 2008). The precise timing of mutual events will also serve as extremely accurate astrometry, allowing for an orbital solution much more precise than reported in Chapter 4. Our solution also predicts two satellite-satellite events, one in February 2009 and one in July 2009 — the last such event until the next mutual event season begins around the year 2100.

Our knowledge of the state of the Haumea system will improve significantly with the observation and analysis of these events. See <http://web.gps.caltech.edu/~mbrown/2003EL61/mutual> for up-to-date information on the Haumea mutual events. To date (May 29, 2009), there are no secure detections of any of the Haumea-Namaka mutual events, though some of our observations are highly suggestive. We also applied for and received HST observations of the February 2009 satellite-satellite event. The accurate resolved photometry show significant variability that it still being interpreted.

Although the mutual events are very interesting for the future, the actual orbits themselves show unexpected implications for Haumea's past. Throughout the solar system, all multiple satellite systems with well-known tidally-evolved orbits have very low eccentricities and inclinations. With an eccentricity of 0.25 ± 0.02 and mutual inclination of $13^\circ \pm 1^\circ$, Namaka's orbit is most unusual. The excitation of Namaka's orbit is almost certainly due to the also unique combination of massive interacting satellites and extensive tidal evolution (e.g., Canup et al., 1999). As the satellites tidally evolved outwards, they passed through mean-motion resonances that excited their eccentricity and inclination. For a detailed qualitative description of this model, see Chapter 4. It is interesting to note that the satellites are highly tidally-evolved, implying that they, like the Haumea family, were not formed in recent geologic history.

Chapter 4 was published as Ragozzine & Brown (2009) in the *Astronomical Journal* under the title, “Orbits and Masses of the Satellites of the Dwarf Planet Haumea (2003 EL₆₁)”.

1.4 Chapter 5: The Changing Orbits of Kuiper Belt Binaries

Haumea is not the only Kuiper belt object with satellites. Dozens of KBOs are known to be binary (Noll et al., 2008b) and it is already clear that these binaries are giving us unique clues into the evolution of the outer solar system (Noll et al., 2008a). For example, Brown et al. (2006) found that the binary fraction of large KBOs is significantly higher than the binary fraction of smaller KBOs and Noll et al. (2008b) recently reported that the binary fraction of non-resonant KBOs with low heliocentric inclinations ($29.3 \pm_{6.3}^{7.2}\%$) is strikingly different from the binary fraction of high inclination KBOs of similar sizes ($2.9 \pm_{2.4}^{6.5}\%$).

In light of these recent results, it seems clear that a major goal of the KBO community will be to use the orbital distributions of KBO binaries to constrain theories on the formation of the Kuiper belt. Achieving this goal will require many observational and theoretical studies of KBO binaries.

One major difficulty in connecting the observations to formation theories is that the current orbital properties of KBOs may not represent the initial orbital distribution. Without a clear understanding of the processes that can modify KBO binary orbits, there is no sure way to extrapolate the present-day observational trends backwards in time in order to gain insights into binary formation mechanisms. As a result, we must begin addressing mechanisms that can modify KBO binary orbits since their initial epoch of formation.

Two mechanisms that may modify the orbits of KBO binaries on geologic timescales are perturbations from the Sun and tidal evolution (Greenberg & Barnes, 2008; Perets & Naoz, 2008). In Chapter 5, we study these non-Keplerian effects using a model developed specifically for KBO binaries. Since this is one of the first major attempts to calculate the orbital and tidal evolution of KBO binaries, the techniques of Chapter 5 are not applied to specific binary systems; instead, general results are sought.

We find that perturbations from the Sun (in the form of Kozai oscillations and Cassini states) combined with tidal evolution at high eccentricities can significantly modify the semi-major axes, eccentricities, inclinations, spin rates, and obliquities of KBO binaries. In particular, orbital and tidal evolution can change binary properties from those indicative of formation by gravitational capture (Goldreich et al., 2002) to those indicative of formation by giant impact (Canup, 2005). The Orcus-Vanth binary is used as a test case to show that solar perturbations and tidal evolution complicate the interpretation of binary orbital properties.

Though potentially adverse to the goal of inferring the original orbital distribution of KBO binaries, these effects do leave unique observational signatures, which are also discussed in Chapter

5. Future theoretical and observational studies will clarify the importance of these effects.

Though dynamics is arguably the oldest branch of planetary physics, there is still theoretical and observational progress being made over 400 years after its birth. This thesis represents my minor contribution to planetary science in a study of the orbital dynamics of Kuiper belt object satellites, a Kuiper belt family, and extra-solar planet interiors.

Bibliography

- K. M. Barkume, M. E. Brown, and E. L. Schaller. Water Ice on the Satellite of Kuiper Belt Object 2003 EL₆₁. *Astrophysical Journal, Letters*, 640, L87-L89, March 2006.
- K. M. Barkume, M. E. Brown, and E. L. Schaller. Near-Infrared Spectra of Centaurs and Kuiper Belt Objects. *Astronomical Journal*, 135:55–67, January 2008.
- T. G. Beatty and B. S. Gaudi. Predicting the Yields of Photometric Surveys for Transiting Extrasolar Planets. *ArXiv e-prints*, 804, April 2008.
- R. P. Binzel and W. B. Hubbard. *Pluto and Charon, ed. S.A. Stern, D.J Tholen (U. Arizona Press:1997)*. 1997.
- M. E. Brown, A. H. Bouchez, D. Rabinowitz, R. Sari, C. A. Trujillo, M. van Dam, R. Campbell, J. Chin, S. Hartman, E. Johansson, R. Lafon, D. Le Mignant, P. Stomski, D. Summers, and P. Wizinowich. Keck Observatory Laser Guide Star Adaptive Optics Discovery and Characterization of a Satellite to the Large Kuiper Belt Object 2003 EL₆₁. *Astrophysical Journal, Letters*, 632:L45–L48, October 2005.
- M. E. Brown, M. A. van Dam, A. H. Bouchez, D. Le Mignant, R. D. Campbell, J. C. Y. Chin, A. Conrad, S. K. Hartman, E. M. Johansson, R. E. Lafon, D. L. Rabinowitz, P. J. Stomski, Jr., D. M. Summers, C. A. Trujillo, and P. L. Wizinowich. Satellites of the Largest Kuiper Belt Objects. *Astrophysical Journal, Letters*, 639:L43–L46, March 2006.
- M. E. Brown, K. M. Barkume, D. Ragozzine, and E. L. Schaller. A Collisional Family of Icy Objects in the Kuiper Belt. *Nature*, 446:294–296, March 2007.
- A. Burrows, I. Hubeny, J. Budaj, and W. B. Hubbard. Possible Solutions to the Radius Anomalies of Transiting Giant Planets. *Astrophysical Journal*, 661:502–514, May 2007. doi: 10.1086/514326.
- R. M. Canup. A Giant Impact Origin of Pluto-Charon. *Science*, 307:546–550, January 2005.
- R. M. Canup, H. F. Levison, and G. R. Stewart. Evolution of a Terrestrial Multiple-Moon System. *Astronomical Journal*, 117:603–620, January 1999.
- D. Charbonneau, T. M. Brown, D. W. Latham, and M. Mayor. Detection of Planetary Transits Across a Sun-like Star. *Astrophysical Journal, Letters*, 529:L45–L48, January 2000. doi: 10.1086/312457.
- E. Chiang, Y. Lithwick, R. Murray-Clay, M. Buie, W. Grundy, and M. Holman. A Brief History of

- Transneptunian Space. In B. Reipurth, D. Jewitt, and K. Keil, editors, *Protostars and Planets V*, pages 895–911, 2007.
- T. G. Cowling. On the Motion of the Apsidal Line in Close Binary Systems. *Monthly Notices of the RAS*, 98, 734, June 1938.
- P. Descamps, F. Marchis, J. Pollock, J. Berthier, F. Vachier, M. Birlan, M. Kaasalainen, A. W. Harris, M. H. Wong, W. J. Romanishin, E. M. Cooper, K. A. Kettner, P. Wiggins, A. Kryszczyńska, M. Polinska, J.-F. Coliac, A. Devyatkin, I. Verestchagina, and D. Gorshanov. New determination of the size and bulk density of the binary Asteroid 22 Kalliope from observations of mutual eclipses. *Icarus*, 196:578–600, August 2008. doi: 10.1016/j.icarus.2008.03.014.
- D. D. Durda, W. F. Bottke, D. Nesvorný, B. L. Enke, W. J. Merline, E. Asphaug, and D. C. Richardson. Size Frequency Distributions of Fragments from SPH/N-body Simulations of Asteroid Impacts: Comparison with Observed Asteroid Families. *Icarus*, 186:498–516, February 2007.
- K. E. Edgeworth. The origin and evolution of the Solar System. *Monthly Notices of the RAS*, 109: 600–609, 1949.
- D. C. Fabrycky, D. Ragozzine, M. E. Brown, and M. J. Holman. Mutual Events of (136108) 2003 EL₆₁ and S/2005 (136108) 2. *IAU Circular*, 8949, May 2008.
- P. Farinella and D. Vokrouhlicky. Semimajor Axis Mobility of Asteroidal Fragments. *Science*, 283: 1507–1510, March 1999.
- J. A. Fernandez and W.-H. Ip. Some Dynamical Aspects of the Accretion of Uranus and Neptune - The Exchange of Orbital Angular Momentum with Planetesimals. *Icarus*, 58:109–120, April 1984.
- W. C. Fraser and M. E. Brown. NICMOS Photometry of the Unusual Dwarf Planet Haumea and its Satellites. *Astrophysical Journal, Letters*, 695:L1–L3, April 2009. doi: 10.1088/0004-637X/695/1/L1.
- P. Goldreich, Y. Lithwick, and R. Sari. Formation of Kuiper-belt Binaries by Dynamical Friction and Three-body Encounters. *Nature*, 420:643–646, December 2002.
- R. Gomes, H. F. Levison, K. Tsiganis, and A. Morbidelli. Origin of the Cataclysmic Late Heavy Bombardment Period of the Terrestrial Planets. *Nature*, 435:466–469, May 2005a. doi: 10.1038/nature03676.
- R. S. Gomes, T. Gallardo, J. A. Fernández, and A. Brunini. On The Origin of The High-Perihelion Scattered Disk: The Role of The Kozai Mechanism And Mean Motion Resonances. *Celestial Mechanics and Dynamical Astronomy*, 91:109–129, March 2005b.
- R. Greenberg and R. Barnes. Tidal Evolution of Dysnomia, Satellite of the Dwarf Planet Eris. *Icarus*, 194:847–849, April 2008.
- T. Guillot, N. C. Santos, F. Pont, N. Iro, C. Melo, and I. Ribas. A Correlation Between the Heavy Element Content of Transiting Extrasolar Planets and the Metallicity of their Parent Stars. *Astronomy and Astrophysics*, 453:L21–L24, July 2006. doi: 10.1051/0004-6361:20065476.

- K. Hirayama. Groups of Asteroids probably of Common Origin. *Astronomical Journal*, 31:185–188, October 1918.
- G. P. Kuiper. On the Origin of the Solar System. 357, 1951.
- P. Lacerda. Time-Resolved Near-Infrared Photometry of Extreme Kuiper Belt Object Haumea. *ArXiv e-prints*, November 2008.
- P. Lacerda, D. Jewitt, and N. Peixinho. High-Precision Photometry of Extreme Kbo 2003 EL₆₁. *Astronomical Journal*, 135, 1749–1756, May 2008.
- H. F. Levison, A. Morbidelli, C. Vanlaerhoven, R. Gomes, and K. Tsiganis. Origin of the structure of the Kuiper belt during a dynamical instability in the orbits of Uranus and Neptune. *Icarus*, 196:258–273, July 2008a.
- H. F. Levison, A. Morbidelli, D. Vokrouhlický, and W. F. Bottke. On a Scattered-Disk Origin for the 2003 EL₆₁ Collisional Family — An Example of the Importance of Collisions on the Dynamics of Small Bodies. *Astronomical Journal*, 136:1079–1088, September 2008b.
- R. Malhotra. The Origin of Pluto’s Peculiar Orbit. *Nature*, 365:819, October 1993.
- R. Malhotra. The Origin of Pluto’s Orbit: Implications for the Solar System Beyond Neptune. *Astronomical Journal*, 110:420, July 1995.
- G. Marcy, R. P. Butler, D. Fischer, S. Vogt, J. T. Wright, C. G. Tinney, and H. R. A. Jones. Observed Properties of Exoplanets: Masses, Orbits, and Metallicities. *Progress of Theoretical Physics Supplement*, 158:24–42, 2005. doi: 10.1143/PTPS.158.24.
- M. Mayor and D. Queloz. A Jupiter-Mass Companion to a Solar-Type Star. *Nature*, 378:355, November 1995. doi: 10.1038/378355a0.
- A. Milani and P. Farinella. The age of the Veritas asteroid family deduced by chaotic chronology. *Nature*, 370:40, July 1994.
- A. Morbidelli. Solar system: Portrait of a suburban family. *Nature*, 446:273–274, March 2007.
- K. S. Noll, W. M. Grundy, E. I. Chiang, J.-L. Margot, and S. D. Kern. *Binaries in the Kuiper Belt*, pages 345–363. The Solar System Beyond Neptune, 2008a.
- K. S. Noll, W. M. Grundy, D. C. Stephens, H. F. Levison, and S. D. Kern. Evidence for two populations of classical transneptunian objects: The strong inclination dependence of classical binaries. *Icarus*, 194:758–768, April 2008b.
- H. B. Perets and S. Naoz. The eccentric behavior of inclined binary minor planets. *ArXiv e-prints*, September 2008.
- D. L. Rabinowitz, K. Barkume, M. E. Brown, H. Roe, M. Schwartz, S. Tourtellotte, and C. Trujillo. Photometric Observations Constraining the Size, Shape, and Albedo of 2003 EL₆₁, a Rapidly Rotating, Pluto-sized Object in the Kuiper Belt. *Astrophysical Journal*, 639:1238–1251, March 2006.
- D. Ragozzine and M. E. Brown. Candidate Members and Age Estimate of the Family of Kuiper

- Belt Object 2003 EL61. *Astronomical Journal*, 134:2160–2167, December 2007.
- D. Ragozzine and M. E. Brown. Orbits and Masses of the Satellites of the Dwarf Planet Haumea (2003 EL61). *Astronomical Journal*, 137:4766–4776, June 2009.
- H. N. Russell. On the advance of periastron in eclipsing binaries. *Monthly Notices of the RAS*, 88: 641–643, June 1928.
- B. Sato, D. A. Fischer, G. W. Henry, G. Laughlin, R. P. Butler, G. W. Marcy, S. S. Vogt, P. Bodenheimer, S. Ida, E. Toyota, A. Wolf, J. A. Valenti, L. J. Boyd, J. A. Johnson, J. T. Wright, M. Ammons, S. Robinson, J. Strader, C. McCarthy, K. L. Tah, and D. Minniti. The N2K Consortium. II. A Transiting Hot Saturn around HD 149026 with a Large Dense Core. *Astrophysical Journal*, 633:465–473, November 2005. doi: 10.1086/449306.
- E. L. Schaller and M. E. Brown. Volatile Loss and Retention on Kuiper Belt Objects. *Astrophysical Journal, Letters*, 659:L61–L64, April 2007. doi: 10.1086/516709.
- E. L. Schaller and M. E. Brown. Detection of Additional Members of the 2003 EL61 Collisional Family via Near-Infrared Spectroscopy. *Astrophysical Journal, Letters*, 684:L107–L109, September 2008.
- T. E. Sterne. Apsidal motion in binary stars. *Monthly Notices of the RAS*, 99:451–462, March 1939a.
- T. E. Sterne. Apsidal motion in binary stars. II. Distributions of density. *Monthly Notices of the RAS*, 99:662, June 1939b.
- C. A. Trujillo. *Future Surveys of the Kuiper Belt*, pages 573–585. The Solar System Beyond Neptune, 2008.
- J. N. Winn. Measuring accurate transit parameters. In *IAU Symposium*, volume 253 of *IAU Symposium*, pages 99–109, February 2009. doi: 10.1017/S174392130802629X.

Chapter 2

Probing the Interiors of Very Hot Jupiters Using Transit Light Curves

This chapter will be published in its entirety under the same title by authors D. Ragozzine and A. S. Wolf in the *Astrophysical Journal*, 2009. Reproduced by permission of the American Astronomical Society.

Abstract

Accurately understanding the interior structure of extra-solar planets is critical for inferring their formation and evolution. The internal density distribution of a planet has a direct effect on the star-planet orbit through the gravitational quadrupole field created by the rotational and tidal bulges. These quadrupoles induce apsidal precession that is proportional to the planetary Love number (k_{2p} , twice the apsidal motion constant), a bulk physical characteristic of the planet that depends on the internal density distribution, including the presence or absence of a massive solid core. We find that the quadrupole of the planetary tidal bulge is the dominant source of apsidal precession for very hot Jupiters ($a \lesssim 0.025$ AU), exceeding the effects of general relativity and the stellar quadrupole by more than an order of magnitude. For the shortest-period planets, the planetary interior induces precession of a few degrees per year. By investigating the full photometric signal of apsidal precession, we find that changes in transit shapes are much more important than transit timing variations. With its long baseline of ultra-precise photometry, the space-based *Kepler* mission can realistically detect apsidal precession with the accuracy necessary to infer the presence or absence of a massive core in very hot Jupiters with orbital eccentricities as low as $e \simeq 0.003$. The signal due to k_{2p} creates unique transit light curve variations that are generally not degenerate with other parameters or phenomena. We discuss the plausibility of measuring k_{2p} in an effort to directly constrain the interior properties of extra-solar planets.

2.1 Introduction

Whether studying planets within our solar system or planets orbiting other stars, understanding planetary interiors represents our best strategy for determining their bulk composition, internal dynamics, and formation histories. For our closest neighbors, we have had the luxury of sending spacecraft to accurately measure the higher-order gravity fields of these objects, yielding invaluable constraints on their interior density distributions. Using these observations, we have been able, for instance, to infer the presence of large cores, providing support for the core-accretion theory of planet formation (Guillot, 2005). Study of planets outside our solar system, however, has necessitated the development and usage of more indirect techniques. Nevertheless, as the number of well-characterized extra-solar planets grows, we gain more clues that help us answer the most fundamental questions about how planets form and evolve.

Guided by our current understanding of planetary physics, we have begun to study the interiors of extra-solar planets. This endeavor has been dominated by a model-based approach, in which the mass and radius of a planet are measured using radial velocity and transit photometry observations, and the interior properties are inferred by finding the model most consistent with those two observations. This strategy clearly requires a set of assumptions, not the least of which is that the physical processes at work in extra-solar planets are just like those that we understand for our own giant planets. While it does seem that this approach is adequate for explaining most of the known transiting planets, there does exist a group of planets for which the usual set of assumptions are not capable of reproducing the observations (e.g., Guillot et al., 2006; Burrows et al., 2007). These are the planets with so-called positive “radius anomalies”, including the first-discovered transiting planet HD 209458b (Charbonneau et al., 2000). Though most of these planets can be explained by adjusting different pieces of the interior physics in the models (including opacities, equations of state, and heat deposition), it is currently impossible to discern which combination of these possible explanations is actually responsible for their observed sizes (Guillot et al., 2006).

Additional uncertainties also exist for planets at the other end of the size spectrum. For the group of under-sized extra-solar planets, such as HD 149026b, the canonical approach is to give the planet a massive highly condensed core of heavy elements in order to match the observed radius. This approach also provides a first order estimate of the planet’s bulk composition, in terms of its fraction of heavy elements. There is also the added complication of how the assumed state of differentiation affects the inferred composition and predicted structure (Baraffe et al., 2008).

Currently, the most promising approach to modeling the distinctive features of extra-solar planet interiors is to study the known transiting planets as an ensemble. The group can be used to develop either a single consistent model that reproduces all the observations (e.g., Guillot et al., 2006) or to showcase the possible diversity in model parameters (e.g., opacities, as in Burrows et al., 2007).

Surely, a model-independent measure of interior structure would be valuable in order to begin disentangling otherwise unconstrained physics.

The idea of obtaining direct structural measurements for distant objects is by no means a new one. For decades, the interiors of eclipsing binary stars have been measured by observing “apsidal motion,” i.e., precession of the orbit due to the non-point-mass component of the gravitational field (Russell, 1928; Cowling, 1938; Sterne, 1939a,b). The signal of the changing orbit is encoded in the light curves of these systems by altering the timing of the primary and secondary eclipses. From these eclipse times, it is straightforward to determine the so-called apsidal motion constant which then constrains the allowed interior density distributions. Interior measurements inferred from apsidal precession were among the first indications that stars were highly centrally condensed. While it seems non-intuitive, we show in this paper that we can use a similar technique to measure the interior properties of very hot Jupiters. Most surprisingly, the interior structure signal for very hot Jupiters actually dominates over the signal from the star, yielding an unambiguous determination of planetary interior properties.

Our theoretical analysis is also extended to full simulated photometry in order to explore the observability of apsidal precession. We show that this precession is observable by measuring the subtle variations in transit light curves. The photometric analysis is focused on the data expected from NASA’s *Kepler* mission, which successfully launched on March 6, 2009 (Borucki et al., 2003; Koch et al., 2006). *Kepler* will obtain exquisite photometry on $\sim 100,000$ stars, of which about 30 are expected to host hot Jupiters with periods less than 3 days (Beatty & Gaudi, 2008). *Kepler* has the potential to measure the gravitational quadrupoles of very hot Jupiters though the technique described below. If successful, this will constitute a major step towards an understanding of the diversity of planetary interiors.

In Section 2, we describe the background theory that connects interior structure and orbital dynamics and explore which effects are most important. Section 3 applies this theory to the observable changes in the transit photometry, including full *Kepler* simulated light curves. We show in Section 4 that the signal due to the planetary interior has a unique signature. Other methods for inferring planetary interior properties are discussed in Section 5. The final section discusses the important conclusions of our work.

2.2 Background Theory

2.2.1 Coordinate System and Notation

The internal structure of very hot Jupiters can be determined by observing changes in the planet’s orbit. These changes can be described in terms of two general types of precession. Apsidal precession refers to rotation of the orbital ellipse within the plane of the orbit. It is characterized by circulation

of the line of apsides, which lies along the major axis of the orbit. Nodal precession, on the other hand, occurs out of the plane of the orbit and refers to the orbit normal precessing about the total angular momentum vector of the system. For typical very hot Jupiter systems with no other planets, apsidal precession has a much stronger observable signal than nodal precession (see Section 2.4.1), so we focus our discussion on the simpler case of a fixed orbital plane.

As is typical for non-Keplerian orbits, the star-planet orbit is described using osculating orbital elements that change in time. We identify the plane of the sky as the reference plane and orient the coordinate axes in the usual way such that the sky lies in the x-z plane with the y-axis pointing at Earth. The intersection of the orbital plane and the reference plane is called the line of nodes, but without directly resolving the system, there is no way to determine the orientation of the line of nodes with respect to astronomical North; thus, the longitude of the ascending node, Ω , cannot be determined. Given this degeneracy, we simplify the description by orienting the z-axis to lie within the plane spanned by the orbit normal and the line-of-sight. The angle between the line of sight and the orbit normal is i , the inclination. The x-axis is in the plane of the sky and is the reference line from which the argument of periape (ω) is measured (in the standard counter-clockwise sense). For this choice of coordinates, the argument of periape and longitude of periape (ϖ) are equivalent. Given this coordinate system, transit centers occur when the planet crosses the y-z plane; this point lies 90° past the reference x-axis, and thus primary transits occur when the true anomaly, f , satisfies $f_{tr} + \omega_{tr} \equiv 90^\circ$, where the subscript tr indicates the value at transit center.¹

Throughout this paper, we refer to parameters of the star (mass, radius, etc.) with subscripts of “*” and parameters of the planet with subscripts of “ p ”. For evaluation of various equations, we will take as fiducial values the mass ratio $M_p/M_* = 10^{-3}$, the radius ratio $R_p/R_* = 0.1$ (though some low density planets have radius ratios greater than $1/6$), and the semi-major axis in stellar radii $a/R_* = 6$, typical for very hot Jupiters, which we define as planets with semi-major axes $a \lesssim 0.025$ AU (see Table 1).² In this definition, we deviate from Beatty & Gaudi (2008), who define very hot Jupiters as planets with periods less than 3 days. These authors estimate that *Kepler* will find ~ 30 such planets, of which ~ 16 will be brighter than V=14 (T. Beatty, pers. comm.). Since our definition is more stringent, our technique will be applicable to fewer *Kepler* planets.

2.2.2 Rotational and Tidal Potentials

It is well known from classical mechanics, that if stars and planets are considered to be purely spherical masses, then they will obey a simple r^{-2} force law and hence execute closed elliptical orbits. Non-spherical mass effects are caused by the application of external potential(s): the centrifugal potential of spinning bodies causes rotational flattening and the tidal potential of a nearby mass

¹In elliptical orbits, if the inclination is not 90° , the photometric minima do not exactly coincide with the planetary conjunctions. See Kopal (1959), p. 388 and section 2.3.3 below.

²Throughout this work, we do not distinguish between M_{tot} and M_* , since $M_p \ll M_*$.

raises tidal bulges. Rotational and tidal bulges create gravitational quadrupole fields (r^{-3}) that lead to orbital precession.

The complex subject of how planets³ respond to applied potentials is encapsulated in the so-called theory of figures (Zharkov & Trubitsyn, 1978). As long as the distortions are small, we can simplify the problem by ignoring the small interaction terms between the tidal and rotational potentials; in this paper, we thus restrict ourselves to the first order theory, where the two planetary responses simply add. Even in the linear case, the way the fluid planet responds depends on the full radial density structure of the planet. The planetary response is conveniently captured in a single variable k_{2p} , using the definition

$$V_2^{\text{ind}}(R_p) \equiv k_{2p} V_2^{\text{app}}(R_p) \quad (2.1)$$

where k_{2p} is the Love number of the planet, which is just a constant of proportionality between the applied second degree potential field V_2^{app} and the resulting field that it induces V_2^{ind} at the surface of the planet. Due to the orthogonality of the Legendre polynomials used to express the gravity field, if the planet is responding to a second degree harmonic field, then only the second degree harmonic of the planet’s gravity field is altered, to first-order. Thus, k_{2p} is a measure of how the redistribution of mass caused by the applied potential actually affects the external gravity field of the planet. In the stellar literature, the symbol k_2 is used for the apsidal motion constant, which is half of the secular/fluid Love number that we use throughout this paper (Sterne, 1939a).

The Love number k_2 is an extremely useful parameterization, as it hides the complex interactions of a planet and an applied potential in just a single number. The process of calculating k_2 of a fluid object (like stars and gas giants), from the interior density distribution is fairly straightforward and outlined in several places (e.g., Sterne, 1939a; Kopal, 1959). Objects with most of their mass near their cores, like stars, have very low k_2 values (~ 0.03 for main sequence solar-like stars, Claret, 1995) since the distorted outer envelope has little mass and therefore little effect on the gravity field. Planets have much flatter density distributions, and thus distortions of their relatively more massive outer envelopes greatly affect the gravity field. At the upper extreme lies a uniform density sphere, which has $k_2 = 3/2$. In this way, k_2 can be thought of as a measure of the level of central condensation of an object, with stronger central condensation corresponding to smaller k_2 .

By examining the variations in k_2 for giant planets within our own Solar System, we can gain a feel for its expected values and how sensitive it is to internal structure. The $n = 1$ polytrope is commonly used to approximate the density structure of (cold) gas giant planets; it has $k_2 \approx 0.52$ (Kopal, 1959). This can be compared to the value determined from the gravity measurements of Jupiter, where $k_{2J} \simeq 0.49$. Even though Jupiter may have a 10 Earth mass core, it is small in comparison to Jupiter’s total mass, and thus it has minor effect on the value of k_2 . Saturn, on the

³For clarity, in these sections we focus on the planetary shape, though the derivations are also valid for stars.

other hand has a roughly 20 Earth mass core and is less than 1/3 of Jupiter’s mass. As a result, the presence of Saturn’s core is easily seen in the value of its Love number $k_{2S} \approx 0.32$. From this, we can see that planets with and without significant cores differ in k_{2p} by about ~ 0.1 . This can also be inferred from Barnes & Fortney (2003) by using the Darwin-Radau relation to convert the moment of inertia factor to k_2 . Furthermore, Bodenheimer et al. (2001) list the moment of inertia factors of various planet models of HD 209458 b and τ Bootis b, which correspond to a range of k_{2p} values from ~ 0.1 to ~ 0.6 .

Current methods for inferring the internal structures of extra-solar planets combine measurements of the mass and radius with a model to obtain estimates of the planet’s implied composition and core size. Unfortunately, these models require one to make assumptions about the degree of differentiation, among other things (Baraffe et al., 2008). A good measurement of k_{2p} , however, reveals important independent structure information, which can break the degeneracies between bulk composition and the state of differentiation. Given such a wide range of potential k_{2p} values, even an imprecise measurement of k_{2p} will be extremely valuable for understanding extra-solar planets. By measuring the k_{2p} values for extra-solar planets, we can also uncover constraints on the density structure that are independent of the measurement of the planetary radius. This new information may allow us to probe the unknown physics responsible for the currently unexplained radius anomalies.

2.2.2.1 Induced External Gravity Field

The internal structures of planets in our own solar system are most readily characterized by the zonal harmonics of the planet’s gravity field, i.e., J_2 , J_4 , etc. It is these high-order harmonics that are directly measured by spacecraft flybys. To better understand the connection between the two, we can relate the k_2 formulation to J_2 by writing out the expression for the induced potential at the surface of the planet in Equation 2.1 in terms of the definition of J_2 , yielding: $k_{2p} V_2^{\text{app}}(R_p) = -J_2 \frac{GM_p}{R_p} P_2(\cos \theta)$, where P_2 is the usual Legendre polynomial and θ is the planetary co-latitude (Murray & Dermott, 1999). We can use this equation to obtain expressions for the J_2 field induced by both rotation and tides (discussed in more detail below). The relation relies on dimensionless constants which compare the strength of the acceleration due to gravity with that of the rotational and tidal potentials:

$$q_r = \frac{\nu_p^2 R_p^3}{GM_p} \quad \text{and} \quad q_t = -3 \left(\frac{R_p}{r} \right)^3 \left(\frac{M_*}{M_p} \right) \quad (2.2)$$

where ν_p is the angular spin frequency of the planet. For the case where the spin axis and tidal bulge axis are perpendicular (i.e., zero obliquity), the relationship between J_2 and k_2 is, to first order:

$$J_2 = \frac{k_2}{3} \left(q_r - \frac{q_t}{2} \right) \quad (2.3)$$

Note that q_t is a function of the instantaneous orbital separation, r , and is thus constantly changing in an eccentric orbit in response to the changing tidal potential. Hence J_2 for eccentric extra-solar planets is a complex function of time. This is why it is more sensible to analyze the orbital precession in terms of k_2 , which is a fixed intrinsic property of the planet, rather than J_2 .

As very hot Jupiters are expected to be synchronously locked (denoted by s) with small eccentricities, it can easily be shown that $q_t^s \approx -3q_r$, which simplifies equation 2.3 yielding:

$$J_{2p}^s \simeq \frac{5}{6} k_{2p} q_r \simeq \frac{5}{6} k_{2p} \left(\frac{M_*}{M_p} \right) \left(\frac{R_p}{a} \right)^3 \quad (2.4)$$

Using a moderate value of $k_{2p} = 0.3$, the J_2 of very hot Jupiters reaches as high as 5×10^{-3} , about half of the measured J_2 of Jupiter and Saturn.

2.2.3 Apsidal Precession

The quadrupole field created by rotational and tidal potentials discussed above induces precession of the star-planet orbit. Both Jupiter and Saturn have rather significant quadrupoles, dominated entirely by their sizeable rotational bulges resulting from rapid rotation periods of less than 10 hours. In contrast, very hot Jupiters are expected to be synchronously rotating, and thus their spin periods are longer by a factor of a few. Since the rotational bulge size goes as the square of the spin frequency, very hot Jupiters should have rotational bulges that are at least an order of magnitude smaller than Jupiter and Saturn, inducing only tiny quadrupole fields. These extra-solar planets are extremely close to their parent stars, however, with semi-major axes of only ~ 6 stellar radii. Very hot Jupiters are thus expected to have large tidal bulges which are shown below to dominate the quadrupole field and resulting apsidal precession.

2.2.3.1 Precession Induced by Tidal Bulges

The orbital effect of tidal bulges is complicated by their continuously changing size. While tidal bulges always point directly⁴ at the tide-raising object, their size is a function of orbital distance. Since the height of the tidal bulge depends on the actual separation between the objects, the second-order gravitational potential is time-varying in eccentric orbits. Accounting for this dependence (which cannot be captured by using a fixed J_2) is critical, as illustrated by Sterne (1939a). The

⁴We can ignore the lag due to dissipation, which has an angle of only $Q_p^{-1} \lesssim 10^{-5}$ for giant planets (Goldreich & Soter, 1966; Murray & Dermott, 1999).

dominant tidal perturbation to the external gravity field of the planet, evaluated at the position of the star, is a second-order potential:

$$V_{tid}(r) = \frac{1}{2}k_2GM_*R_p^5r^{-6} \quad (2.5)$$

The apsidal precession due to the tidal bulge, including the effect of both the star and the planet is (Sterne, 1939a; Eggleton & Kiseleva-Eggleton, 2001):

$$\begin{aligned} \dot{\omega}_{\text{tidal}} &= \dot{\omega}_{\text{tidal},*} + \dot{\omega}_{\text{tidal},p} \\ &= \frac{15}{2}k_{2*} \left(\frac{R_*}{a}\right)^5 \frac{M_p}{M_*} f_2(e)n \\ &+ \frac{15}{2}k_{2p} \left(\frac{R_p}{a}\right)^5 \frac{M_*}{M_p} f_2(e)n \end{aligned} \quad (2.6)$$

where n is the mean motion and $f_2(e)$ is an eccentricity function:

$$\begin{aligned} f_2(e) &= (1 - e^2)^{-5} \left(1 + \frac{3}{2}e^2 + \frac{1}{8}e^4\right) \\ &\approx 1 + \frac{13}{2}e^2 + \frac{181}{8}e^4 + \dots \end{aligned} \quad (2.7)$$

Note that the factor of 15 does not appear for stationary rotational bulges, as detailed below, and comes through Lagrange's Planetary Equations from the higher dependence on radial separation (r^{-6}) in the tidal potential. For this reason, tidal bulges are much more important in producing apsidal precession.

Furthermore, the main factor of importance to extra-solar planets is the mass ratio, which comes in because the height of the tide is proportional to the mass of the tide-raising body. Consider the ratio of the planetary and stellar effects:

$$\frac{\dot{\omega}_{\text{tidal},p}}{\dot{\omega}_{\text{tidal},*}} = \frac{k_{2p}}{k_{2*}} \left(\frac{R_p}{R_*}\right)^5 \left(\frac{M_*}{M_p}\right)^2 \simeq 100 \quad (2.8)$$

For tidal bulges, the apsidal motion due to the planet clearly dominates over the contribution of the star. Even though the planet's radius is smaller than the star's by a factor of ten, the star is so much more massive than the planet that it raises a huge tidal bulge, which consequently alters the star-planet orbit. The benefit provided by the inverse square of the small mass ratio is compounded by the order of magnitude increase in k_2 of the planet over the star.

2.2.3.2 Precession Induced by Rotational Bulges

The quadrupolar gravitational field due to the planetary rotational bulge, evaluated at the star's position is:

$$V_{\text{rot}}(r) = \frac{1}{3}k_2\nu_p^2R_p^5r^{-3}P_2(\cos\alpha_p) \quad (2.9)$$

where α_p is the planetary obliquity, the angle between the orbit normal and the planetary spin axis. Sterne (1939a) assumes zero obliquity and calculates the secular effect of this perturbation on the osculating Keplerian elements. This final result, including the effect of both the star and the planet is⁵:

$$\begin{aligned} \dot{\omega}_{\text{rot}} &= \dot{\omega}_{\text{rot},*} + \dot{\omega}_{\text{rot},p} \\ &= \frac{k_{2*}}{2} \left(\frac{R_*}{a}\right)^5 \frac{\nu_*^2 a^3}{GM_*} g_2(e)n \\ &+ \frac{k_{2p}}{2} \left(\frac{R_p}{a}\right)^5 \frac{\nu_p^2 a^3}{GM_p} g_2(e)n \end{aligned} \quad (2.10)$$

where $g_2(e)$ is another eccentricity function:

$$g_2(e) = (1 - e^2)^{-2} \approx 1 + 2e^2 + 3e^4 + \dots \quad (2.11)$$

Evaluating the importance of this effect requires an understanding of the spin states of very hot Jupiters and their stars. The rotation and spin pole orientation of very hot Jupiters should be tidally damped on timescales $\lesssim 1$ MYr (e.g., Dobbs-Dixon et al., 2004; Ferraz-Mello et al., 2008). We therefore assume that all planets have reached the pseudosynchronous rotation rate derived by Hut (1981). The rotation rate of the star is usually much slower since the tidal stellar spin-up timescale is much longer than ~ 1 GYr (Fabrycky et al., 2007).

If both the star and the planet were spinning synchronously, the stellar and planetary rotational bulges would have comparable contributions to apsidal precession. However, since the tidal bulge of the planet is a much more important effect, we find that even fast-spinning stars have a very weak contribution to apsidal precession.

2.2.3.3 Total Apsidal Precession

The other major contributor to the apsidal precession in extra-solar planetary systems is general relativity. The anomalous apsidal advance of Mercury's orbit due to its motion near the massive Sun was one of the first confirmations of general relativity. This same apsidal advance is prevalent in very hot Jupiter systems and has been shown to be possibly detectable through long-term transit

⁵The full equation, including arbitrary obliquities, is given in Kopal (1978), Equation V.3.18 (see also Sterne, 1939a; Eggleton & Kiseleva-Eggleton, 2001). Also recall that, unlike these authors, we use the symbol k_2 to represent the Love number which is twice the apsidal motion constant called k_2 in eclipsing binary literature.

timing (Miralda-Escudé, 2002; Heyl & Gladman, 2007; Pál & Kocsis, 2008; Jordan & Bakos, 2008). The relativistic advance is given (to lowest order) by:

$$\dot{\omega}_{GR} = \frac{3GM_*n}{ac^2(1-e^2)} \quad (2.12)$$

One additional effect for non-synchronous planets is due to thermal tides (Arras & Socrates, 2009), which create a bulge on the planet due to temperature-dependent expansion of an unevenly-radiated upper atmosphere. The thermal tidal bulge is very small in mass and is not expected to provide a significant contribution to apsidal precession (P. Arras, pers. comm.) and is thus neglected.

Since we are considering only the lowest-order effects, all the apsidal precession rates (rotational/tidal for the star/planet and general relativity) simply add to give the total apsidal precession (roughly in order of importance for very hot Jupiters):

$$\dot{\omega}_{tot} = \dot{\omega}_{tid,p} + \dot{\omega}_{GR} + \dot{\omega}_{rot,p} + \dot{\omega}_{rot,*} + \dot{\omega}_{tid,*} \quad (2.13)$$

We are ignoring the small cross-terms (geodetic precession, quadrupole-quadrupole coupling, Lense-Thirring effect, nutation, etc.) for the purposes of this paper as higher-order corrections.

Calculating each of these contributions to the precession shows that *for very hot Jupiters, the dominant term in the total apsidal precession is due to the planetary tidal bulge*. For the known transiting planets, the fraction of apsidal precession due to the planet is calculated and illustrated in Figure 1. The precession due to the interiors of very hot Jupiters towers over the other effects. General relativity, the next largest effect is ~ 10 times slower than the precession caused by the planetary tidal bulge.

The apsidal precession rate of very hot Jupiters due solely to the interior structure of the planet is:

$$\begin{aligned} \dot{\omega}_p \approx & 3.26 \times 10^{-10} \text{ rad/sec} \times \left(\frac{k_{2p}}{0.3}\right) \left(\frac{M_*}{M_\odot}\right)^{3/2} \times \\ & \left(\frac{M_p}{M_J}\right)^{-1} \left(\frac{R_p}{R_J}\right)^5 \left(\frac{a}{0.025 \text{ AU}}\right)^{-13/2} \end{aligned} \quad (2.14)$$

which explains why low density very close-in Jupiters are the prime targets for measuring apsidal precession. For these planets, the precession rate can reach a few degrees per year.

The precession due to the planet has generally been neglected in extra-solar planet transit timing work to date (Miralda-Escudé, 2002; Heyl & Gladman, 2007), which has considered stellar oblateness or general relativity to be the dominant effects (in the absence of other planets) though Jordan & Bakos (2008) have also pointed out that $\dot{\omega}_{tidal,p}$ can be an important source of apsidal precession. We

find that the planetary quadrupole is usually 1-2 orders of magnitude more important than effects previously considered for single very hot Jupiters. Hence, measuring apsidal precession essentially gives $\dot{\omega}_{\text{tid,p}}$ which is directly proportional to k_{2p} , implying that transit light curve variations due to apsidal precession can directly probe the interiors of extra-solar planets.

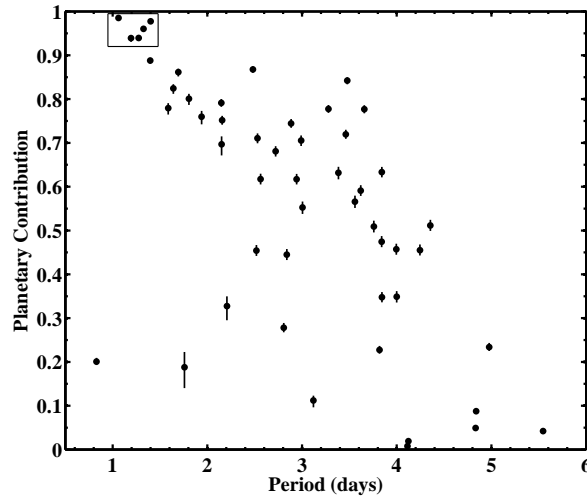


Figure 2.1

Fraction of Apsidal Precession Due to the Planetary Quadrupole. The points show the planetary fraction of the total apsidal precession calculated for the known transiting extra-solar planets with properties taken from J. Schneider’s Extra-Solar Planet Encyclopedia (<http://www.exoplanet.eu>), assuming the planet has a typical Love number of $k_{2p} = 0.3$ (e.g. Saturn-like). The apsidal precession induced by the tidal and rotational bulges of the planet overcome precession due to general relativity and the star, especially for short period planets. The ”error bars” show the range of planetary contributions for a 5% variation in stellar masses (and hence $\dot{\omega}_{GR}$) and the comparatively smaller effect of varying the stellar Love number and rotation rate over all reasonable values. The five cases where the planetary contribution to apsidal precession is most important (boxed) also have the shortest precession periods: WASP-12b, CoRoT-1b, OGLE-TR-56b, WASP-4b, and TrES-3b would fully precess in about 18, 71, 116, 120, and 171 years, respectively. The planet in the lower left is CoRoT-7, a super-Earth planet whose planetary contribution to precession is small because of its small radius. Transiting planets with periods longer than 6 days all had planetary contributions less than 0.15. In all cases, the dominant signal in apsidal precession of very hot Jupiters is k_{2p} , which is determined by their internal density distribution and is a powerful probe into their interior structure.

2.2.4 Modification of the Mean Motion

Non-Keplerian potentials also modify the mean-motion, n , and cause a small deviation from Kepler's Third Law. Including the effects described above, the non-Keplerian mean motion, n' , is (dropping second-order corrections):

$$n' = n \left(1 + \epsilon - \frac{3GM_*}{2ac^2} \right) \quad (2.15)$$

where ϵ is defined as

$$\begin{aligned} \epsilon = & \frac{k_{2*}}{2} q_{r,*} \left(\frac{R_*}{a} \right)^2 + \frac{k_{2p}}{2} q_{r,p} \left(\frac{R_p}{a} \right)^2 \\ & + 3k_{2*} \frac{M_p}{M_{tot}} \left(\frac{R_*}{a} \right)^5 + 3k_{2p} \frac{M_*}{M_p} \left(\frac{R_p}{a} \right)^5 \end{aligned} \quad (2.16)$$

and $n^2 \equiv \frac{GM_{tot}}{a^3}$. The general relativistic correction to the mean motion is from Soffel (1989). (Throughout this paper, except where noted, the difference between n' and n is ignored as a higher-order correction.)

As with apsidal precession, the planetary quadrupole is more important than the stellar quadrupole by about 2 orders of magnitude. At the largest, the correction to the mean motion is a few times 10^{-5} . Iorio (2006) used the fact that quadrupole moments cause deviations to Kepler's Third Law to attempt to derive the J_2 of the star HD 209458 (the quadrupole of the planet was incorrectly ignored).

However, as Iorio (2006) found, this method is only feasible if you know the masses and semi-major axes of the orbit *a priori* or independently from Kepler's Law. Since the error in stellar masses (from radial velocities and evolutionary codes) is usually 3-10 % (e.g., Torres et al., 2008), the propagated error on k_{2p} would be a few times greater than the highest k_{2p} expected, making this method impractical. It has been proposed that the stellar mass and semi-major axis can be precisely and independently measured via the light-travel time effect described by Loeb (2005). In practice, however, the light-travel time effect is highly degenerate with the unknown transit epoch and/or the orbital eccentricity. We find that a precise independent measurement of M_* from light-travel time is impractical even with the excellent photometry of *Kepler*.⁶

2.2.5 Expectations for Planetary Eccentricities

Thus far, we have quantified how planetary interiors affect the orbit through precession. The photometric observability of this apsidal precession is highly dependent on the current orbital eccentricity (e). Small eccentricities are the largest limitation to using transit light curves to probe extra-solar

⁶We do note that detailed observations of multiple-planet systems can yield mass estimates of each of the bodies independently. *Kepler* asteroseismology can also provide independent information about stellar mass and other properties (Kjeldsen et al., 2008).

planet interiors. Indeed, if eccentricities are very low, measuring apsidal precession from transit light curves may not be possible for any of the *Kepler* planets.

Nearly all hot Jupiters have eccentricities consistent with zero, though the radial velocity technique has difficulty putting $3\text{-}\sigma$ upper limits on eccentricities smaller than 0.05 (Laughlin et al., 2005). So far, the strongest constraints are placed by comparing the deviation of the secondary transit time from half the orbital period, which are related by (e.g., Charbonneau et al., 2005):

$$e \cos \omega \simeq \frac{\pi}{2P_{\text{orb}}} (t_{\text{sec}} - t_{\text{prim}} - \frac{P_{\text{orb}}}{2}) \quad (2.17)$$

Similarly, by measuring the primary and secondary transit durations (Θ_I and Θ_{II}), an additional constraint can be placed on $e \sin \omega$. The equation commonly quoted in the extra-solar planet literature (Kallrath et al., 1999; Charbonneau, 2003; Winn et al., 2006) has a sign error; the correct equation is derived by Kopal (1959), p. 391 :

$$e \sin \omega = \frac{\Theta_{II} - \Theta_I}{\Theta_{II} + \Theta_I} \frac{\alpha^2 - \cos^2 i}{\alpha^2 - 2 \cos^2 i} \quad (2.18)$$

where $\alpha \equiv \frac{R_* + R_p}{a\sqrt{1-e^2}}$. The accuracy of this measurement is typically smaller than for $e \cos \omega$, but we include this equation to note that there is information about both the eccentricity and its orientation in the full transit light curve (see also Bakos et al., 2009).

Combining secondary transit timing information with radial velocity and Rossiter-McLaughlin measurements to help constrain ω , Winn et al. (2005) found the best-fit eccentricity for HD 209458 was ~ 0.015 . Though Winn et al. (2005) argue that the actual eccentricity is probably less than 0.01, it is not necessarily 0 (Mardling, 2007). Recently, Joshi et al. (2008) revealed WASP-14b, a young massive hot Jupiter with an eccentricity of 0.1; WASP-10b and WASP-12b also appear to be eccentric (Christian et al., 2008; Hebb et al., 2009), though these eccentricities may be spurious or overestimated.

The most accurate eccentricity constraint is a detection by Knutson et al. (2007a) for the very hot Jupiter HD189733b. They observed continuously and at high cadence (0.4 seconds) with the Spitzer space telescope and measured a secondary timing offset corresponding to $e \cos \omega = 0.001 \pm 0.0002$, a $5\text{-}\sigma$ result that they could not explain by any other means. (Preliminary analysis of additional data for this planet by Agol et al. (2009) indicates $e \cos \omega = 0.0002 \pm 0.0001$.) The constraint on $e \sin \omega$ is much weaker. A non-zero eccentricity of $e \simeq 0.003$ for hot Jupiters is therefore consistent with every measurement available in the literature, though the actual values of eccentricities at the 10^{-3} level are essentially unconstrained.

In the absence of excitation, the current eccentricities of these planets depend on the initial eccentricity and the rate of eccentricity decay. Extrapolating from planets in our solar system

(Goldreich & Soter, 1966) implies short circularization timescales of $\simeq 10$ MYr, though recent studies have shown that using a fixed eccentricity damping timescale is an inappropriate simplification of the full tidal evolution (e.g., Jackson et al., 2008; Levrard et al., 2009; Rodriguez & Ferraz-Mello, 2009). Even an analysis using the full tidal evolution equations cannot give a compelling case for the present-day eccentricities of these planets, since there are essentially no direct constraints on the tidal dissipation parameter for the planet, Q_p . Various estimates show that Q_p for exoplanets is not known and may be quite large (e.g., Matsumura et al., 2008), implying that non-zero eccentricities are not impossible. Even so, we stress that the best candidates for observing apsidal precession are also those planets that have the fastest eccentricity damping, since the damping timescale and apsidal precession rates are both proportional to $\frac{M_p}{M_*} \left(\frac{a}{R_p}\right)^5$. Hence, those planets which have the fastest precession rates will also have the lowest eccentricities. The first step in determining if this trade-off allows for apsidal precession to be measured by *Kepler* data is to apply the techniques described in this paper to the data themselves. Furthermore, with the discovery and long-term characterization of more planets using ground and space-based observations, the detectability of apsidal precession will increase dramatically.

We should note that there are several mechanisms that can excite eccentricities and compete with or overwhelm tidal dissipation. The most prevalent is assumed to be eccentricity pumping by an additional companion (Peale et al., 1979; Bodenheimer et al., 2001; Adams & Laughlin, 2006). Even very small (Earth-mass or less) companions in certain orbits can provide significant eccentricity excitation (Mardling, 2007). (In this case, however, our single-planet method for estimating k_{2p} would need to be modified considerably.) Tidal dissipation in rapidly rotating stars tends to increase the eccentricity, potentially prolonging circularization in some systems (Ferraz-Mello et al., 2008). Very distant inclined companions (e.g., a planet orbiting a star in a misaligned binary star system) can induce Kozai oscillations that impart very large eccentricities on secular timescales (e.g., Fabrycky & Tremaine, 2007). Arras & Socrates (2009) proposed that thermal tides can significantly affect the orbital and rotational properties of extra-solar planets, though their conclusions appear to be overestimated (Goodman, 2009; Gu & Ogilvie, 2009). Finally, recent (not necessarily primordial) dynamical instabilities in the planetary system can also be responsible for generating eccentricity which simply hasn't damped away yet (Ford et al., 2005; Gomes et al., 2005; Chatterjee et al., 2007; Thommes et al., 2008). We, therefore, continue our analysis under the possibility that some very hot Jupiters may have non-zero eccentricities.

2.3 Transit Light Curves of Apsidal Precession

Previous studies of transit light curve variability due to non-Keplerian perturbations have focused almost exclusively on transit timing. In contrast, we model the full photometric light curve in order

to estimate the detectability of k_{2p} . This will automatically include the effect of changing transit durations, which are very useful for detecting apsidal precession (Pál & Kocsis, 2008; Jordan & Bakos, 2008). In addition, using full photometry can provide a more direct and realistic estimate of the detectability of k_{2p} . Of course, the drawback is additional computational cost, though we found this to be manageable, requiring less than 20 seconds to generate the ~ 2 million photometric measurements expected from *Kepler*'s 1-minute cadence over 3.5 years.

2.3.1 Our Transit Light Curve Model

Determining the photometric light curve of a transiting system requires knowing the relative positions of the star and the planet at all times. These can be calculated by describing the motion of the planet with time-varying osculating orbital elements. When describing the motion of the planet using instantaneous orbital elements, it is usually customary to ignore the periodic terms by averaging, as in Sterne (1939a), and calculate only the secular terms. These small periodic terms describe how the orbital elements change within a single orbit as a function of the true anomaly, f , due to the non-Keplerian potential. In precessing systems, the value of the true anomaly at central transit, $f_{tr} \equiv 90^\circ - \omega_{tr}$, changes subtly from one transit to the next, inducing slow variations in the osculating orbital elements at transit. Therefore, we include in our model the dominant periodic changes in orbital elements as a function of orbital phase, using $M_{tr} \approx f_{tr}$ as an appropriate approximation for low eccentricities. Using a direct integration (described in Section 2.4.1), we verified that ignoring these periodic variations can cause non-negligible systematic errors in determining transit times. The periodic changes are derived from the same disturbing potentials used above. We follow the method of Kozai (1959) for calculating osculating elements from mean elements, and assume zero obliquity. The correction is similar to the correction to the mean motion, which is also applied in our model. The correction to the semi-major axis, eccentricity, longitude of periapse, and mean anomaly are $a_{osc} = a_{mean} + \frac{2ae}{1-e^2}\epsilon \cos M \approx 2ae\epsilon \cos M$, $e_{osc} = e_{mean} + \epsilon(1 - \cos M)$, $\omega_{osc} = \omega_{mean} + \frac{\epsilon}{e} \sin M$, and $M_{osc} = M_{mean} - \frac{\epsilon}{e} \sin M$ where ϵ is defined in Equation 2.16. General relativistic periodic corrections are also added; these are taken from Soffel (1989), page 92 (with $\alpha = 0$, $\beta = \gamma = 1$). Using our direct integrator (described below), we verified that these corrections reproduced the actual orbit to sufficient accuracy for this analysis as long as $e \gg \epsilon \sim 10^{-5}$. Other corrections are higher order in small parameters and are ignored.

Our model uses these corrected elements to generate astrometric Cartesian coordinates for a specific system inclination and, for completeness, also includes the effect of light-travel time (Loeb, 2005) though we concur with Jordan & Bakos (2008) and Pál & Kocsis (2008) that the light-travel time change due to $\dot{\omega}$ is unimportant. The positions are then translated to photometric light curves using the quadratic limb-darkening code⁷ described in Mandel & Agol (2002). *Kepler* data will have

⁷Available at <http://www.astro.washington.edu/agol/transit.tar.gz>

enough signal-to-noise to justify using non-linear limb darkening laws (Knutson et al., 2007b), but we do not expect that this simplification will significantly alter our conclusions.

In addition, we include the photometry of the secondary eclipse. As suggested by López-Morales & Seager (2007), very hot Jupiters can reach temperatures exceeding 2000 K, where their blackbody emission at optical wavelengths is detectable by *Kepler*. This thermal emission is added to the reflected light of the planet, which appears to be small based on the low upper limit of the albedo of HD 209458b and TrES-3 measured by Rowe et al. (2007) and Winn et al. (2008), respectively. We find that in *Kepler*'s observing bandpass of 430-890 nm (Koch et al., 2006), thermal emission of very hot Jupiters can dominate over the weak reflected light. We estimate the depth of the secondary eclipse (d_{sec}) in our simulated *Kepler* data by assuming that 1% of the light is reflected and the other 99% absorbed and reemitted as processed thermal blackbody emission from the entire planetary surface (day and night sides). To be conservative and to account for unmodeled non-blackbody effects, we divide the resulting planet/star flux ratio by 2 (Hood et al., 2008); the resulting depth of around 2×10^{-4} is consistent with the lower values of Burrows et al. (2008), the tentative measurement of the thermal emission from CoRoT-2b (Alonso et al., 2009), and the detection of secondary eclipse emission from OGLE-TR-56b (Sing & López-Morales, 2009). We note that the best candidates for detecting k_{2p} are those with small semi-major axes and large radii; these same planets have relatively large d_{sec} values (Table 1). Secondary eclipses are very useful for determining e and ω . We will also find that they can be important for observing apsidal precession.

Our model generates accurate photometry for an extra-solar planet undergoing apsidal precession. Several other small photometric effects have been discussed in the literature, which we do not include. Most of these effects are periodic (e.g., the reflected light curve) and therefore will not affect the long-term trend of precession. Care will need to be taken to ensure that slow changes due to parallax and proper motion, which should be quite small for relatively distant stars observed by *Kepler* (Rafikov, 2008; Scharf, 2007) or changes in the stellar photosphere (Loeb, 2008) are not significant. Non-Gaussian astrophysical noise of the star and other systematic noise should degrade the accuracy with which k_{2p} can be measured compared to our ideal photometry. The long-term variability of the star can be interpolated away or modeled (Lanza et al., 2009), though it is not clear how short-term variability will affect transit light curves at *Kepler*'s level of precision. On the other hand, complimentary observations (e.g., warm Spitzer, HST, radial velocities, JWST, etc.) should only enhance our understanding of the systems studied.

2.3.2 Accuracy of k_{2p} Measurement

With an accurate photometric model of apsidal precession, one could estimate the measurement accuracy of k_{2p} from *Kepler* data by carrying out a full Monte Carlo study of the inversion problem, going from realistic synthetic photometric data sets to a determination of all system parameters. In

this work, instead, we carry out a much simpler calculation which cannot provide strict one-sigma error estimates like the Monte Carlo analysis, but does give an indication of how well k_{2p} can be resolved given a large dataset.

We obtain this accuracy estimate by comparing a realistic precessing photometric model with $k_{2p} \neq 0$ to a base model with $k_{2p} = 0$. The base model is still undergoing very slow apsidal precession, induced by general relativity and k_{2*} . We calculate the effect of a non-zero k_{2p} value by subtracting the precessing model from the base model. (See Figures 2.2 and 2.4.) Then, by calculating the root-sum-square of the residual signal and comparing it to the photometric error on a single data point, we obtain a numerical measure of the relative signal induced by k_{2p} . The “signal-to-noise” ratio for the data set is therefore given by:

$$\frac{S}{N} \sim \frac{\sqrt{\sum_i (y_i - y_i^0)^2}}{\sigma} \quad (2.19)$$

where y_i and y_i^0 are the photometry model values for the k_{2p} test model and the base model, respectively, and σ is the photometric error. We use $\sigma = 1000$ parts per million (ppm) flux per 1-minute integration, corresponding to the expected noise of *Kepler* on a faint $V = 14$ star (Koch et al., 2006). Of the 30 planets with periods less than 3 days, 16 are expected to be brighter than $V \simeq 14$ (T. Beatty, pers. comm.) and we can reasonably expect some fraction of these to have orbits comparable to the planets modeled here.

Since our residual signal changes as a function of time, this is not a true signal-to-noise calculation; the distribution of values in time matters for a proper interpretation, but any distribution would yield the same effective $\frac{S}{N}$, and thus this construction is not capturing all of the details. Even so, it does provide a useful and reasonable rough estimate for detectability. In order to identify the resolution on the k_{2p} measurement, we search for the value of k_{2p} which yields a signal-to-noise of $\frac{S}{N} = 1$. This is reasonable since it represents the threshold value of k_{2p} , below which planetary induced precession cannot be distinguished in the data with the given errors. The threshold k_{2p} value can also be loosely thought of as an estimate of the $1\text{-}\sigma$ expected errors.

This is a realistic estimate only insofar as the residual signal ($y_i - y_i^0$) is due only to k_{2p} and cannot be absorbed by any other parameters. Hence we seek to choose other parameters so as to minimize the residuals without changing k_{2p} . For most system parameters, this is accomplished by referencing the time to the center of the data set, and thus the difference between the signals grows similarly forward and backward in time as seen in Figures 2.2 - 2.5. The transit shapes in both models are equivalent at the center of the dataset as would be expected in an analysis of actual data.

Additionally, a major effect from changing the precession period is to alter the observed average period. When analyzing actual data, this would just be absorbed into a small adjustment to the

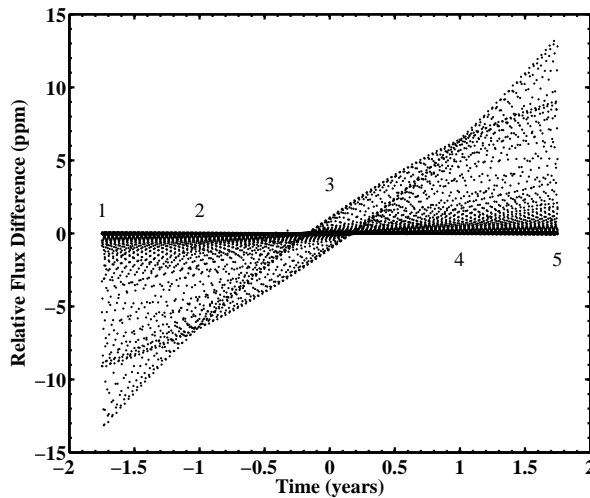


Figure 2.2 **Photometric Difference Signal from k_{2p}** . As described in the text, we use the difference between two theoretical light curves in the transit photometry to assess the observability of apsidal precession by *Kepler*. For WASP-4b at $\omega = 0^\circ$, $e = 0.003$, and a central impact parameter, the difference between a model with $k_{2p} = 0$ and $k_{2p} = 0.146$ would yield an effective “signal-to-noise” of 1 on a moderately bright star ($V = 14$). Shown is this difference signal; the root sum of squares of the signal is equal to 1000 ppm, the expected photometric accuracy of *Kepler* for a 1 minute observation (Koch et al., 2006). The trends seen in the figure are illustrated in Figure 2.3 by considering excerpts of single primary transits from the regions labeled 1-5.

(unknown) stellar mass, thereby adjusting the period to absorb much of the k_{2p} signal. It is therefore important to correct for the average period change to avoid significantly overestimating the signal due to k_{2p} . Additionally, there is a similar, though less severe, effect for the epoch of the first transit, which is also adjusted to best absorb signal. This is achieved by using an analytic expression for the transit times (see Equation 2.22 below) which match the transit times of the photometric model to very high accuracy. By fitting a line to these times, we can determine the average period and epoch that absorb the degenerate portions of the k_{2p} signal, leaving behind the residual due only to k_{2p} . We have not explicitly accounted for degeneracies between the signal from k_{2p} and the other parameters, like the radius, limb darkening, and system inclination, but since k_{2p} induces a time varying signal while these other parameters are generally constant, there is little expected signal absorption from these parameters.

The only major drawback of this approach is that it does not allow the eccentricity state of the system to change. With real data, the eccentricity and precession phase are not known in advance, and thus must be found by inversion. As detailed in Section 2.2.5, eccentricity and orbital orientation are primarily constrained by comparing primary and secondary transit pairs, and thus proper inversion is greatly aided by accurate observations in wavelengths more favorable to secondary transit observations, obtained by Spitzer, HST, or from the ground (e.g., Knutson et al., 2007a;

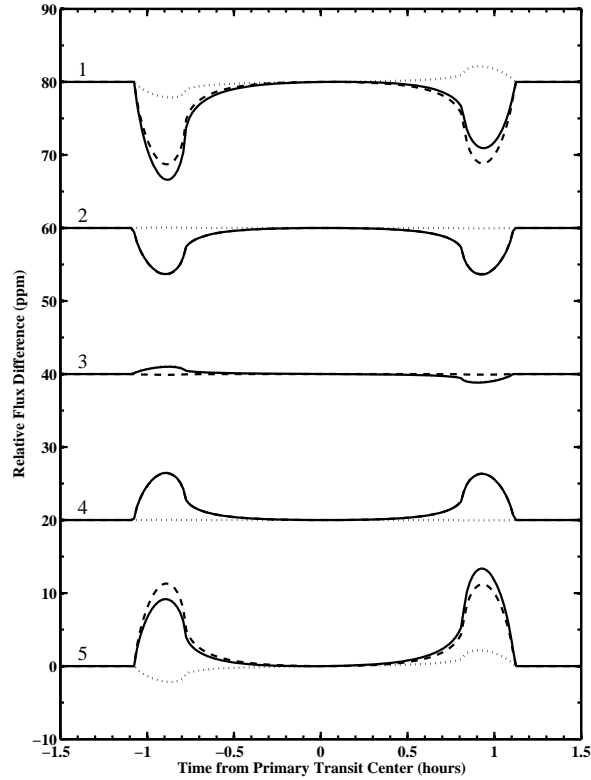


Figure 2.3 **Excerpts of Photometric Difference Signal.** Examining excerpts of the residual signal shown fully in Figure 2.2, the effects of transit timing and “transit shaping” can both be seen. The five excerpts are offset for clarity. Transit timing has an asymmetric signal (dotted lines), obtained when subtracting two transit curves slightly offset in time. Transit shaping, which is mostly due to changing transit duration, creates a symmetric signal (dashed lines). The total difference signal (solid lines) is dominated by the effect of transit shaping, which has ~ 30 times more signal than transit timing alone. (See explanation in text.) Both effects are maximized at the beginning (1) and end (5), as expected for a signal that increases with longer baseline. The maximal signal occurs during ingress and egress, when the light curve changes the fastest. The transit shapes are equivalent at the center (3) by construction. The transit timing anomaly of precession is quadratic, which, when fitted with a best-fit straight line corresponding to a non-precessing signal, yields two intersections when transit timing is minimized (2,4). The transit timing offset at the beginning and end is only 0.085 seconds, while the center is offset by -0.042 seconds.

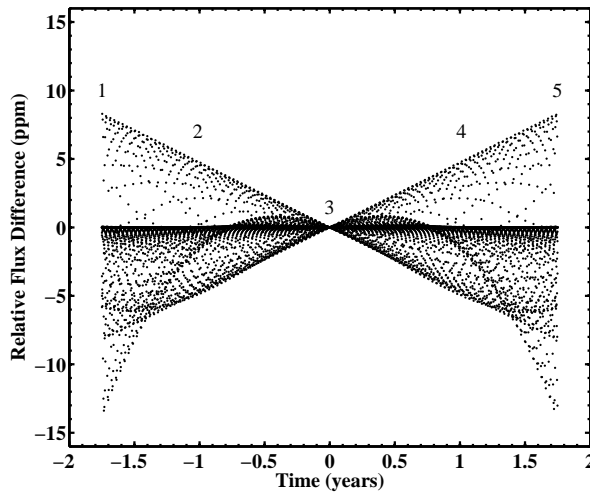


Figure 2.4 **Photometric Difference Signal from k_{2p}** . Similar to Figure 2.2, but for $\omega = 90^\circ$. This figure is dominated by the photometric difference between secondary transits slightly offset in time. At $\omega = 90^\circ$ the changes in the primary transits due to precession are small, except far away from the central time. At this orientation, the primary-secondary timing offset (Equation 2.17) is maximized. This “secondary transit timing” signal is weaker than the signal from primary transit as the secondary transit depth is much shallower. Therefore, an unreasonably high k_{2p} of 0.925 is required to detect the apsidal precession. Excerpts of single secondary transits taken from regions labeled 1-5 are shown in Figure 2.5.

Swain et al., 2008; Gillon et al., 2008). We also find that binned and folded *Kepler* data has comparable sensitivity to a single Spitzer observation for characterizing the secondary eclipses of very hot Jupiters. In any case, our assessment of the threshold k_{2p} assumes that the eccentricity of the system is very well known, which will likely require additional supporting observations.

2.3.3 Comparison to Expected Signal

The residual light curves calculated for each planet, Figures 2.2 - 2.5, match the theoretical expectations of the apsidal precession signal (Miralda-Escudé, 2002; Heyl & Gladman, 2007; Pál & Kocsis, 2008; Jordan & Bakos, 2008). To interpret the results of our analysis, it will be useful to briefly review the major components of the apsidal precession signal: changes in the times of primary transits, changes in the shape of primary transits, and changes in the primary-secondary offset times (Miralda-Escudé, 2002; Heyl & Gladman, 2007; Pál & Kocsis, 2008; Jordan & Bakos, 2008).

The primary transit times, T_N , due to apsidal precession are well described by a sinusoid for very low eccentricities ($e \ll 0.1$):

$$T_N = T_0 + NP_{\text{obs}} + \frac{eP_{\text{obs}}}{\pi}(\cos \omega_{tr,N} - \cos \omega_{tr,0}) \quad (2.20)$$

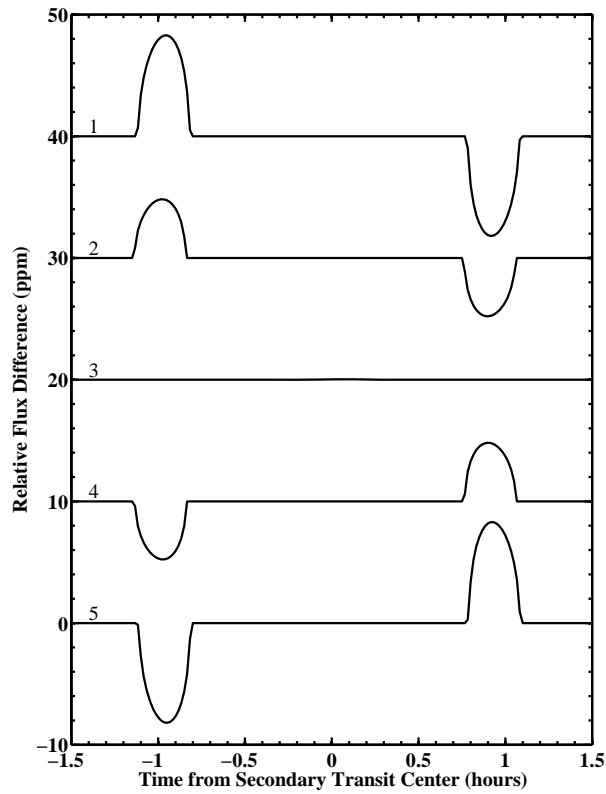


Figure 2.5 **Excerpts of Photometric Difference Signal.** Similar to Figure 2.3, but for $\omega = 90^\circ$. Single secondary transit differences are excised from the full difference signal shown in Figure 2.4. The shape of the curves is due to the subtraction of two secondary transits slightly offset in time. Since the secondary transits are complete occultations, they are flat-bottomed and lack the additional structure due to limb-darkening seen in Figure 2.3. By construction, the offset grows in time away from the center (3) of the signal and attains a maximum at the beginning (1) and end (5). Curves 2 and 4 are shown for comparison to Figure 2.3.

where T_0 is the epoch of the first transit, $\omega_{tr,N} \equiv \dot{\omega}(T_N - T_0) + \omega_{tr,0}$ is the argument of periapse for the N^{th} transit, and P_{obs} is the *observed* period between successive transits, which deviates from the actual orbital period since the orbit has precessed a small amount between transits (Batten, 1973). For small eccentricities, the amplitude of the transit timing variations due to k_{2p} is:

$$\frac{eP_{\text{obs}}}{\pi} \simeq 119 \text{ sec} \times \left(\frac{e}{0.003}\right) \left(\frac{a}{0.025 \text{ AU}}\right)^{3/2} \left(\frac{M_*}{M_\odot}\right)^{-1/2} \quad (2.21)$$

Given that individual transit times can be measured with accuracies of only a few seconds, even tiny eccentricities $e \lesssim 10^{-5}$ can induce detectable transit timing variations on precessional timescales ($\sim \dot{\omega}^{-1}$).

For our analysis, we extended Equation 2.20 to fifth order in eccentricity allowing accurate determination of transit times for eccentricities up to of order 0.1. We also require a correction for the effect of a non-central impact parameter ($i < 90^\circ$, $e > 0$). For an inclined eccentric orbit, the apparent path of the planet across the stellar disk is curved. At orientations where the line of sight is not along the major axis of the ellipse, the curved path is also asymmetric. Therefore, the times of photometric minima, T_N , do not correspond exactly to the times of conjunction (when the planet crosses the $y - z$ plane and $f_{tr} \equiv 90^\circ - \omega_{tr}$). We follow the correction from Equation VI.9-21 of Kopal (1959), who find that at photometric minimum, $f_{tr} = 90^\circ - \omega'_{tr}$, where $\omega'_{tr} \equiv \omega_{tr} + e \cos \omega_{tr} \cot^2(i)(1 - e \sin \omega_{tr} \csc^2(i))$; in this corrective term, it is only required to keep terms up to second order in eccentricity. Assuming that i and $\dot{\omega}$ are constant, it can be shown that

$$\begin{aligned} T_N &= T_0 + NP_{\text{obs}} \\ &+ \frac{P_{\text{obs}}}{\pi} \left[e(\cos \omega'_{tr,N} - \cos \omega'_{tr,0}) \right. \\ &+ \frac{3}{8}e^2(\sin 2\omega'_{tr,N} - \sin 2\omega'_{tr,0}) \\ &+ \frac{1}{6}e^3(\cos 3\omega'_{tr,N} - \cos 3\omega'_{tr,0}) \\ &+ e^4 \left(\frac{1}{16}(\sin 2\omega'_{tr,N} - \sin 2\omega'_{tr,0}) \right. \\ &- \left. \frac{5}{64}(\sin 4\omega'_{tr,N} - \sin 4\omega'_{tr,0}) \right) \\ &+ e^5 \left(\frac{1}{16}(\cos 3\omega'_{tr,N} - \cos 3\omega'_{tr,0}) \right. \\ &- \left. \frac{3}{80}(\cos 5\omega'_{tr,N} - \cos 5\omega'_{tr,0}) \right) \left. \right] \end{aligned} \quad (2.22)$$

This transcendental equation is solved iteratively for $(T_N - T_0)$ to obtain the transit times and has been tested thoroughly against the empirical determination of transit times calculated by our light

curve model described above.

The expected apsidal precession periods (including small contributions from GR and the star) for WASP-12b, CoRoT-1b, OGLE-TR-56b, WASP-4b, and TrES-3b are around 18, 71, 116, 120, and 171 years, respectively. In other words, they have precession rates induced by the planetary tidal bulge of a few degrees per year, compared to a few degrees per century as the fastest general relativistic precession (Jordan & Bakos, 2008). We caution that if $\frac{R_p}{a}$ for WASP-12b is overestimated due to imprecise data (e.g., Winn et al., 2007), then the precession period would increase accordingly.

Even with such fast precession rates, the duration of observations will generally be much shorter than the precession period. In addition, as discussed above, the linear timing anomalies will be absorbed into the effective period as a small change in the unknown stellar mass (Heyl & Gladman, 2007; Pál & Kocsis, 2008; Jordan & Bakos, 2008). Therefore, detection of apsidal precession from primary transit times alone will require a significant detection of the curvature over a small portion of a long-period sinusoid. Since the curvature in Equation 2.20 is maximal at $\omega \approx 0, 180^\circ$, these orientations have the best primary transit timing signal. Even at these orientations, detecting k_{2p} from primary transit times alone is difficult, since it can be shown that the signal strength is proportional to $e\dot{\omega}^2$, due to the need to detect curvature (Heyl & Gladman, 2007).

When the observational baseline is much shorter than the decades-long precession period, utilizing the changing shape of the transits can significantly improve detectability of apsidal precession (Pál & Kocsis, 2008; Jordan & Bakos, 2008). Transit shapes are primarily determined by the orbital speed at transit \dot{f}_{tr} and impact parameter b , both of which depend on the precession phase ω_{tr} . For small eccentricities, the orbital angular speed at transit is given simply by $\dot{f}_{tr} \simeq n(1 + 2e \cos \omega_{tr})$. Changes in the impact parameter are somewhat more subtle, since b is given by $r_{tr} \cos i / R_*$, where $r_{tr} \simeq a(1 - e^2)/(1 + e \sin \omega_{tr})$ is the star-planet separation. Hence, the apparent impact parameter of the planet can change for non-central transits, even when the orbital plane remains fixed. The evolving transit shape of precessing orbits is determined by variations in both orbital speed and impact parameter. Simplifying the effect of transit shape by considering only the variations in transit duration as a function of ω_{tr} , Pál & Kocsis (2008) and Jordan & Bakos (2008) find that these two effects are of comparable magnitude. These authors also show analytically that the two effects exactly cancel when $b = 1/\sqrt{2}$. At this impact parameter, the transit duration stays constant throughout apsidal precession. The full photometric transit shape, however, still changes detectably in a precessing orbit, though the magnitude of signal is reduced (Figure 2.7).

The expected effect of changing transit shapes is fully consistent with the photometric difference signals calculated by our model (Figures 2.2 and 2.3). Indeed, our model shows that transit shaping dominates the signal by a factor of $\gtrsim 30$ (Figure 2.3). We can also see that changes in the transit shape are maximized at orientations near $\omega \approx 0, 180^\circ$ (as expected from Equation 2.18).

For small eccentricities, the transit shaping signal strength is given by $\frac{S}{N} \propto e\dot{\omega} \propto ek_{2p}$. Therefore,

when transit shaping dominates the observable signal, we should find that searching for the threshold k_{2p} value that yields $\frac{S}{N} = 1$ results in a power law relationship between threshold k_{2p} and e , such that $k_{2p} \propto e^{-1}$. By solving for threshold k_{2p} for eccentricities from 0.001 to 0.1, we find, as expected, that threshold k_{2p} very closely follows a power law in eccentricity with a slope of -1 for all planets. This power law relationship can be written as $ek_{2p} = C$, where C is a constant calculated from our model that depends on the planetary, orbital, and stellar parameters of the system.

At $\omega \approx 90, 270^\circ$, transit timing and transit shaping effects are much weaker and are rather ineffective at constraining apsidal precession. At these orientations (when the Earth’s line of sight is nearly aligned with the major axis of the orbit), another photometric signal emerges: variations in the difference between the times of primary and secondary transits. The changing orientation of the orbital ellipse causes a variation in the offset between primary and secondary transit times following Equation 2.17 above (Heyl & Gladman, 2007; Jordan & Bakos, 2008). These authors show that the strength of this signal is also proportional to $e\dot{\omega}$ and we find that the variation in threshold k_{2p} then also follows $k_{2p} \propto e^{-1}$.

The photometric difference signal at $\omega = 90^\circ$ is shown in Figures 2.4 and 2.5. Using the method described in Section 2.3.2 to remove degeneracies almost eliminates the primary transit signal entirely, as expected, and the secondary transit offset becomes the more powerful signal. For WASP-12b, with an expected *Kepler* secondary transit depth of ~ 1830 ppm, the threshold k_{2p} is actually *lower* at $\omega = 90^\circ$ (Figure 2.6). For the other planets, the secondaries are not as important.

Our estimates of threshold k_{2p} at $\omega = 90^\circ$ are based on the unknown secondary transit depth (d_{sec}) in the *Kepler* bandpass (though our estimates of d_{sec} are consistent with all the measurements in the literature to date). Furthermore, we find that $\frac{S}{N} \propto d_{\text{sec}}$, so that deeper secondary transits improve the accuracy with which k_{2p} can be measured. It is important to note that combining *Kepler* primary transit times with precise secondary transit times measured in the near-infrared (e.g., by warm Spitzer, HST, or JWST) is a very powerful way to constrain apsidal precession (Heyl & Gladman, 2007) for any orientation. Even a few high-precision secondary eclipse observations are enough to lower the value of threshold k_{2p} from our predictions, especially when $\omega \approx 90, 270^\circ$.

By construction, threshold k_{2p} values vary linearly with the assumed photometric error $\sigma = 0.001 \times 10^{0.2(V-14)}$. In addition, re-performing our analysis using a 6-year long *Kepler* mission improved threshold k_{2p} values by a common factor of ~ 2.2 .

2.3.4 Results for Specific Planets

Using the method described above, we have determined the threshold k_{2p} for the most favorable known transiting planets as analogs for the very hot Jupiters to be discovered by *Kepler*. The threshold k_{2p} for each planet was computed at a range of eccentricities from 0.001 to 0.1 and for $\omega = 0^\circ$ and $\omega = 90^\circ$. Using the relationship discussed above ($k_{2p} \propto e^{-1}$) we interpolated (and

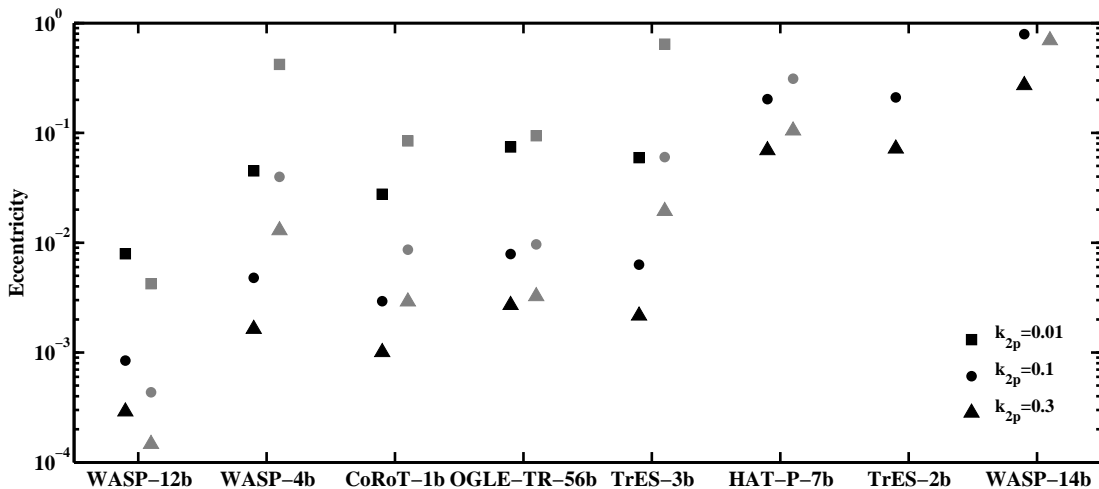


Figure 2.6 **Eccentricities Needed to Detect Interior Properties from Apsidal Precession.** The best-known planets for detecting k_{2p} precession are analogs to the hot Jupiters WASP-12b, WASP-4b, CoRoT-1b, OGLE-TR-56b, TrES-3b, HAT-P-7b, TrES-2b, and WASP-14b. Assuming that analogs to these planets exist in the *Kepler* field around a $V=14$ magnitude star, the above graph shows the eccentricities required to detect k_{2p} . Black symbols correspond to calculations with $\omega = 0^\circ$ and gray symbols correspond to $\omega = 90^\circ$; in both cases, $b = 0$. Apsidal precession is much easier to detect for larger eccentricities so increasing e decreases the detectable k_{2p} . Using our transit light curve model, we found that threshold k_{2p} values followed a power law $k_{2p} \propto e^{-1}$ (for low eccentricities), which is consistent with the analytical estimates that $\frac{S}{N} \propto e\dot{\omega} \propto ek_{2p}$ (see Section 2.3.2). Interpolating (and sometimes extrapolating) on this power law relationship, the graph identified the eccentricities required of these analog planets to detect precession due to a “typical” planetary interior of $k_{2p} = 0.3$ (triangles). For example, when $e = 0.00026$ and $\omega = 0^\circ$, the apsidal precession due to an analog of WASP-12b should be just detectable by *Kepler*. A higher eccentricity (shown in Table 1) would be needed to measure k_{2p} with sufficient accuracy (0.1) to distinguish between a massive core and a core-less model (circles). Systematic errors are expected to become important once the measurement error on k_{2p} reaches as low as 0.01 (squares). If any of the very hot Jupiters discovered by *Kepler* have comparable eccentricities, the long-term high-precision photometry would allow for a powerful probe into their interior structure. HAT-P-7b and TrES-2b are known to lie in the *Kepler* observing field, but the values above are not corrected for improved photometric accuracy obtainable on these bright stars. Note that the eccentricities shown above and in Table 1 are computed for $\frac{S}{N} = 1$; $3\text{-}\sigma$ measurements require eccentricities 3 times as high.

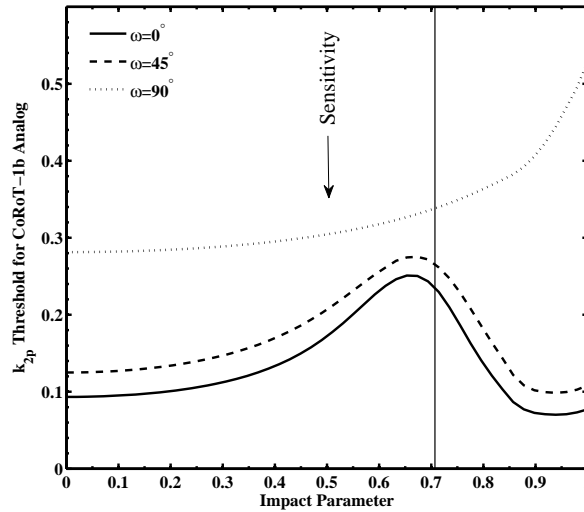


Figure 2.7 **Effect of Impact Parameter on Precession Signal.** The detectability of apsidal precession depends on the impact parameter (b) of the orbital track across the star. For $\omega = 0^\circ$ (solid), the signal of primary transits are most important, with transit shaping playing the largest role. (See Figure 2.3.) However, the strength of transit shaping is a function of impact parameter with the minimum effect analytically estimated by Jordan & Bakos (2008) and Pál & Kocsis (2008) to be $b = 1/\sqrt{2}$ (vertical solid line). Using a full photometric model, we see the expected decrease in the shaping signal (i.e., requiring a larger k_{2p} to reach $\frac{S}{N} = 1$). Note that the signal is nearly maximal, with small threshold k_{2p} values, for a large range of impact parameters. When $\omega = 90^\circ$ (dotted), the effect of primary transits are minimal and the offset in secondary transits become the determining factor. (See Figure 2.4.) At high impact parameters secondary eclipses are grazing, reducing the observable signal. We also show the threshold k_{2p} for an orientation of $\omega = 45^\circ$, which lies, as expected, between the two extremes. The values of threshold k_{2p} shown are for an $V=14$ CoRoT-1b analog in the *Kepler* field with an eccentricity of 0.003.

Table 2.1. Extra-Solar System Parameters and Results

Planet Analog	M_*	R_*	M_p	R_p	a	$d_{\text{sec}}^{\text{b}}$	$\dot{\omega}_{\text{tot}}$	e (Threshold $k_{2p}=0.1$) ^c		Threshold	Thresh.	Ref
	M_{\odot}	R_{\odot}	M_J	R_J^{a}	AU	ppm	$^{\circ}/\text{yr}$	$\omega = 0^{\circ}$	$\omega = 90^{\circ}$	\dot{P}^{d} ms/yr	Q_*^{d}	
WASP-12b	1.35	1.57	1.41	1.79	0.0229	1830	19.9	0.0008	0.0004	0.95	92700	1
CoRoT-1b	0.95	1.11	1.03	1.55	0.0245	314	4.96	0.0028	0.0085	0.93	12500	2,3
WASP-4b	0.92	0.91	1.24	1.36	0.0234	109	2.91	0.0047	0.0394	0.68	9900	4
TrES-3b	0.93	0.83	1.91	1.34	0.0228	106	2.04	0.0062	0.0614	0.53	13700	5
OGLE-TR-56b	1.17	1.32	1.29	1.30	0.0236	451	3.00	0.0077	0.0096	1.36	24700	6
HAT-P-7 b	1.47	1.84	1.77	1.36	0.0377	176	0.25	0.2085	0.3146	6.73	2800	7
TrES-2 b	0.98	1.00	1.19	1.22	0.0367	18	0.13	0.2102	...	2.94	350	8
WASP-14b	1.21	1.31	7.34	1.28	0.0360	144	0.09	0.8352 ^e	...	3.92	5400	9
XO-3 b	1.21	1.37	11.8	1.22	0.0454	46	0.04	8.00	1700	10
HAT-P-11b	0.81	0.75	0.081	0.42	0.0530	0.2	0.01	29.2	0.1	11
CoRoT-7b	0.91	1.02	0.028	0.16	0.0170	8	0.29	16.8	80	12

References. — (1) Hebb et al. (2009) (2) Bean (2009) (3) Barge et al. (2008) (4) Winn et al. (2009a) (5) Sozzetti et al. (2009) (6) Pont et al. (2007b) (7) Pál et al. (2009) (8) Holman et al. (2007) (9) Joshi et al. (2009) (10) Johns-Krull et al. (2008) (11) Bakos et al. (2009) (12) www.exoplanet.eu^f

Note. — These system parameters were used to estimate the detectability of apsidal precession for these very hot Jupiter systems. The derivation of the values in the remaining columns is described in the text and in the footnotes below. For all systems, $k_{2*} = 0.03$ and quadratic limb darkening parameters $u_1 = 0.35$ and $u_2 = 0.4$ (appropriate for *Kepler*'s bandpass) were used (Mandel & Agol, 2002). For reference, the measured eccentricity of WASP-12b, WASP-14b, HAT-P-11b, and XO-3b are 0.049 ± 0.015 , 0.091 ± 0.003 , 0.198 ± 0.046 , and 0.2884 ± 0.0035 respectively. Other planets have unmeasured eccentricities or eccentricity upper limits of $\lesssim 0.05$. A discussion of these results is provided in Section 2.3.4.

^aWe use $R_J \equiv 71492$ km, the equatorial radius at 1 bar.

^bThe estimated depth of the secondary transit in *Kepler*'s bandpass (see Section 2.3.1).

^cThe eccentricity required (at two different values of ω) so that a k_{2p} difference of 0.1 has an effective signal-to-noise of 1 in all of *Kepler* data for a $V=14$ star, corresponding to a photometric accuracy of 1000 ppm/min. If analogs to these planets were found by *Kepler* with the given eccentricities, the internal density distribution would be measured well enough to detect the presence of a large core (see Section 2.3.2). These values correspond to the circles in Figure 2.6. These results are for central transits (for $b > 0$, see Figure 2.7).

^dThe value of the change in period, \dot{P} , that can be detected with a signal-to-noise of 1 in all of *Kepler* data for a $V=14$ star (see Section 2.4.2). The value of threshold Q_* is an estimate of the maximum value of the stellar tidal dissipation parameter, Q_* , assuming that the period decay is due entirely to tidal evolution of the planet. Lower values of Q_* are detectable by *Kepler*. Stars are thought to have time-averaged Q_* values around 10000, though this value is highly uncertain and could be much higher for individual stars.

^eEven with the precision of *Kepler*, apsidal precession for these planets is undetectable. The extrapolation used to compute eccentricities at specific values of threshold k_{2p} assumes the inverse relationship discussed in the text $k_{2p} \propto e^{-1}$, which is only true for low eccentricities.

^fThis ultra-short period low-mass planet was recently announced by the CoRoT team, but has not been published in a peer-reviewed journal. We take the parameters from J. Schneider's Extra-solar Planets Encyclopedia and use the mass-radius relation for terrestrial super-Earths of Sotin et al. (2007) to estimate the mass as ~ 9 Earth masses (rather than using the quoted upper limit of 17 Earth masses).

sometimes extrapolated) our calculations to determine the eccentricity required to reach threshold k_{2p} values of 0.3, 0.1, and 0.01. These results are summarized in Figure 2.6 and Table 1.

WASP-12b is the best candidate for observing apsidal precession. With an eccentricity of $e \simeq 0.00026$ and $k_{2p}=0.3$, the apsidal precession would have an effective signal-to-noise of ~ 1 for all of *Kepler* data. If e is ~ 0.001 , then k_{2p} can be well characterized and not just detected. As the difference in k_2 between Jupiter and Saturn of ~ 0.15 is primarily due to the presence of a massive core, a resolution in k_{2p} of 0.1 is enough to detect whether or not the planet has a core, at the ~ 1 -sigma level.

Although WASP-12b does not lie in the *Kepler* field, it clearly stands out as an excellent candidate for observing apsidal precession. Though the putative eccentricity of 0.049 (Hebb et al., 2009) is probably an overestimate (Laughlin et al., 2005), if it were real, it would cause sinusoidal transit timing deviations with an amplitude of ~ 25 minutes (using Equation 2.20) and a period of ~ 18 years. Such a large deviation would be readily observed from the ground in either transit times or transit shapes. If apsidal precession is not observed, tight upper limits on the eccentricity can be established.

Analogous to the very hot Jupiters WASP-4b, TrES-3b, CoRoT-1b, and OGLE-TR-56b are good candidates for observing apsidal precession if the eccentricities are above ~ 0.003 . (Note that CoRoT-1b has only ~ 30 days of observations from the *CoRoT* satellite (Barge et al., 2008), which is insufficient to observe any of the effects discussed in this paper.) These planets have precession periods of around 100 years so that the argument of periape of these planets changes by $\sim 10^\circ$ during the course of *Kepler* observations. Though none of these planets lie in the *Kepler* field, they are all good candidates for observing apsidal precession through precision photometry.

WASP-14b is more massive and has a larger semi-major axis (0.035 instead of 0.025) which is enough to significantly reduce the detectability of apsidal precession which only proceeds at 0.1° per year. Unlike the previously mentioned planets, WASP-14b has a known non-zero eccentricity of 0.091 ± 0.003 (Joshi et al., 2009). Thus, the amplitude of transit timing variations is known to be very large (~ 97 minutes), but with a ~ 3400 year precession period.

CoRoT-7b is a very hot super-Earth and has the shortest known orbital period (excepting the ultra-short period planets of Sahu et al. 2006). We included this planet in our analysis to get a feel for the plausibility of detecting the interior structure of terrestrial extra-solar planets. The small radius reduces the planetary contribution to apsidal precession (Figure 1) and significantly reduces the photometric signal. We note here that in bodies where material strength (rigidity) is more important than self-gravity, k_{2p} is no longer directly related to internal density distribution. The correction factor is typically small for bodies larger than the Earth (Murray & Dermott, 1999).

XO-3b is a super-massive eccentric planet that is not in the *Kepler* field. Even so, it is interesting to note that, using the known eccentricity $e = 0.2884 \pm 0.0035$ (Winn et al., 2009b) and accounting

for the brightness of the host star ($V=9.8$), the *Kepler* threshold k_{2p} is reduced to only 0.54. As pointed out by Jordan & Bakos (2008) and Pál & Kocsis (2008), XO-3b is a good candidate for observing apsidal precession within the next decade or so. Furthermore, as discussed below, the non-zero obliquity of the stellar spin axis (Winn et al., 2009b) may also result in an observable signal due to nodal precession.

HAT-P-7b and HAT-P-11b are orbiting bright stars in the *Kepler* field. The latter is an eccentric hot Neptune with a relatively large semi-major axis resulting in no eminently detectable apsidal precession. HAT-P-7b, on the other hand, is a good candidate for detecting apsidal precession. It is probably one of the brightest hot Jupiters in the *Kepler* field, orbiting a $V=10.5$ star. The system brightness improves the expected photometric accuracy from 1000 ppm/min to 200 ppm/min, implying that an eccentricity of only 0.014 is needed to detect apsidal precession (threshold $k_{2p}=0.3$). Pál et al. (2009) report a best-fit eccentricity of 0.003 ± 0.012 , indicating that the necessary eccentricity cannot be ruled out. Furthermore, this planet has transiting data extending back to 2004 and was observed by NASA’s *EPOXI* Mission in 2008 (Christiansen et al., 2009; D. Deming, pers. comm.). This additional baseline, though sparsely sampled, may provide the additional leverage needed to detect apsidal precession if the eccentricity is non-zero. Note, however, that detecting changes in transit shapes is more difficult when the observations are made with a variety of telescopes because transit shapes depend on the observing filter used, due to wavelength-dependent limb darkening.

TrES-2b is similar to HAT-P-7b in that it also lies in the *Kepler* field, has observations dating to 2005, and was observed by NASA’s *EPOXI* Mission. TrES-2b is somewhat fainter than HAT-P-7b ($V=11.4$), and, correcting for the system brightness, an eccentricity of 0.021 would result in detectable apsidal precession (threshold $k_{2p}=0.3$). Observations of the secondary eclipse show no detectable deviations of the orbit from circularity (O’Donovan et al., 2009). Even so, the light curve of this planet is quite sensitive to perturbations as it has a quite high impact parameter $b = 0.854$. Accounting for this impact parameter does not significantly change the required eccentricity.

We conclude that *Kepler may detect the cores of very hot Jupiters* and probe their interior structure through their evolving transit light curve if eccentricities are above ~ 0.003 . As future observations provide longer baselines for these observations, the sensitivity to interior structure measurements will increase dramatically, significantly lowering the eccentricity needed to observe apsidal precession.

In cases where apsidal precession is not observed, the data can set strong upper limits on planetary eccentricities. An upper limit on the eccentricity can be inferred by assuming that the planet has the minimal physically-plausible value of $k_{2p} \approx 0.1$. Null detections of apsidal motion should therefore provide upper limits on eccentricity comparable to the values shown in Table 1 (also shown by circles in Figure 2.6). Such strong eccentricity constraints are valuable for improving our understanding of these close-in planets.

2.4 Potential Confusion of the Apsidal Precession Signal

In the above, we have assumed that measuring $\dot{\omega}$ is tantamount to measuring k_{2p} . This is justified by noting that the conversion $\dot{\omega}$ to k_{2p} involves only factors that are very well characterized. In Section 2 and Figure 1, we showed that k_{2p} is usually the dominant source of apsidal precession. The effects of k_{2*} and general relativity are well-understood and can typically be subtracted away without introducing serious uncertainty, even when they dominate the apsidal precession rate. From Equation 2.6, converting the remaining $\dot{\omega}_p$ to k_{2p} requires only knowing $\frac{M_p}{M_*}$, e , $\frac{R_p}{a}$, and n . The latter two are very accurately measured with even a few transit light curves (e.g., Torres et al., 2008; Southworth, 2008). The eccentricity only enters the equation through the $f_2(e)$ and $g_2(e)$ eccentricity functions (Equations 2.7 and 2.11), and *Kepler* observations of secondary eclipse are sufficiently accurate to remove any systematic error due to these terms unless the eccentricity is large ($e \gtrsim 0.3$). Determining the mass ratio requires well-sampled radial velocity observations. The systems detected by *Kepler* are bright enough to get good mass measurements, especially since very hot Jupiters have large radial velocity amplitudes ($K \sim 200$ m/s).⁸ The anticipated error in the mass ratio is a few percent (Torres et al., 2008). In all, we estimate that, converting from $\dot{\omega}$ to k_{2p} leads to a typical systematic error on k_{2p} of around ~ 0.01 . This is a relatively small systematic effect in comparison to the potential range (~ 0.5) of k_{2p} values. For reference, the eccentricity required to reach a threshold k_{2p} of 0.01 is shown in Figure 2.6 by squares.

Another way to introduce systematic errors on the measurement of k_{2p} is to misinterpret similar transit light curve variations. To ensure that the method outlined in this paper truly probes the interiors of extra-solar planets, we consider in this section whether the transit light curve resulting from apsidal precession can be confused with any other common circumstances. Although a very specific combination of parameters is required for any particular phenomenon to successfully mimic a signal due to k_{2p} , the below effects should be reconsidered when actual data is available.

2.4.1 Testing the Effect of Obliquity

If either the star or planet has a non-zero obliquity, the orbital plane will no longer be fixed as a result of nodal precession. The obliquities of very hot Jupiters rapidly ($\lesssim 1$ MYr) decay to a Cassini state, and recent work has shown that these planets are likely in Cassini state 1 (Winn & Holman, 2005; Levrard et al., 2007; Fabrycky et al., 2007). Using a model based on the equations of Eggleton & Kiseleva-Eggleton (2001), we found that Cassini obliquities of very hot Jupiters are indeed negligible ($\alpha_p < 0.01^\circ$). Though tidal damping of the stellar obliquity occurs on far longer timescales, several measurements of the projected stellar obliquity through the Rossiter-McLaughlin

⁸Other than determining the mass ratio and constraining the eccentricity, radial velocity information is thought to have a negligible contribution in constraining apsidal precession unless a serious observational campaign can measure the radial velocity period (independently of transits) to sub-second accuracies. (Heyl & Gladman, 2007; Jordan & Bakos, 2008).

effect indicates that planet-hosting stars generally have low obliquities $\lesssim 10^\circ$ like the Sun (Fabrycky & Winn, 2009). Hence, the general expectation is that both the star and planet will have rather low, but potentially non-zero obliquities.

Understanding the specific orbital evolution resulting from non-zero obliquities is more complicated than the simple prescription for apsidal precession. To correctly account for non-Keplerian effects, we wrote a direct integrator, following Mardling & Lin (2002), that calculates the Cartesian trajectory (and the direction of the spin axes) of a star-planet system including general relativity and the effects of quadrupolar distortion. This integrator reproduces the orbit-averaged analytic equations of Mardling & Lin (2002), which are the same as those in Eggleton & Kiseleva-Eggleton (2001), Sterne (1939a), and elsewhere.⁹ We did not include the effects of tidal forces or additional planets which are not relevant to our problem.

Using this direct integrator, we investigated the effect of non-zero obliquities on the transit times, durations, and impact parameters. Integration of several cases with varying stellar and planetary obliquities showed that the largest effect on the photometry was due to changes in the impact parameter, as expected for an orbit with changing orientation (Miralda-Escudé, 2002). However, even for large stellar obliquities ($\sim 45^\circ$) the transit light curve variations due to obliquity are generally small relative to the effects of purely apsidal precession, even with low eccentricities. One reason for this is that the tidal bulge, which does not contribute to nodal precession, is $\gtrsim 15$ times more important than the rotational bulge. As with apsidal precession, the planetary contribution to orbital variations is much stronger than the stellar contribution (for equal obliquities). Unless the planetary obliquity is unexpectedly large ($\gtrsim 0.5^\circ$), the obliquity-induced nodal precession should have only a minor effect on the transit light curve.

2.4.2 Transit Timing due to Orbital Decay

Orbital decay generates a small secular trend in transit times. Sasselov (2003) proposed the detectability of the expected ~ 1 ms/yr period change due to semi-major axis decay of OGLE-TR-56b. The transit timing anomaly due solely to orbital decay (or growth) is the result of constantly accumulating changes in the period:

$$T_N \simeq T_0 + NP_{\text{obs}} + \frac{1}{2}N^2\delta P \quad (2.23)$$

where $\delta P \equiv \dot{P}$ is the change in the period during one orbit and N is the number of transits after the initial transit. Equation 2.23 can be derived by noting that the transit times are basically the integral of the instantaneous period. As before, the transit timing anomaly is composed of the

⁹This involved minor modifications to the "direct integrator" equations 3 and 5 in Mardling & Lin (2002). In Equation 3, the coefficient 12 should be a 6 (R. Mardling, pers. comm.) and Equation 5 was replaced with the nearly equivalent equation from Soffel (1989).

quadratic deviation of T_N from a straight line. The change in period can be due to magnetic stellar breaking (e.g., Lee et al., 2009; Barker & Ogilvie, 2009a), the Yarkovsky effect applied to planets (Fabrycky, 2008a), and/or other effects.

For planets orbiting an asynchronously rotating star, a major source of orbital decay is tidal evolution, which results in a slow change in semi-major axis, according to the formula (Murray & Dermott, 1999):

$$\dot{a} = \text{sign}(\nu_* - n) \frac{3k_{2*}}{Q_*} \frac{M_p}{M_*} \left(\frac{R_*}{a} \right)^5 na \quad (2.24)$$

where $\text{sign}(x)$ returns the sign of x or 0 if $x = 0$ and where Q_* is the tidal quality parameter of the star, typically around 10^4 (Dobbs-Dixon et al., 2004). Though δP due to tidal dissipation is only of order 3 micro-seconds, N grows by ~ 300 each year, reaching ~ 1000 during the duration of *Kepler* for very hot Jupiters. This implies a transit timing signal of about a few seconds.

Calculating the total “signal-to-noise” of tidal evolution, as was done for k_{2p} , we find that reasonable values of Q_* can be measured even for faint stars ($V = 14$; 1000 ppm/min noise). For a circular orbit with the parameters of OGLE-TR-56b, the effective $\frac{\dot{S}}{N}$ reaches 1 when \dot{P} is 1.36 ms/yr (see Table 1), corresponding to $Q_* \approx 25000$. This implies the detectability of most of the empirically-motivated estimates of Sasselov (2003) for the tidal decay of OGLE-TR-56b, which are estimated to be within an order of magnitude of 1 ms/yr. On the other hand, Barker & Ogilvie (2009b) estimate that the tidal damping in F-stars like OGLE-TR-56 and WASP-12 may be very low, which may explain the survival of these short period planets.

The estimates of the threshold values of \dot{P} , shown in Table 1, include removing degeneracies in other parameters, except apsidal precession of eccentric orbits, and assume that everything but \dot{P} is known. Note that the transit light curve signal due to orbital decay is due entirely to transit timing; the change in a is far too small to observe in transit shaping. As the signal due to apsidal precession includes significant changes to the shapes of the transits, the signal due to k_{2p} is qualitatively different than that of Q_* . The shifting of secondary transits from precession also help in this regard, as outlined above. However, the primary transit timing signals can be similar: quadratic transit timing anomalies with amplitudes of ~ 1 second.

Kepler analogs of very hot Jupiters WASP-12b, OGLE-TR-56b, CoRoT-1b, WASP-4b, and TrES-3b could have detectable transit timing anomalies due to tidal decay, implying a direct measurement of the current value of Q_* for specific stars (Table 1). This is an exciting possibility, providing the first direct measurements (or constraints) of the currently unknown details of tidal dissipation in a variety of individual stars.¹⁰ We also note that interesting orbital decay of eclipsing binary systems seen by *Kepler* could also be detectable.

¹⁰The vanishingly small effect of eccentricity decay is $\sim \frac{1}{Q_p}$ smaller than apsidal precession, so that direct measurements of Q_p from eccentricity decay are not feasible.

2.4.3 Confusion Due to Other Planets

Could the signal due to k_{2p} be confused with additional planets? In considering this issue, it should be noted that all known hot Jupiters (with $a \lesssim 0.05$ AU and $M_p \gtrsim 0.5M_{Jup}$) have no currently known additional companions. The apparent single nature of these systems could very well be due to observational biases (Fabrycky, 2008b). However, even for stars that have been observed for many years with radial velocity (e.g., 51 Peg, HD 209458), there appears to be a strong tendency towards hot Jupiters as the only close-in massive planets.

Previous studies of transit timing variations focus on the effects of additional planetary perturbers (e.g., Holman & Murray, 2005; Agol et al., 2005; Ford & Holman, 2007; Nesvorný & Morbidelli, 2008). These authors find that nearby massive planets or even low-mass planets in mean-motion resonances would cause strong transit timing variations that are easily distinguishable from the comparatively long-period timing anomalies due to k_{2p} . Relatively distant companions or non-resonant low-mass planets, however, can induce a linear apsidal precession signal just like k_{2p} (Miralda-Escudé, 2002; Heyl & Gladman, 2007; Jordan & Bakos, 2008). The precession rate induced by a perturbing body is a function of its mass and semi-major axis. The interior structure of very hot Jupiters causes apsidal precession as fast as a few degrees per year. To match this precession rate would require, for example, another Jupiter-mass planet at $\lesssim 0.1$ AU or a solar-mass star at ~ 1 AU. Even perturbers an order of magnitude smaller than these would be readily detectable using radial velocity observations and/or high-frequency transit time variations. When restricted to planets that are undetectable by other means, adding the precession due to the unknown perturbing planet would lead to an insignificant overestimate of k_{2p} for very hot Jupiters.¹¹ When observing transiting planets with larger semi-major axes ($a \gtrsim 0.05$ AU), the strength of planetary induced apsidal precession is reduced to a level comparable to apsidal precession from a low-mass perturbing planet (Jordan & Bakos, 2008) and confusion may be possible in these cases.

Since the transit timing signal for apsidal precession is similar to a sinusoid, another potential source of confusion would be light-travel time offsets due to a distant orbiting companion (e.g., Deeg et al., 2008). The transit timing signal due to stellar motion about the barycenter can be distinguished from k_{2p} precession¹² by considering the changes in transit shapes and primary-secondary transit time offsets, which are not affected by distant companions.

We conclude that transit timing effects from other planets can be readily distinguished from the effects of apsidal precession. To address the issue of the transit shaping signal due to additional planets, we wrote a simple three-body integrator (similar to the integrator mentioned above) to investigate the kinds of transit light curve signals created by additional planets. For the vast majority

¹¹Conversely, as a consequence of the fast precession of very hot Jupiters due to their (unknown) interiors, it will be very difficult to detect the presence of additional perturbing planets in these systems from apsidal precession alone.

¹²Transit time anomalies due to Q_* (Section 2.4.2), however, can be confused with barycenter light-travel time shifts due to a distant planet that may be undetectable in radial velocities.

of additional planet parameters, the transit timing deviations always carry far more signal than the minor deviations due to changes in the angular velocity¹³ (\dot{f}_{tr}) or impact parameter (b), which together determine the transit shape as described in Section 2.3.3 above. Generally, it is much easier to delay a transit by 5 seconds than it is to shift the apparent transit plane by an appreciable amount.

However, when the perturbing planet is on a plane highly-inclined to the transiting planet, changes in the transit shape can become detectable, even while the transit timing variations are negligible. For example, a perturbing planet of mass $10^{-5}M_*$ at 0.1 AU with a mutual inclination of 45° caused very hot Jupiter transit durations to change by ~ 1 second/year. This kind of signal is the result of nodal precession induced by the perturbing planet, as originally pointed out by Miralda-Escudé (2002). In our investigation, we found that the three-body nodal precession alters the impact parameter (b) but does not significantly affect the orbital angular velocity (\dot{f}_{tr}). Conversely, the transit shaping signal due to k_{2p} is generally produced by changes in both b and \dot{f}_{tr} , but at near-central transits, the effect of changing orbital velocity is dominant (see Section 2.3.3). In high-precision transit light curves, both the angular velocity and the impact parameter can be independently measured and hence the signals of apsidal and nodal precession are usually distinct for all but the most grazing transits.

Given the uniqueness of the apsidal precession signal induced by the planet’s interior, it appears that if additional planets are not detectable in radial velocities, transit timing variations, or nodal precession, then they will not contribute to a misinterpretation of an inferred value of k_{2p} for very hot Jupiters. Nevertheless, future measurements of k_{2p} should check that these issues are unimportant within the context of the specific system being studied.

Finally, we estimate that moons or rings with enough mass to bias an inferred k_{2p} would cause other readily detectable photometric anomalies (e.g., planet-moon barycentric motion Sartoretti & Schneider, 1999). In addition, extra-solar moons with any significant mass are tidally unstable, especially around very hot Jupiters (Barnes & O’Brien, 2002).

2.5 Other Methods for Determining k_{2p}

2.5.1 Secular Evolution of a Two Planet System

Measuring k_2 for an extra-solar planet was suggested by Wu & Goldreich (2002) for the inner planet of HD 83443. Unfortunately, later analyses have indicated that the supposed second planet in this system was actually an artefact of the sparse radial velocity data (Mayor et al., 2004). Nevertheless, this technique could be applied to other eccentric planetary systems with similar

¹³The angular velocity is directly related to the star-planet separation through conservation of angular momentum: $r\dot{f}^2$.

conditions (Mardling, 2007). Wu & Goldreich (2002) showed that in a regime of significant tidal circularization and excitation from an additional planet, the ratio of eccentricities depends on the precession rate which is dominated by k_{2p} as shown above (see also Adams & Laughlin 2006, who do not include precession due to the planetary quadrupole). In theory, the current orbital state of such multi-planet systems gives an indirect measurement of the apsidal precession rate.

2.5.2 Direct Detection of Planetary Asphericity

Another method for determining interior properties of transiting planets would be to directly measure the asphericity due to the rotational or tidal bulge in primary transit photometry. The height of the rotational and tidal bulges are $q_r h_2 R_p$ and $q_t h_2 R_p$, respectively, where q_r and q_t are the dimensionless small parameters defined in Equation 2.2 and h_2 is another Love number which, for fluid bodies, is simply $k_2 + 1$ (Sterne, 1939a). These bulges cause the disk of the planet to be slightly elliptical, subtly modifying the photometric signal, as discussed for rotational bulges by Seager & Hui (2002) and Barnes & Fortney (2003). However, as discussed by Barnes & Fortney (2003), in real systems with actual observations, the size of the rotational bulge is very difficult to determine as it is highly correlated with stellar and orbital parameters that are not known *a priori*, e.g., limb darkening coefficients.

The tidal bulge, whose height is also set by k_{2p} , does not suffer from some of the difficulties involved with measuring the rotational bulge. It has a known orientation (pointing towards the star) so there is no degeneracy from an unknown obliquity (Barnes & Fortney, 2003). (Note, however, that for hot Jupiters, the obliquities must be tidally evolved to nearly zero, so this isn't really a problem with the rotational bulge.) In addition, the signal due to oblateness is only significant near ingress/egress, but the tidal bulge is continuously changing orientation throughout the entire transit. Though the tidal bulge is typically three times larger than the rotational bulge (Equation 2), the projection of the tidal bulge that is seen during a transit is small, proportional to $\sin \theta$ where θ is the angle between the planet position and the Earth's line of sight. For very hot Jupiters that have semi-major axes of only $\lesssim 6$ stellar radii, $\sin \theta$ during transit ingress/egress reaches $\gtrsim \frac{1}{6}$ so that the projected tidal bulge is about half as large as the rotational bulge. The extra dimming due to the tidal bulges (and rotational bulges) is as high as 2×10^{-4} for some planets that are expected to have tides over 2000 km high (e.g., WASP-12b, WASP-4b, Corot-1b, OGLE-TR-56b); this compares very favorably with the photometric accuracy of binned *Kepler* data at about 10 ppm per minute. However, we expect that, as with the rotational bulge alone, the combined signal from the rotational and tidal bulge will be highly degenerate with the unknown limb-darkening coefficients, as the size of the projection of the tidal bulge also varies as the distance to the center of the star.

We note that using multi-color photometry should significantly improve the prospects of detecting non-spherical planetary transits since it breaks most of these degeneracies. For example, Knutson

et al. (2007b) use HST to observe transits of HD 209458b in 10 wavelength bands and measure the planetary radius with a relative accuracy (between bands) of $0.003R_J$, of the same level as the change in shape due to oblateness and the tidal bulge. Pont et al. (2007a) made a similar measurement for HD 189733b and reached even higher relative accuracy. Combining such measurements with other data (e.g., primary transits in the infrared, where limb-darkening is much smaller) and a stellar photosphere model (to correctly correlate limb darkening parameters as in Agol & Steffen 2007) could yield detections of planetary asphericity, especially in very hot Jupiters which have the largest bulges.

One possible source of confusion in interpreting planetary asphericity is the thermally-induced pressure effects of an unevenly radiated surface. In non-synchronous planets, the thermal tidal bulge (Arras & Socrates, 2009) can shift the level of the photosphere by approximately an atmospheric scale height, about 10^{-2} or 10^{-3} planetary radii (P. Arras, pers. comm.). The orientation of the thermal bulge is significantly different from the tidal or rotational bulges and should be distinguishable. Furthermore, very hot Jupiters should orbit synchronously, reducing the importance of this effect. Nevertheless, the effect of atmospheric phenomena on measurements of planetary asphericity should be considered.

Though difficult to disentangle from other small photometric effects, high-precision multi-color photometry may be another viable method for measuring k_{2p} . This technique is complimentary to detecting k_{2p} from apsidal precession since it does not require that the planet is eccentric, nor does it require a long time baseline. On some planets, the two methods could be used together as mutual confirmation of the planetary interior structure.

2.6 Conclusions

The planetary mass and radius are the only bulk physical characteristics measured for extra-solar planets to date. In this paper, we find that the planetary Love number (k_{2p} , equivalent to J_2) can also have an observationally detectable signal (quadrupole-induced apsidal precession) which can provide a new and unique probe into the interiors of very hot Jupiters. In particular, k_{2p} is influenced by the size of a solid core and other internal properties. Core sizes can be used to infer the formation and evolution of individual extra-solar planets (e.g., Dodson-Robinson & Bodenheimer, 2009; Helled & Schubert, 2009).

The presence of a nearby massive star creates a large tidal potential on these planets, raising significant tidal bulges which then induce non-Keplerian effects on the star-planet orbit itself. The resulting apsidal precession accounts for $\sim 95\%$ of the total apsidal precession in the best cases (Figure 2.1). Hence, we find that the internal density distribution, characterized by k_{2p} , has a large and clear signal, not to be confused with any other parameters or phenomena. We urge those

modeling the interior structures of extra-solar planets to tabulate the values of k_{2p} for their various models.

Encouraged by this result, we calculated full photometric light-curves like those expected from the *Kepler* mission to determine the realistic observability of the interior signal. We estimate that *Kepler* should be able to distinguish between interiors with and without massive cores ($\Delta k_{2p} \simeq 0.1$) for very hot Jupiters with eccentricities around $e \sim 0.003$ (Figure 2.6). Eccentricities this high may occur for some of the very hot Jupiters expected to be found by *Kepler*, though these planets usually have highly damped eccentricities. Much stronger constraints on apsidal precession can be obtained by combining *Kepler* photometry with precise secondary transits observed in the infrared. In cases where apsidal precession is not observed, the data can set strong upper limits on planetary eccentricities.

In analyzing *Kepler*'s photometric signal of apsidal precession, we find that transit timing variations are an almost negligible source of signal, though transit timing has been the focus of many observational and theoretical papers to date. The effect of "transit shaping" has ~ 30 times the photometric signal of transit timing for apsidal precession (see Figure 2.3, Pál & Kocsis, 2008; Jordan & Bakos, 2008)). At orientations where transit timing and shaping are weakest, the changing offset between primary and secondary transit times can be used to measure k_{2p} (Figure 2.4). It may also be possible to measure k_{2p} from high-precision multi-color photometry by directly detecting the planetary asphericity in transit. Such a measurement does not require a long baseline or an eccentric orbit.

Very hot Jupiters are also excellent candidates for detecting tidal semi-major axis decay, where we find that relatively small period changes of $\dot{P} \simeq 1$ ms/yr should be detectable. This could constitute the first measurements (or constraints) on tidal Q_* for a variety of individual stars. We note that *Kepler* measurements of transit timing and shaping for eclipsing binaries should also provide powerful constraints on stellar interiors through apsidal motion and binary orbital decay (due to tides, if the components are asynchronous).

Accurately measuring the interior structure of distant extra-solar planets seems too good to be true. Nevertheless, the exquisite precision, constant monitoring, and 3.5-year baseline of the *Kepler* mission combined with the high sensitivity of transit light curves to small changes in the star-planet orbit make this measurement plausible.

Our focus on *Kepler* data should not be interpreted to mean that other observations will be incapable of measuring k_{2p} . In fact, the opposite is true since the size of the apsidal precession signal increases dramatically with a longer baseline. Combining *Kepler* measurements with future ground and space based observations can create a powerful tool for measuring k_{2p} . In the far future, many planets will have measured apsidal precession rates (like eclipsing binary systems have now) and inferred k_{2p} values. Incorporating these measurements into interior models holds promise for

greater understanding of all extra-solar planets.

Acknowledgments: We thank Dave Stevenson, Mike Brown, Greg Laughlin, Oded Aharonson, Thomas Beatty, Phil Arras, Rosemary Mardling, Re'em Sari, Alejandro Soto, Ian McEwen and Chris Lee for help and useful discussions. We especially thank the referee, Dan Fabrycky, for helpful suggestions and discussions. DR is grateful for the support of the Moore Foundation. ASW is grateful for support from the National Science Foundation. This research has made use of NASA's Astrophysics Data System.

Bibliography

- Adams, F. C., & Laughlin, G. 2006, *Astrophysical Journal*, 649, 1004, arXiv:astro-ph/0606349
- Agol, E., Cowan, N. B., Bushong, J., Knutson, H., Charbonneau, D., Deming, D., & Steffen, J. H. 2009, in *IAU Symposium*, Vol. 253, *IAU Symposium*, 209–215
- Agol, E., Steffen, J., Sari, R., & Clarkson, W. 2005, *Monthly Notices of the RAS*, 359, 567, arXiv:astro-ph/0412032
- Agol, E., & Steffen, J. H. 2007, *Monthly Notices of the RAS*, 374, 941, arXiv:astro-ph/0610159
- Alonso, R., Aigrain, S., Pont, F., Mazeh, T., & The CoRoT Exoplanet Science Team. 2009, in *IAU Symposium*, Vol. 253, *IAU Symposium*, 91–96
- Arras, P., & Socrates, A. 2009, *ArXiv e-prints*, 0901.0735
- Bakos, G. Á. et al. 2009, *ArXiv e-prints*, 0901.0282
- Baraffe, I., Chabrier, G., & Barman, T. 2008, 0802.1810
- Barge, P. et al. 2008, 0803.3202
- Barker, A. J., & Ogilvie, G. I. 2009a, *ArXiv e-prints*, 0902.4554
- . 2009b, *ArXiv e-prints*, 0902.4563
- Barnes, J. W., & Fortney, J. J. 2003, *Astrophysical Journal*, 588, 545, arXiv:astro-ph/0301156
- Barnes, J. W., & O’Brien, D. P. 2002, *Astrophysical Journal*, 575, 1087, arXiv:astro-ph/0205035
- Batten, A. H. 1973, *Binary and multiple systems of stars (Binary and multiple systems of stars / by Alan H. Batten. Oxford ; New York : Pergamon Press, [1973] (International series of monographs in natural philosophy ; v. 51))*
- Bean, J. L. 2009, *ArXiv e-prints*, 0903.1845
- Beatty, T. G., & Gaudi, B. S. 2008, *ArXiv e-prints*, 804, 0804.1150
- Bodenheimer, P., Lin, D. N. C., & Mardling, R. A. 2001, *Astrophysical Journal*, 548, 466
- Borucki, W. J. et al. 2003, in *Presented at the Society of Photo-Optical Instrumentation Engineers (SPIE) Conference*, Vol. 4854, *Future EUV/UV and Visible Space Astrophysics Missions and Instrumentation*. Edited by J. Chris Blades, Oswald H. W. Siegmund. *Proceedings of the SPIE*, Volume 4854, pp. 129-140 (2003)., ed. J. C. Blades & O. H. W. Siegmund, 129–140
- Burrows, A., Hubeny, I., Budaj, J., & Hubbard, W. B. 2007, *Astrophysical Journal*, 661, 502, arXiv:astro-ph/0612703

- Burrows, A., Ibgui, L., & Hubeny, I. 2008, ArXiv e-prints, 803, 0803.2523
- Charbonneau, D. 2003, in *Astronomical Society of the Pacific Conference Series*, Vol. 294, *Scientific Frontiers in Research on Extrasolar Planets*, ed. D. Deming & S. Seager, 449–456
- Charbonneau, D. et al. 2005, *Astrophysical Journal*, 626, 523, arXiv:astro-ph/0503457
- Charbonneau, D., Brown, T. M., Latham, D. W., & Mayor, M. 2000, *Astrophysical Journal*, Letters, 529, L45, arXiv:astro-ph/9911436
- Chatterjee, S., Ford, E. B., & Rasio, F. A. 2007, ArXiv Astrophysics e-prints, astro-ph/0703166
- Christian, D. J. et al. 2008, ArXiv e-prints, 806, 0806.1482
- Christiansen, J. L. et al. 2009, in *IAU Symposium*, Vol. 253, *IAU Symposium*, 301–307
- Claret, A. 1995, *Astronomy and Astrophysics*, Supplement, 109, 441
- Cowling, T. G. 1938, *Monthly Notices of the RAS*, 98, 734
- Deeg, H. J., Ocaña, B., Kozhevnikov, V. P., Charbonneau, D., O’Donovan, F. T., & Doyle, L. R. 2008, *Astronomy and Astrophysics*, 480, 563, arXiv:0801.2186
- Dobbs-Dixon, I., Lin, D. N. C., & Mardling, R. A. 2004, *Astrophysical Journal*, 610, 464, arXiv:astro-ph/0408191
- Dodson-Robinson, S. E., & Bodenheimer, P. 2009, ArXiv e-prints, 0901.0582
- Eggleton, P. P., & Kiseleva-Eggleton, L. 2001, *Astrophysical Journal*, 562, 1012, arXiv:astro-ph/0104126
- Fabrycky, D. 2008a, *Astrophysical Journal*, Letters, 677, L117, 0803.1839
- Fabrycky, D., & Tremaine, S. 2007, *Astrophysical Journal*, 669, 1298, arXiv:0705.4285
- Fabrycky, D. C. 2008b, ArXiv e-prints, 806, 0806.4314
- Fabrycky, D. C., Johnson, E. T., & Goodman, J. 2007, *Astrophysical Journal*, 665, 754, arXiv:astro-ph/0703418
- Fabrycky, D. C., & Winn, J. N. 2009, ArXiv e-prints, 0902.0737
- Ferraz-Mello, S., Rodríguez, A., & Hussmann, H. 2008, 0712.1156
- Ford, E. B., & Holman, M. J. 2007, *Astrophysical Journal*, Letters, 664, L51, arXiv:0705.0356
- Ford, E. B., Lystad, V., & Rasio, F. A. 2005, *Nature*, 434, 873, arXiv:astro-ph/0502441
- Gillon, M., Anderson, D. R., Demory, B., Wilson, D. M., Hellier, C., Queloz, D., & Waelkens, C. 2008, ArXiv e-prints, 806, 0806.4911
- Goldreich, P., & Soter, S. 1966, *Icarus*, 5, 375
- Gomes, R., Levison, H. F., Tsiganis, K., & Morbidelli, A. 2005, *Nature*, 435, 466
- Goodman, J. 2009, ArXiv e-prints, 0901.3279
- Gu, P.-G., & Ogilvie, G. I. 2009, ArXiv e-prints, 0901.3401
- Guillot, T. 2005, *Annual Review of Earth and Planetary Sciences*, 33, 493, arXiv:astro-ph/0502068
- Guillot, T., Santos, N. C., Pont, F., Iro, N., Melo, C., & Ribas, I. 2006, *Astronomy and Astrophysics*, 453, L21, arXiv:astro-ph/0605751

- Hebb, L. et al. 2009, *Astrophysical Journal*, 693, 1920, 0812.3240
- Helled, R., & Schubert, G. 2009, ArXiv e-prints, 0903.1997
- Heyl, J. S., & Gladman, B. J. 2007, *Monthly Notices of the RAS*, 377, 1511, arXiv:astro-ph/0610267
- Holman, M. J., & Murray, N. W. 2005, *Science*, 307, 1288
- Holman, M. J. et al. 2007, *Astrophysical Journal*, 664, 1185, 0704.2907
- Hood, B., Wood, K., Seager, S., & Collier Cameron, A. 2008, ArXiv e-prints, 807, 0807.1561
- Hut, P. 1981, *Astronomy and Astrophysics*, 99, 126
- Iorio, L. 2006, *New Astronomy*, 11, 490, arXiv:gr-qc/0505107
- Jackson, B., Greenberg, R., & Barnes, R. 2008, 0801.0716
- Johns-Krull, C. M. et al. 2008, *Astrophysical Journal*, 677, 657, 0712.4283
- Jordan, A., & Bakos, G. A. 2008, ArXiv e-prints, 806, 0806.0630
- Joshi, Y. C. et al. 2009, *Monthly Notices of the RAS*, 392, 1532, 0806.1478
- . 2008, ArXiv e-prints, 806, 0806.1478
- Kallrath, J., Milone, E. F., Kallrath, J., & Milone, E. F., eds. 1999, *Eclipsing binary stars : modeling and analysis*
- Kjeldsen, H., Bedding, T. R., & Christensen-Dalsgaard, J. 2008, ArXiv e-prints, 807, 0807.0508
- Knutson, H. A. et al. 2007a, *Nature*, 447, 183, arXiv:0705.0993
- Knutson, H. A., Charbonneau, D., Noyes, R. W., Brown, T. M., & Gilliland, R. L. 2007b, *Astrophysical Journal*, 655, 564, arXiv:astro-ph/0603542
- Koch, D. et al. 2006, *Astrophysics and Space Science*, 304, 391
- Kopal, Z. 1959, *Close binary systems (The International Astrophysics Series, London: Chapman & Hall, 1959)*
- Kopal, Z., ed. 1978, *Astrophysics and Space Science Library, Vol. 68, Dynamics of Close Binary Systems*
- Kozai, Y. 1959, *Astronomical Journal*, 64, 367
- Lanza, A. F. et al. 2009, *Astronomy and Astrophysics*, 493, 193, 0811.0461
- Laughlin, G., Marcy, G. W., Vogt, S. S., Fischer, D. A., & Butler, R. P. 2005, *Astrophysical Journal, Letters*, 629, L121
- Lee, J. W., Kim, S.-L., Kim, C.-H., Koch, R. H., Lee, C.-U., Kim, H.-I., & Park, J.-H. 2009, *Astronomical Journal*, 137, 3181, 0811.3807
- Lévrard, B., Correia, A. C. M., Chabrier, G., Baraffe, I., Selsis, F., & Laskar, J. 2007, *Astronomy and Astrophysics*, 462, L5, arXiv:astro-ph/0612044
- Lévrard, B., Winisdoerffer, C., & Chabrier, G. 2009, *Astrophysical Journal, Letters*, 692, L9, 0901.2048
- Loeb, A. 2005, *Astrophysical Journal, Letters*, 623, L45, arXiv:astro-ph/0501548
- . 2008, ArXiv e-prints, 807, 0807.0835

- López-Morales, M., & Seager, S. 2007, *Astrophysical Journal, Letters*, 667, L191, arXiv:0708.0822
- Mandel, K., & Agol, E. 2002, *Astrophysical Journal, Letters*, 580, L171, arXiv:astro-ph/0210099
- Mardling, R. A. 2007, *Monthly Notices of the RAS*, 382, 1768, arXiv:0706.0224
- Mardling, R. A., & Lin, D. N. C. 2002, *Astrophysical Journal*, 573, 829
- Matsumura, S., Takeda, G., & Rasio, F. A. 2008, *Astrophysical Journal, Letters*, 686, L29, 0808.3724
- Mayor, M., Udry, S., Naef, D., Pepe, F., Queloz, D., Santos, N. C., & Burnet, M. 2004, *Astronomy and Astrophysics*, 415, 391, arXiv:astro-ph/0310316
- Miralda-Escudé, J. 2002, *Astrophysical Journal*, 564, 1019, arXiv:astro-ph/0104034
- Murray, C. D., & Dermott, S. F. 1999, *Solar system dynamics (Solar system dynamics by Murray, C. D., 1999)*
- Nesvorný, D., & Morbidelli, A. 2008, *Astrophysical Journal*, 688, 636
- O'Donovan, F. T., Charbonneau, D., Harrington, J., Seager, S., Deming, D., & Knutson, H. A. 2009, in *IAU Symposium, Vol. 253, IAU Symposium*, 536–539
- Pál, A., Bakos, G. Á., Noyes, R. W., & Torres, G. 2009, in *IAU Symposium, Vol. 253, IAU Symposium*, 428–431
- Pál, A., & Kocsis, B. 2008, *ArXiv e-prints*, 806, 0806.0629
- Peale, S. J., Cassen, P., & Reynolds, R. T. 1979, *Science*, 203, 892
- Pont, F. et al. 2007a, *Astronomy and Astrophysics*, 476, 1347, arXiv:0707.1940
- . 2007b, *Astronomy and Astrophysics*, 465, 1069, arXiv:astro-ph/0610827
- Rafikov, R. R. 2008, *ArXiv e-prints*, 807, 0807.0008
- Rodriguez, A., & Ferraz-Mello, S. 2009, *ArXiv e-prints*, 0903.0763
- Rowe, J. F. et al. 2007, *ArXiv e-prints*, 711, 0711.4111
- Russell, H. N. 1928, *Monthly Notices of the RAS*, 88, 641
- Sahu, K. C. et al. 2006, *Nature*, 443, 534, arXiv:astro-ph/0610098
- Sartoretti, P., & Schneider, J. 1999, *Astronomy and Astrophysics, Supplement*, 134, 553
- Sasselov, D. D. 2003, *Astrophysical Journal*, 596, 1327, arXiv:astro-ph/0303403
- Scharf, C. A. 2007, *Astrophysical Journal*, 661, 1218, arXiv:astro-ph/0702749
- Seager, S., & Hui, L. 2002, *Astrophysical Journal*, 574, 1004, arXiv:astro-ph/0204225
- Sing, D. K., & López-Morales, M. 2009, *Astronomy and Astrophysics*, 493, L31, 0901.1876
- Soffel, M. H. 1989, *Relativity in Astrometry, Celestial Mechanics and Geodesy (Relativity in Astrometry, Celestial Mechanics and Geodesy, XIV, 208 pp. 32 figs.. Springer-Verlag Berlin Heidelberg New York. Also Astronomy and Astrophysics Library)*
- Sotin, C., Gasset, O., & Mocquet, A. 2007, *Icarus*, 191, 337
- Southworth, J. 2008, 0802.3764
- Sozzetti, A. et al. 2009, *Astrophysical Journal*, 691, 1145, 0809.4589
- Sterne, T. E. 1939a, *Monthly Notices of the RAS*, 99, 451

- . 1939b, *Monthly Notices of the RAS*, 99, 662
- Swain, M. R., Vasisht, G., & Tinetti, G. 2008, *Nature*, 452, 329
- Thommes, E. W., Bryden, G., Wu, Y., & Rasio, F. A. 2008, *Astrophysical Journal*, 675, 1538, arXiv:0706.1235
- Torres, G., Winn, J. N., & Holman, M. J. 2008, 0801.1841
- Winn, J. N., & Holman, M. J. 2005, *Astrophysical Journal, Letters*, 628, L159, arXiv:astro-ph/0506468
- Winn, J. N. et al. 2007, *Astronomical Journal*, 134, 1707, arXiv:0707.1908
- Winn, J. N., Holman, M. J., Carter, J. A., Torres, G., Osip, D. J., & Beatty, T. 2009a, *Astronomical Journal*, 137, 3826, 0901.4346
- Winn, J. N., Holman, M. J., Shporer, A., Fernández, J., Mazeh, T., Latham, D. W., Charbonneau, D., & Everett, M. E. 2008, *Astronomical Journal*, 136, 267, arXiv:0804.2479
- Winn, J. N. et al. 2009b, *ArXiv e-prints*, 0902.3461
- . 2006, *Astrophysical Journal, Letters*, 653, L69, arXiv:astro-ph/0609506
- . 2005, *Astrophysical Journal*, 631, 1215, arXiv:astro-ph/0504555
- Wu, Y., & Goldreich, P. 2002, *Astrophysical Journal*, 564, 1024, arXiv:astro-ph/0108499
- Zharkov, V. N., & Trubitsyn, V. P. 1978, *Physics of planetary interiors (Astronomy and Astrophysics Series, Tucson: Pachart, 1978)*

Chapter 3

Candidates and Age of the Family of Kuiper Belt Object 2003 EL61

This chapter has been published in its entirety under the same title by authors D. Ragozzine and M. E. Brown in the *Astronomical Journal*, 2007, Volume 134, pp. 2160-2167. Reproduced by permission of the American Astronomical Society. Since publication, 2003 EL61 has been renamed Haumea.

Abstract

The collisional family of Kuiper belt object (KBO) 2003 EL61 opens the possibility for many interesting new studies of processes important in the formation and evolution of the outer solar system. As the first family in the Kuiper belt, it can be studied using techniques developed for studying asteroid families, although some modifications are necessary. Applying these modified techniques allows for a dynamical study of the 2003 EL61 family. The velocity required to change orbits is used to quantitatively identify objects near the collision. A method for identifying family members that have potentially diffused in resonances (like 2003 EL61) is also developed. Known family members are among the very closest KBOs to the collision and two new likely family members are identified: 2003 UZ117 and 1999 OY3. We also give tables of candidate family members which require future observations to confirm membership. We estimate that a minimum of ~ 1 GYr is needed for resonance diffusion to produce the current position of 2003 EL61, implying that the family is likely primordial. Future refinement of the age estimate is possible once (many) more resonant objects are identified. The ancient nature of the collision contrasts with the seemingly fresh surfaces of known family members, suggesting that our understanding of outer solar system surfaces is incomplete.

3.1 Introduction

The collisional history of Kuiper belt objects (KBO) strongly constrains the formation and evolution of the Kuiper belt. The recent discovery by Brown et al. (2007b, hereafter B07), of a KBO family created by a collision promises new and valuable information about the early outer solar system. As the first bona fide collisional family in the Kuiper belt, it merits further study and comparison to the Hirayama collisional families in the asteroid belt. The goal of this work is to identify potential fragments for future observations and study by properly adapting techniques used in dynamical studies of asteroid families. The distribution of family members is then be used to estimate the age of the family.

Members of the 2003 EL61 family are identified by infrared spectra with strong water ice absorptions (B07), as seen in large KBO (136108) 2003 EL61 and its brightest moon (Barkume et al., 2006; Trujillo et al., 2007). Based on light curve observations, 2003 EL61 appears to be rapidly rotating with an inferred density of at least 2.6 g cm^{-3} (Rabinowitz et al., 2006), suggesting that a giant impact stripped roughly 20% of the icy mantle from the proto-2003 EL61, based on an assumed initial density of about 2 g cm^{-3} as measured for other large KBOs (e.g., Pluto, Triton). The identification of the 2003 EL61 collisional family by B07 is presumably the discovery of icy mantle fragments ejected from this giant impact. The probability of such a giant impact in the current Kuiper belt is extremely low, implying that the collision probably occurred in the early history of the outer solar system before any significant depletion in mass, as we discuss below (Morbidelli et al., 2007).

3.2 Dynamics

3.2.1 Differences between KBO and Asteroid Families

The spread in orbital elements created by a collision in the Kuiper belt is different than the previously studied asteroid belt. In both cases, a collision powerful enough to create a family launches fragments at velocities high enough to be gravitationally ejected. The ejection velocity, Δv , is the velocity at infinity of unbound fragments and typically scales with the escape velocity from the surface of the target. Since known KBOs (especially 2003 EL61) are much larger than typical asteroids, the expected Δv of a family-forming collision is much larger in the Kuiper belt. In addition, the typical orbital velocities (v_{orb}) in the Kuiper belt are $\sim 5 \text{ km s}^{-1}$, compared to $\sim 20 \text{ km s}^{-1}$ typical of the asteroid belt. The ratio of $\Delta v/v_{orb}$ roughly determines the size of the spread in orbital elements that will be achieved by collisional dispersion. Hence, asteroid families will (initially) be far more tightly clustered in proper orbital element space than Kuiper belt families. Figure 1 shows the cloud of orbital elements created from a velocity dispersion of only 150 m s^{-1} from a potential origin of the 2003 EL61-forming collision (described in more detail below).

Asteroid families are often identified by looking only at clusters in proper orbital elements. This fails to identify true families in the Kuiper belt since the large anticipated spread in orbital elements is typically larger than the natural separation between objects (Chiang et al., 2003). The 2003 EL61 family was only identified because family members shared a unique spectral signature, in addition to being dynamically clustered. (B07)

Due to interactions with resonances, the dynamical clustering of collisional families grows weaker with time. In the asteroid belt, proper element dispersion is aided by drifting semi-major axes due to the Yarkovsky effect acting on small bodies (Farinella & Vokrouhlicky, 1999). In the Kuiper belt, objects are generally very stable over the age of the solar system except near mean-motion resonances with Neptune and/or when perihelia drop below about 35 AU (Kuchner et al., 2002).

3.2.2 Determining Δv

To identify dynamically-nearby KBOs for further investigation, we use Δv (the required ejection velocity) as a quantitative measurement of dynamical proximity. After a collision, each (unbound) fragment assumes a different heliocentric orbit, all of which intersect at the location of the collision (x_c, y_c, z_c) . At this location, each family member has a different velocity, \mathbf{v}_c . By definition, Δv is the length of $(\mathbf{v}_c - \mathbf{v}_{c,cm})$, where $\mathbf{v}_{c,cm}$ is the velocity at the collision location of the center of mass orbit; all values of Δv are measured with respect to the center of mass orbit. After the collision the center of mass orbit is nearly the orbit of the largest fragment; we approximate the center of mass orbit with the post-impact orbit of 2003 EL61. Finding Δv would be trivial if we knew the full set of orbital elements $(a, e, i, \Omega, \omega, M)$ for each object and 2003 EL61 at the time of the collision. Unfortunately, after a relatively short time, the coherence of the original orbital angles is lost and at the present epoch only the proper semi-major axes, proper eccentricities, and proper inclinations are known.

Even so, it is possible to use the distribution of proper elements of family members to estimate the orbital angles of the center of mass orbit (see below). Once these orbital elements are fully proscribed, there is enough information to calculate Δv using the additional constraint that all orbits pass through the collision location. For asteroid families, Gauss' equations are then used to compute the components of Δv (e.g., Morbidelli et al., 1995). These equations are only accurate if $\Delta v \ll v$ for each component of v , whereas for the 2003 EL61 family, which has a large velocity dispersion ($\gtrsim 200 \text{ m s}^{-1}$) and a relatively small orbital velocity ($\sim 4500 \text{ m s}^{-1}$), Gauss' equations can lead to inaccuracies which can be avoided through a more direct calculation.

Instead, we convert the center of mass orbital elements to Cartesian coordinates, giving the collision location (x_c, y_c, z_c) and velocity $\mathbf{v}_{c,cm}$. We then use a direct mathematical conversion of the KBO proper elements (a_P, e_P, i_P) and the collision location (x_c, y_c, z_c) to find the orbital velocity \mathbf{v}_c . However, these six variables do not uniquely determine the velocity; there are four

possible solutions to this inversion. (This degeneracy results from two different occurrences where either the positive or negative square root can be used.) That is, a single location (x_c, y_c, z_c) can be identified by identical orbital elements a_P , e_P , and i_P and four sets of velocities, as there is no way to distinguish between reflections along the line of apsides or the line of nodes. There is no *a priori* way to resolve this degeneracy since the information about the original orbital angles (Ω, ω, M) is lost. Since the goal of this study is to identify all KBOs that could potentially be members of the 2003 EL61 family, we take the smallest value of Δv . In this way, all KBOs with proper orbital elements that could be dynamically near the collision are identified.

To determine Δv of candidate family members requires the orbital elements of the center of mass orbit. This orbit is usually taken from the proper orbital elements of the largest fragment with orbital angles chosen to match the distribution of family members in a_P - e_P - i_P space (see Figures 1 and 2). The longitude of the ascending node (Ω_{cm}) has no effect on this distribution and is ignored. We use the orientation of the collisional cloud in a_P vs. e_P to find the mean anomaly (M_{cm}); the argument of perihelion (ω_{cm}) has no effect here. However, ω_{cm} does change the extent of the inclinations attainable with a particular value of Δv . In particular, for collisions that occur on the ecliptic ($\omega_{cm} + M_{cm} \simeq 0^\circ$ or 180°), require the lowest Δv to change the inclination. At the highest and lowest points of the orbit it is very difficult for a collision to change the inclination (apparent from the form of Gauss' equation for inclination changes, see Morbidelli et al. (1995)). There is not enough information in the distribution of proper elements of the family members to uniquely determine the component of Δv out of the plane of the orbit. In order to proceed, we choose to work with the minimum possible Δv , which we will call Δv_{min} . (The analysis in B07 did not appreciate this aspect of collisional orbit changes and assumed that Δv_{min} was the actual escape velocity of the fragments, which may not be true.) The component of Δv out of the plane of the orbit is larger by a factor of ~ 2 on average (i.e., with a randomly chosen ω_{cm}) and at extreme points in the orbit the actual ejection velocity could theoretically be ~ 5 or more times greater than Δv_{min} . However, collisions are most probable near the ecliptic (where the number density is highest), so the correction is probably much smaller. Furthermore, if an isotropic ejection of fragments is assumed, then this ambiguity is removed and the a_P - e_P - i_P distribution is sufficient to determine the typical ejection velocity (Nesvorný et al., 2006). The only way the actual ejection velocities of all the family members could have been significantly greater than $\sim 150 \text{ m s}^{-1}$ is if they all left in a collimated jet in a particular direction from a non-ecliptic collision. Finally, we note that a similar correction factor will apply to most KBOs, roughly preserving the overall ranking of KBOs by dynamical proximity to the collision.

3.3 Potential Family Members

3.3.1 Collision Center

For the 2003 EL61 family, we determined the center of mass orbit based on the orbit of 2003 EL61, the largest fragment. However, 2003 EL61 has diffused from its original location due to interaction in the 12:7 mean-motion resonance with Neptune (B07) and its proper elements have changed. Over long timescales, overlapping sub-resonances can cause diffusion of proper eccentricity and inclination (Nesvorný & Roig, 2001; Murray & Holman, 1997). For KBOs starting with orbital elements near the center of the 2003 EL61 family, we have found empirically that the chaotic diffusion nearly conserves the proper Tisserand parameter with respect to Neptune, the 50 MYr average of the osculating Tisserand parameter:

$$T = \frac{a_N}{a} + 2 \cos(i - i_N) \sqrt{(a/a_N)(1 - e^2)} \quad (3.1)$$

where a_N and i_N are the osculating semi-major axis and inclination of Neptune. In particular, we can estimate possible past locations of 2003 EL61 by changing the eccentricity and inclination to preserve the proper Tisserand parameter of 2003 EL61 ($a_p=43.10$ AU and $T_p=2.83$).

The pre-diffusion orbit of 2003 EL61 is estimated by minimizing the sum of Δv_{min} for previously identified family members (1995 SM55, 1996 TO66, 2002 TX300, 2003 OP32, and 2005 RR43) while fixing $a_P = a_{P,EL61}$ and $T_P = T_{P,EL61}$ and allowing the other orbital elements to vary. This results in a nominal collision location at $(a, e, i, \omega, M)_{cm} = (43.10 \text{ AU}, 0.118, 28.2^\circ, 270.8^\circ, 75.7^\circ)$ which is used to generate Figure 1 and the values of Δv_{min} for family members listed in Table 3.1. (As expected, the minimal velocities are attained for values of ω_{cm} that place the collision near the ecliptic.) The results that follow are not strongly dependent on this particular choice of the center of mass orbit. Exploring other center of mass orbits (such as the average of proper elements of non-resonant family members) indicates that the exact values of the ejection velocity vary somewhat, especially for objects near ($\Delta v \lesssim 100 \text{ m s}^{-1}$) the collision, but the known family members are always tightly clustered dynamically. Figure 1 shows the extent of proper element space covered by a collision with $\Delta v_{min}=150 \text{ m s}^{-1}$; this collisional cloud contains all the known family members (allowing for resonance diffusion).

3.3.2 Non-resonant KBOs

Keeping in mind the large spread in osculating elements of KBOs that could belong to the 2003 EL61 family, 131 high-inclination KBOs observed over at least two oppositions were chosen for further study. These objects were integrated using the n-body code SyMBA (Levison & Duncan, 1994) using the integrator `swift_rmvs3` based on the mapping by Wisdom & Holman (1991). The integration

proceeded backwards in time with 40-day timesteps from epoch JD 2451545.0 and included the 4 outer planets and the KBOs as test particles with initial conditions given by JPL HORIZONS¹. Proper elements were taken as the 50 MYr average of the corresponding osculating elements.

Using the center of mass orbit found above reveals that 2003 UZ117 and 2005 CB79 have small values of Δv_{min} , less than some known fragments. (No other KBOs have significantly smaller Δv_{min} than known family members.) KBO 2003 UZ117 has unpublished colors obtained by Tegler et al.² that show it has a clearly neutral color gradient. As shown in B07, all family members have blue/neutral visible color gradients (see Table 3.1 and references therein). Although future infrared observations are necessary, since this object has a strongly consistent color and is dynamically within the core of other known fragments, we will consider it a member of the 2003 EL61 family. No color or spectral information is available for 2005 CB79, but it has a very low Δv_{min} and is an excellent candidate family member.

We now seek a meaningful self-consistent value of Δv_{min} for other KBOs which may or may not be other family members. Allowing the center of mass orbital angles to vary can significantly change the shape of the collisional cloud and the values of Δv as illustrated in Figure 3.2. We could use the center of mass orbit found above (thin lines in Figure 3.2), but the small number of family members and their tight clustering does not provide a unique constraint for the orbital angles. On the other hand, the orbital angles that minimize Δv for each individual KBO may result in a collisional cloud that is inconsistent with the distribution of known family members (dotted line in Figure 3.2). As a compromise, we define Δv_{min} for candidate KBOs as the minimum Δv found by varying the orbital angles under the constraint that all known family members must lie within the resulting collisional cloud (thick solid curve in Figure 3.2). In other words, the angles are allowed to vary so long as the candidate KBO has larger Δv_{min} than all the known family members. This compromise allows for flexibility in estimating the center of mass orbital angles that are compatible with the known family members.

The results of this analysis are given in Table 3.1. For those KBOs known to be family members, accounting for errors in the orbital elements (as listed on the AstDys website³) caused variations in Δv_{min} of less than 5-10%.

¹<http://ssd.jpl.nasa.gov/horizons.cgi>

²<http://www.physics.nau.edu/~tegeler/research/survey.htm>

³<http://hamilton.dm.unipi.it/cgi-bin/astdys/astibo>

Table 3.1. KBOs Near the 2003 EL61 Family

Name	Δv_{min}	a_P (AU)	e_P	i_P ($^\circ$)	T_P	H^a	Visible Gradient ^b	Comments on Infrared Spectra	References
1996 TO66	24.2	43.32	0.12	28.02	2.83	4.50	2.38 ± 2.04	Strong Water Ice	3,5
2003 UZ117	66.8	44.26	0.13	27.88	2.84	5.20	0.00 ± 1.96	(Strong Water Ice)?	6
2005 CB79	96.7	43.27	0.13	27.17	2.84	5.0	NA		
2002 TX300	107.5	43.29	0.13	26.98	2.84	3.09	0.00 ± 0.67	Strong Water Ice	3
2005 RR43	111.2	43.27	0.13	27.07	2.84	4.00	NA	Strong Water Ice	3
2003 OP32	123.3	43.24	0.10	27.05	2.85	4.10	-1.09 ± 2.20	Strong Water Ice	3
2005 FY9	141.2	45.56	0.16	27.63	2.84	-0.23	NA	Methane Ice	1
2002 GH32	141.9	42.04	0.09	27.59	2.83	5.50	35.25 ± 10.21		4
1998 HL151	142.5	40.80	0.09	27.82	2.82	8.10	9.83 ± 21.2		4
2003 SQ317	148.0	42.67	0.09	28.16	2.83	6.30	NA		
1995 SM55	149.7	41.84	0.10	26.85	2.84	4.80	1.79 ± 2.60	Strong Water Ice	3,5
1999 OK4	161.5	43.30	0.15	28.58	2.81	7.60	NA		
2004 PT107	198.3	40.60	0.06	27.32	2.83	5.60	NA		
2005 UQ513	199.2	43.46	0.16	27.12	2.84	3.7	NA	Weak Water Ice	2
2003 HA57	214.3	39.44	0.15	28.40	2.78	8.10	NA		
2004 SB60	221.0	42.08	0.10	25.59	2.86	4.40	NA		
2003 TH58	229.6	39.44	0.06	29.50	2.78	7.60	NA		
1998 WT31	233.3	46.04	0.19	27.91	2.83	7.05	5.57 ± 5.61		4
2002 AW197	265.0	47.28	0.12	26.00	2.90	3.27	22.45 ± 1.62	No Water Ice	3
1996 RQ20	269.9	43.89	0.10	31.74	2.76	6.95	19.81 ± 6.31	IR Colors Inconsistent	4,5
1999 OY3	292.8	43.92	0.17	25.80	2.86	6.76	-2.62 ± 3.39	Vis and IR Colors of Strong Water Ice	4,5
1999 OH4	305.1	40.52	0.04	26.71	2.84	8.30	NA	IR Colors Inconsistent	5
1997 RX9	306.1	41.62	0.05	29.31	2.80	8.30	NA		
2001 QC298	310.2	46.32	0.13	31.59	2.78	6.09	NA	IR Colors Inconsistent	5
2003 EL61 ^c	323.5	43.10	0.19	26.85	2.83	0.27	-0.18 ± 0.67	Strong Water Ice	3
2000 CG105	330.6	46.38	0.04	29.43	2.84	6.50	2.58 ± 17.72	IR Colors Inconsistent	4,5
2003 HX56	363.2	47.32	0.21	30.00	2.79	7.10	NA		
1999 CD158	364.0	43.71	0.15	23.83	2.90	5.05	16.36 ± 3.41	IR Colors Inconsistent	4,5

References. — (1) Brown et al. (2007a) (2) Barkume et al. in press (3) Brown et al. (2007) (4) MBOSS Database <http://www.sc.eso.org/~chainaut/MBOSS/> and references therein (5) Noll et al. (2005) (6) Tegler et al. website <http://www.physics.nau.edu/teglert/research/survey.htm>

Note. — As explained in the text, Δv_{min} is the minimum ejection velocity required to reach the orbit of the listed KBO from the modeled 2003 EL61 family-forming collision in m s^{-1} . The actual ejection velocities could be different, but the relative order should be roughly correct. Known family members have visible color gradients near zero and strong water ice spectra. Other objects listed could be family members or interlopers.

^aAbsolute Magnitude

^bAs defined in References 1 and 4. Objects without published colors list "NA".

^cThis refers to the current proper elements, without allowing diffusion.

The blue/neutral visible color gradients of 1998 HL151 and 1998 WT31 are similar to known family members (see Tables 3.1 and 3.2 and references therein). Blue colors are suggestive, but do not necessarily imply the strong water ice spectrum that characterizes this family (B07). Without observational evidence of a water-ice spectrum, we cannot confirm whether these objects are 2003 EL61 family members or merely interlopers, which appears to be the case for 2002 GH32 and others which have red visible color gradients. Table(s) 3.1 (and 3.2) then serves as a guide for future observations.

3.3.3 Resonant KBOs

As a consequence of the wide dispersion of fragments from a collision in the Kuiper belt, many objects can be injected into various mean-motion resonances with Neptune. While KBOs in low-order resonances (e.g., 3:2) can be stable for the age of the solar system, objects in high-order resonances (found throughout the region of the 2003 EL61 family) will experience chaotic diffusion, as discussed above. Over timescales of tens of millions to billions of years, the proper eccentricity and inclination of resonant KBOs are not conserved. These objects can not be directly connected to the family based on current proper elements because their proper elements have changed since the formation of the family. How then can we identify such fragments? In the case of 2003 EL61, it is the consistent strong water ice spectrum, as well as several indications of a past giant impact, that connect it to the non-resonant objects. Similarly, in the asteroid belt, the Eos family intersects the 4:9 Jovian resonance and objects in the resonance have diffused in eccentricity and inclination (Morbidelli et al., 1995). Spectroscopic studies of a few asteroids in the resonance showed them to be uniquely identifiable and consistent with the rest of the Eos family, confirming that these fugitives are collisionally linked (Zappalà et al., 2000).

For resonant KBOs that have not yet diffused to scattered or low-perihelion orbits, the Tisserand parameter with respect to Neptune, T , can be used as a reasonable dynamical criterion for family membership. Through forward modeling, we have verified that the velocity dispersion ($\Delta v \lesssim 300 \text{ m s}^{-1}$) due to the collision and the forced variation of osculating elements in time together cause maximal variations in T of about ~ 0.1 from ~ 2.85 . Only about 16% of multi-opposition KBOs have a Tisserand parameter between 2.74 and 2.96, and these were included in our integrations of KBOs.

To identify candidate fragments that could have diffused in resonances, we allowed the proper eccentricity and inclination of each KBO to vary, conserving the proper Tisserand parameter, while the semi-major axis of the KBO was fixed to a_P . The minimal velocity distance, found using the method described above, is called δv_{min} to distinguish it from the velocity computed with the current proper elements and is listed in Table 3.2. Of course, this value of δv_{min} will always be less than the corresponding Δv_{min} computed with unadjustable proper elements and will increase the

number of interlopers. Even so, it can give an indication of objects that had low ejection velocities and subsequently diffused in a resonance. Table 3.2 lists the resonances present in our integration of these objects. Even for multi-opposition KBOs, current membership in any of the many weak resonances in this region can be easily obscured within the errors in the determination of orbital elements. To be conservative, we calculate δv_{min} for all KBOs in our integration. A lack of resonance identification in Table 3.2 is not meant to imply that these objects have not actually been affected by proper element diffusion.

Table 3.2. Diffused KBOs Near the 2003 EL61 Family

Name	δv_{min}	a_P (AU)	e_{min}	i_{min} ($^{\circ}$)	T_P	H^a	Visible Gradient ^b	Comments on Infrared Spectra	Resonance	References
1996 TO66	15.0	43.32	0.11	28.09	2.83	4.50	2.38 ± 2.04	Strong Water Ice	19:11	3,5
2003 SQ317	31.4	42.67	0.11	27.92	2.83	6.30	NA			
2005 UQ513	39.0	43.27	0.12	27.77	2.84	5.0	NA	Weak Water Ice		2
2005 RR43	58.0	43.27	0.11	27.38	2.84	4.00	NA	Strong Water Ice		3
2003 UZ117	60.8	44.26	0.12	28.01	2.84	5.20	0.00 ± 1.96	(Strong Water Ice)?		6
2005 CB79	66.5	43.27	0.11	27.40	2.84	5.0	NA			
2002 TX300	68.4	43.29	0.11	27.23	2.84	3.09	0.00 ± 0.67	Strong Water Ice		3
1999 OK4	72.5	43.30	0.12	29.16	2.81	7.60	NA			
2002 GH32	79.3	42.04	0.10	27.50	2.83	5.50	35.25 ± 10.21			4
1997 RX9	86.8	41.62	0.13	28.46	2.80	8.30	NA			
2003 OP32	91.4	43.24	0.11	26.90	2.85	4.10	-1.09 ± 2.20	Strong Water Ice		3
1999 OY3	96.6	43.92	0.10	27.00	2.86	6.76	-2.62 ± 3.39	IR Colors of Strong Water Ice	^c	4,5
2005 FY9	118.0	45.56	0.15	27.87	2.84	-0.23	NA	Methane Ice		1
1995 SM55	123.3	41.84	0.09	26.98	2.84	4.80	1.79 ± 2.60	Strong Water Ice		3,5
1998 HL151	136.4	40.80	0.11	27.55	2.82	8.10	9.83 ± 21.2			4
1998 WT31	139.8	46.04	0.16	28.57	2.83	7.05	5.57 ± 5.61			4
2000 CG105	149.0	46.38	0.16	28.04	2.84	6.50	2.58 ± 17.72	IR Colors Inconsistent		4,5
2004 PT107	161.9	40.60	0.09	27.08	2.83	5.60	NA			
1999 RY215	183.0	45.28	0.11	26.37	2.88	6.13	4.54 ± 6.65	IR Colors Inconsistent		4,5
2001 FU172	200.0	39.44	0.08	28.62	2.80	8.30	NA		3:2	
1999 OH4	200.5	40.52	0.08	26.45	2.84	8.30	NA	IR Colors Inconsistent		5
2003 HA57	212.3	39.44	0.12	28.80	2.78	8.10	NA		3:2	
2003 TH58	214.7	39.44	0.13	28.82	2.78	7.60	NA		3:2	
2004 SB60	218.5	42.08	0.10	25.63	2.86	4.40	NA			
2003 QX91	222.0	43.71	0.12	31.03	2.77	8.30	NA		7:4	
2000 JG81	235.1	47.77	0.12	27.42	2.88	9.10	NA		2:1	
1999 KR16	242.9	49.00	0.22	28.34	2.84	5.70	44.74 ± 3.21	IR Colors Inconsistent		4
2005 GE187	243.5	39.44	0.07	26.50	2.84	7.10	NA		3:2	
1996 TR66	248.3	47.78	0.11	26.94	2.89	7.50	NA	IR Colors Inconsistent		5

References. — (1) Brown et al. (2007a) (2) Barkume et al. in press (3) Brown et al. (2007) (4) MBOSS Database <http://www.sc.eso.org/ohainaut/MBOSS/> and references therein (5) Noll et al. (2005) (6) Tegler et al. website <http://www.physics.nau.edu/~teglert/research/survey.htm>

Note. — As explained in the text, δv_{min} is the minimum ejection velocity required to reach an orbit with the same proper semi-major axis (a_P) and proper Tisserand parameter (T_P) of the listed KBOs in m s^{-1} . Integrations indicate T_P is nearly conserved during eccentricity and inclination diffusion in mean-motion resonances. By construction, 2003 EL61 is the center of the collision (allowing diffusion). For those objects which are resonant in our integration (identified by libration of the resonance angle in the past 4 MYr), the resonance type is listed. Many more objects may be in resonance within the errors of orbit determination (e.g., 1999 OY3), which were not accounted for here.

^aAbsolute Magnitude

^bAs defined in References 1 and 4. Objects without published colors list "NA".

^c1999 OY3 is probably affected by the 7:4 resonance.

As with non-resonant objects, good spectroscopic evidence is required to consider these objects part of the 2003 EL61 family. KBO 1999 OY3 has reported near-infrared colors consistent with other family members, which have unique colors due to the presence of strong water ice absorptions (Noll et al., 2005). Integrations of clones of this KBO that include errors in orbital elements show that there is a high probability that it is in the 7:4 mean motion resonance. It also has a very low resonant δv_{min} and, like 2003 EL61 and 1996 TO66, appears to be a family member in a resonance. 2005 UQ513 has a very low δv_{min} , but does not have the characteristic spectral features of the family members.

3.4 Age of the Family

Determining the age of the 2003 EL61 family will allow new insights into the history of the Kuiper belt. It is possible to constrain the age because the shape of a collisional cloud will evolve in time by resonance diffusion (Milani & Farinella, 1994). In each resonance, the changing eccentricity distribution of KBOs can be computed by numerical integrations. (Throughout this section, all orbital elements refer to proper orbital elements.) As resonance diffusion is chaotic, ages cannot be calculated by back-integration of known particles. Instead, an ensemble of particles (with an assumed initial distribution of eccentricities) is integrated forward for the age of the solar system. Comparing the eccentricities of remaining particles to the eccentricities of known family members results in an age estimate.

3.4.1 Diffusion Time of 2003 EL61

One estimate of the age of the family is the time needed for 2003 EL61 to diffuse from its original eccentricity to the current value. Matching the distribution of known family members above has yielded an estimate of the initial eccentricity and inclination of 2003 EL61 before diffusion, assuming that its displacement from the center of the family is small (which is expected from conservation of momentum). From an ensemble of randomly placed test particles, 78 particles in the 12:7 resonance with low values of Δv from the collision center (near $e_{P,orig} = .118$) were chosen for long-term integration. Again using SyMBA with a 40-day timestep, these particles were integrated for the age of the solar system. The initial configurations of the planets were also randomly chosen (by randomly choosing the starting epoch in the past 100 MYr). As expected from the chaotic nature of resonance diffusion, the results do not significantly depend on the orientation of the planets or even the initial location of 2003 EL61. Initial eccentricities ranged from 0.09 to 0.14, but other than a slight preference for higher eccentricity particles to escape sooner, the calculated diffusion times were similar.

The current proper perihelion of 2003 EL61 is 35 AU, the approximate limit for stability against

close encounters with Neptune. In our simulations, particles are usually removed shortly after attaining the current eccentricity of EL61 $e_{P,now} = 0.186$, though they occasionally diffuse back down to lower eccentricities. In Figure 3.3, we have plotted the fraction of particles with proper eccentricities below $e_{P,now}$ as a function of time. Nearly 90% of the particles have not diffused the full distance a billion years into the integrations. After 3.5 billion years of evolution, roughly half of the particles have reached the current eccentricity of 2003 EL61. We conclude that with 90% confidence, the 2003 EL61 family is older than 1 GYr, with an age estimate of 3.5 ± 2 GYr (1-sigma). Importantly, the age is completely consistent with formation at the beginning of the solar system: the family is ancient and likely primordial.

3.4.2 Diffusion Time of Other Resonant Family Members

As the progenitor of the collision, the resonance diffusion of 2003 EL61 is a special case because it is a unique object. For other family members, a similar analysis would require assumptions about the number of similar objects captured in each resonance. To avoid unnecessary assumptions, we propose a simple method for estimating the age of the family by using the eccentricity distribution of family members currently in the resonance instead of focusing on any single particle. The initial eccentricity distribution in a resonance can be inferred from the eccentricity distribution of nearby non-resonant particles whose (proper) eccentricities are essentially constant for the age of the solar system. Integrating an ensemble of particles with the same starting eccentricities will produce an evolving eccentricity distribution. As an example, consider the eccentricity evolution for the 12:7 resonants shown in Figure 3.4; only the eccentricities of objects still in the resonance are shown. After debiasing the eccentricity distribution of known family members for detection biases, the current eccentricity distribution can be statistically compared with the integrations. As it uses only the distribution of remaining eccentricities, this method does not require any assumptions about the efficiency of initial emplacement in or removal from the resonance in question.

The characteristic diffusion timescale of these resonances strongly depends on the order or strength of the resonance. While 2003 EL61 is in the fifth-order 12:7 resonance, 1996 TO66 appears to be in the weaker eighth-order 19:11 resonance. Over the age of the solar system, the proper eccentricities of 19:11 resonants (near the current location of TO66) only change by 0.01-0.02; this is less than the accuracy with which one could infer the unknown initial location of these objects. The eccentricity distribution of objects in such weak resonances are essentially constant in time and therefore cannot provide a meaningful age constraint.

In contrast, 1999 OY3 is in the strong third-order 7:4 resonance. In addition to increased diffusion times, 7:4 resonants often participate in the Kozai resonance which allows for exchange of angular momentum between eccentricity and inclination (Lykawka & Mukai, 2005). Particles near the assumed starting position of OY3 unpredictably enter and leave the Kozai resonance, potentially

causing huge swings in eccentricity (as these are all high inclination particles) on very short (MYr) timescales. Practically any current eccentricity could have possibly been generated by the Kozai resonance in less than 10 MYr. Therefore, this resonance also appears to be a fruitless source of useful age constraints from eccentricity diffusion. It is important to note here that the assumption of constant T_P is often violated by these particles; the Kozai resonance carries them to low perihelia where they interact with Neptune (which is itself interacting with the other giant planets) often causing a change in T_P . Therefore, KBOs with low perihelia in the past or present are susceptible to inaccurate estimations of the initial ejection velocity (δv_{min}). Although these particles can be significantly perturbed, in an integration of 20 particles in the 7:4 resonance starting near the estimated initial conditions of OY3, half are still in the resonance after 4.5 GYr.

3.4.3 Future Age Estimates

In the future, more family members will be identified in resonances that will, like the 12:7 resonance, have diffusion timescales that are neither too slow nor too fast. The addition of several new family members will allow for further refinement of these age estimates.

It is possible to evaluate the number of resonant particles needed to make a significant improvement upon our age estimate of 3.5 ± 2 GYr. From the distributions of remaining 12:7 resonants shown in Figure 3.4, we randomly drew 5, 10, 50, and 100 eccentricities with replacement at half-billion year intervals from particles that were still in the resonance. Every pair of distributions was inter-compared using the Kuiper variant of the K-S test which returns a significance near 1 if the distributions are distinguishable statistically. This process (of random selection and cross-comparison) was repeated 100 times and the results averaged. Figure 3.5 shows some of the results of this analysis. For example, if the actual age of the family is 3.5 GYr (Figure 3.5, upper right) then with ~ 50 particles (triangles), an age of 2.5 GYr or younger can be ruled out since these eccentricity distributions are different with greater than 90% significance. With ~ 100 resonant particles, the accuracy in the age determination can generally be brought down to 0.5 GYr.

Unfortunately, the chaotic nature of eccentricity diffusion makes it difficult to determine a precise age without a large number of objects. However, it should be noted that each resonance gives an essentially independent measure of the age so that a total of 50-100 known family members in the appropriate (e.g., not too fast or too slow) resonances should be sufficient to get a relatively precise age estimate. In the near future, as the high-inclination region of the Kuiper belt is probed much more deeply, many new family members should be readily discovered.

3.5 Discussion

Identifying more 2003 EL61 family members is very useful for learning more about this family and its relationship to the formation and evolution of the outer solar system. Based on dynamical and observational evidence, we add 2003 UZ117 and 1999 OY3 to the list of 2003 EL61 family members, although the former should be observed in the infrared for confirmation of a strong water ice signature.

Due to the highly dispersive nature of large Kuiper belt collisions, some simplifications were made to identify potential family members. The computed values of Δv_{min} (Table 3.1) and especially δv_{min} (Table 3.2) could be significantly different from the true ejection velocities. Even so, we find it highly significant that all of the known fragments of the 2003 EL61 family can be explained by a velocity dispersion of 150 m s^{-1} from a single collision location, and allowing the objects in resonances to diffuse in eccentricity. In addition, all known KBOs near the proposed collision have strong water ice signatures, including the strongest such absorption features known in the Kuiper belt (except possibly 2003 UZ117, whose spectrum is unknown) (B07). Combining dynamical and spectroscopic evidence, the 2003 EL61 family currently includes, in order of decreasing absolute magnitude: (136108) 2003 EL61, (55636) 2002 TX300, (145453) 2005 RR43, (120178) 2003 OP32, (19308) 1996 TO66, (24835) 1995 SM55, 2003 UZ117, and (86047) 1999 OY3.

Many potential family members have no known photometric or spectroscopic observations. Observations of near-infrared colors on these objects will help to distinguish family members from interlopers. Discovery of additional family members will do much to improve our understanding of this family and the outer solar system. In particular, fragments in resonances have the unique ability to constrain the age of the collisional family as eccentricity diffusion, though chaotic, is time dependent. Based on the time needed for 2003 EL61 to diffuse to its current location, the family-forming collision occurred at least a billion years ago. Indeed, the probability of such a collision is only reasonable in the primordial Kuiper belt when the number densities of large KBOs was much higher. However, the collision should have occurred after any significant dynamical stirring as the orbital distribution of the family remains tight and seemingly unperturbed.

There appears to be no dynamical evidence that is not consistent with the formation of the 2003 EL61 family by an ancient collision. It is therefore interesting that all family members appear to be bright and pristine with strong crystalline water ice spectra. (B07) These surfaces seem to be exceptions to the premise that all static surfaces in the outer solar system darken and redden in time (e.g., Luu & Jewitt, 1996). This is not due to their location in the outer solar system, as there are KBOs dynamically nearby with red spectrally-featureless surfaces (see Tables 3.1 and 3.2). Perhaps the collision was energetic enough to sublimate and lose volatiles before they were able to transform into the higher-order hydrocarbons that are thought to be the darkening reddening agent

dominant in the outer solar system. However, this does not really distinguish these family members from all KBOs, at least some of which should have experienced similarly energetic impacts. Instead, the distinguishing characteristic may be that the relatively large proto-2003 EL61 was able to fully differentiate and the resulting fragments were compositionally much purer than other objects, even fragments from non-differentiated progenitors. In any case, the unique spectra of family members promise to improve our understanding of outer solar system surface processes (Barkume et al. 2007, in press).

Understanding the surfaces of KBOs is one of many insights provided by the likely primordial nature of the 2003 EL61 family. Another is the apparent need for higher number densities in the past if the family-forming collision is to be rendered probable. Continuing identification and characterization of family members can uniquely improve our understanding of this collision and its connection to the formation and evolution of the outer solar system.

Acknowledgments: We would like to thank Kris Barkume, Alessandro Morbidelli, Keith Noll, Emily Schaller, Meg Schwamb, and Jack Wisdom for valuable discussions. We would like to thank the referee (David Nesvorný) for timely reviews that improved the quality of this paper. DR is grateful for the support of the Moore Foundation.

Bibliography

- Barkume, K. M., Brown, M. E., & Schaller, E. L. 2006, *Astrophysical Journal, Letters*, 640, L87.
[astro-ph/0601534](#)
- Brown, M. E., Barkume, K. M., Blake, G. A., Schaller, E. L., Rabinowitz, D. L., Roe, H. G., & Trujillo, C. A. 2007a, *Astronomical Journal*, 133, 284
- Brown, M. E., Barkume, K. M., Ragozzine, D., & Schaller, E. L. 2007b, *Nature*, 446, 294
- Chiang, E. I., Loring, J. R., Millis, R. L., Buie, M. W., Wasserman, L. H., & Meech, K. J. 2003, *Earth Moon and Planets*, 92, 49
- Farinella, P., & Vokrouhlicky, D. 1999, *Science*, 283, 1507
- Kuchner, M. J., Brown, M. E., & Holman, M. 2002, *Astronomical Journal*, 124, 1221.
[astro-ph/0206260](#)
- Levison, H. F., & Duncan, M. J. 1994, *Icarus*, 108, 18
- Luu, J., & Jewitt, D. 1996, *Astronomical Journal*, 112, 2310
- Lykawka, P. S., & Mukai, T. 2005, *Planetary Space Science*, 53, 1175
- Milani, A., & Farinella, P. 1994, *Nature*, 370, 40
- Morbidelli, A., Levison, H. F., & Gomes, R. 2007, *ArXiv Astrophysics e-prints*. [astro-ph/0703558](#)
- Morbidelli, A., Zappala, V., Moons, M., Cellino, A., & Gonczi, R. 1995, *Icarus*, 118, 132
- Murray, N., & Holman, M. 1997, *Astronomical Journal*, 114, 1246
- Nesvorný, D., Enke, B. L., Bottke, W. F., Durda, D. D., Asphaug, E., & Richardson, D. C. 2006, *Icarus*, 183, 296
- Nesvorný, D., & Roig, F. 2001, *Icarus*, 150, 104
- Noll, K., Stephens, D., Grundy, W., Cruikshank, D., Romanishin, W., & Tegler, S. 2005, in *Bulletin of the American Astronomical Society*, 746
- Rabinowitz, D. L., Barkume, K., Brown, M. E., Roe, H., Schwartz, M., Tourtellotte, S., & Trujillo, C. 2006, *Astrophysical Journal*, 639, 1238. [astro-ph/0509401](#)
- Trujillo, C. A., Brown, M. E., Barkume, K. M., Schaller, E. L., & Rabinowitz, D. L. 2007, *Astrophysical Journal*, 655, 1172. [astro-ph/0601618](#)
- Wisdom, J., & Holman, M. 1991, *Astronomical Journal*, 102, 1528
- Zappalà, V., Bendjoya, P., Cellino, A., Di Martino, M., Doressoundiram, A., Manara, A., & Miglior-

ini, F. 2000, *Icarus*, 145, 4

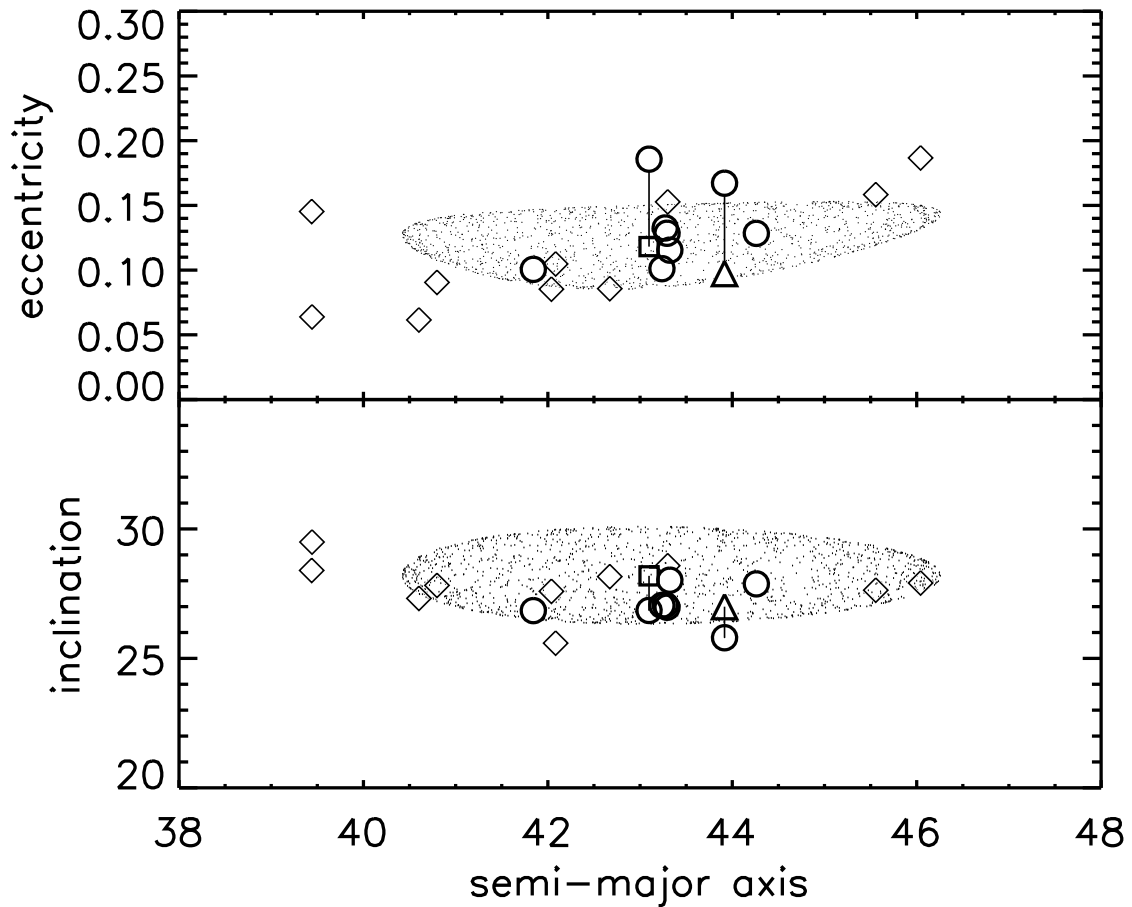


Figure 3.1 Current proper orbital elements of members of the 2003 EL61 family (circles) and potential family members (diamonds). The cloud of small points illustrate the dispersion in semi-major axis, eccentricity, and inclination of objects ejected from the nominal collision location (located at the center of the square) with an isotropic Δv of 150 m s^{-1} , enough to explain all the currently known members of the 2003 EL61 family. (Note that the orbital angles are chosen to minimize Δv ; the actual ejection velocities may be larger.) The square identifies the calculated location of the collision center which is assumed to be the initial location of 2003 EL61 before resonance diffusion (marked by vertical lines). The two rightmost circles are the current proper elements of 1999 OY3 and 2003 UZ117, new family members identified in this work. KBO 1999 OY3 (which has visible and infrared colors consistent with family members) is also allowed to diffuse to the location marked by the triangle (see Table 3.2). The proper elements of other KBOs with $\Delta v < 250 \text{ m s}^{-1}$ (listed in Table 3.1) are shown as diamonds.

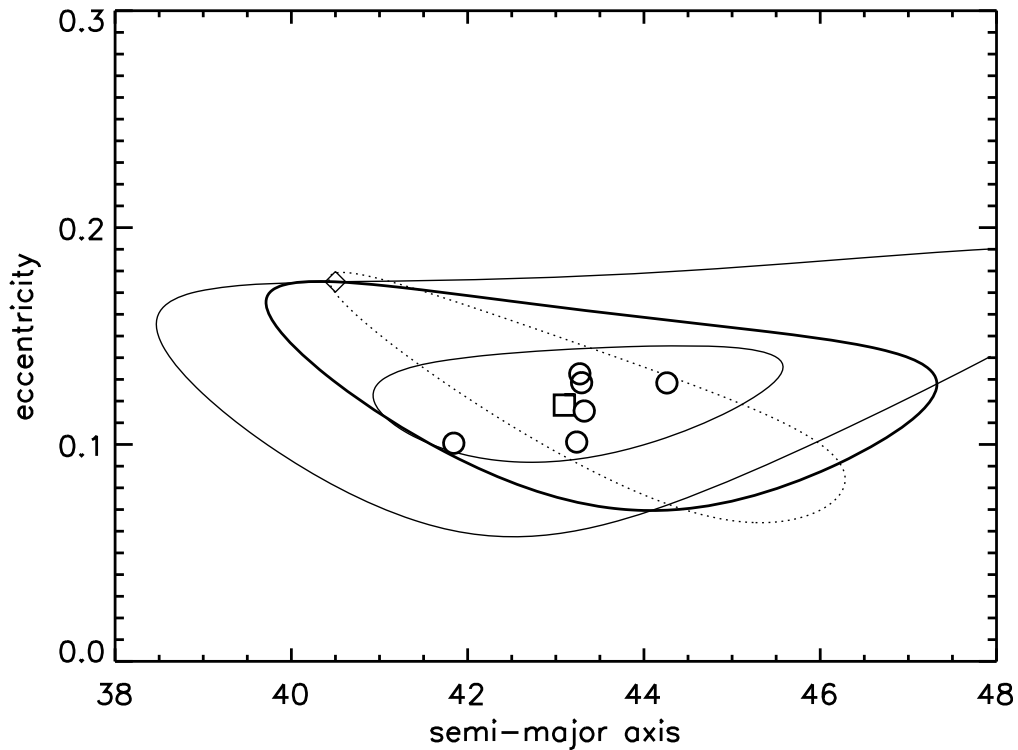


Figure 3.2 Illustration of determining Δv for candidate family members. The known (non-diffusing) family members (circles) fall into a relatively small region of proper orbital element space. (In this illustration, inclinations are held constant and collisions are located near the ecliptic.) These can be explained by ejection from the center of mass orbit (square) with Δv of 150 m s^{-1} or less, marked by the smallest thin solid curve. A hypothetical KBO (diamond) can be explained with larger Δv from the same center of mass orbit, shown by the larger thin curve. Alternatively, by changing the orbital angles, particularly the mean anomaly, the shape of the collisional cloud can also change requiring a much smaller Δv (dotted curve). However, the resulting angle may be inconsistent with the distribution of known family members, as in the case above. As a compromise between these two methods, we find the Δv_{min} for KBOs by allowing the center of mass orbital angles to vary with the constraint that all known family members must lie within the collisional cloud (thick solid curve).

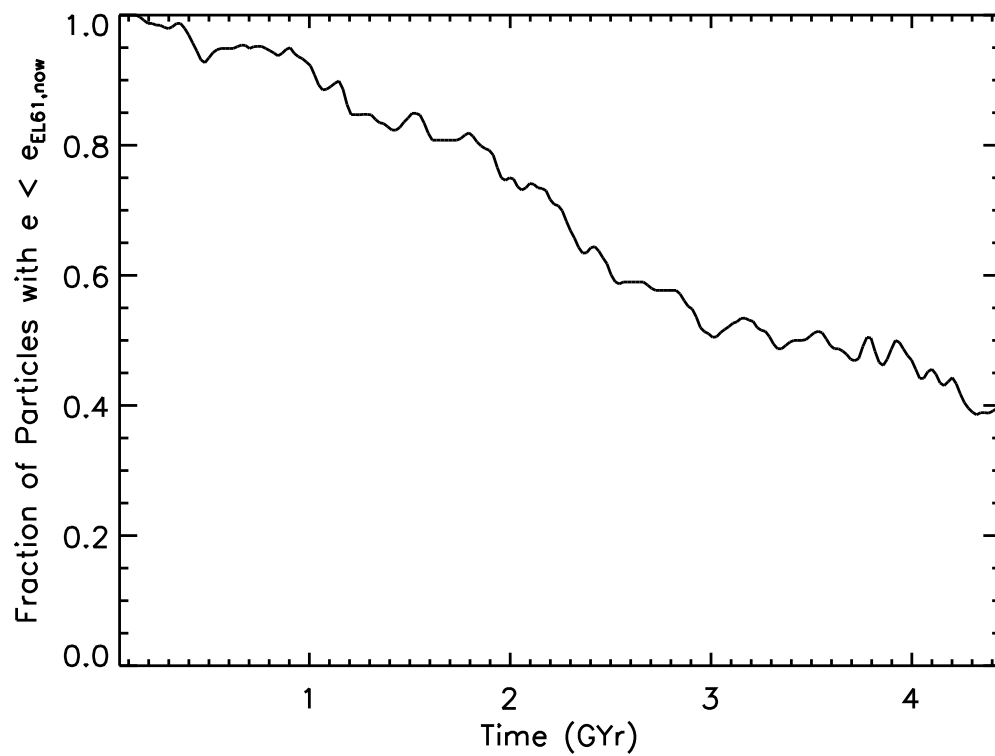


Figure 3.3 Fraction of particles that have eccentricities less than the current eccentricity of 2003 EL61 ($e_P < 0.186$). Calculated from an integration of 78 12:7 resonants with initial eccentricities near 0.118 (the expected initial eccentricity of 2003 EL61). The current location of 2003 EL61 is attained by 10% of resonant KBOs in less than ~ 1 GYr. After nearly 4 GYr of evolution, half the particles have passed the current location of 2003 EL61. We conclude that the 2003 EL61 family is ancient and probably primordial.

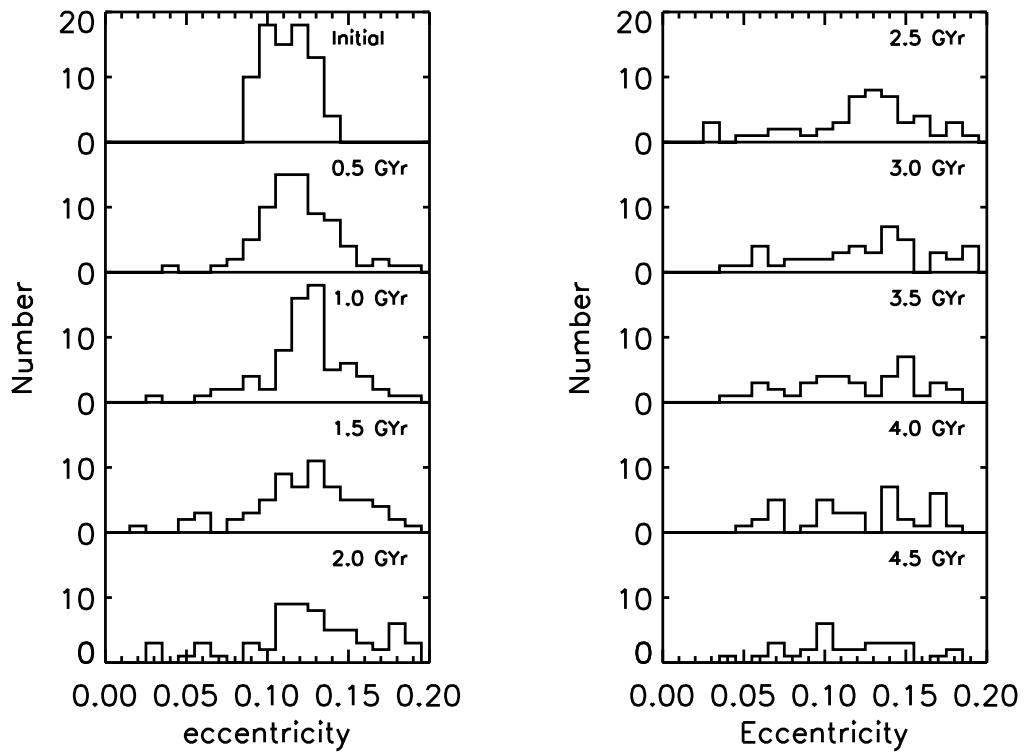


Figure 3.4 Distribution of eccentricities of 12:7 resonants at half-billion year intervals. Only particles remaining in the resonance are shown. The bin size is 0.01 in eccentricity. A clear diffusion-like spreading is evident in the widening of the initial peak. The eccentricities of KBOs in this resonance will have a distribution that can be compared to these distributions in order to estimate an age.

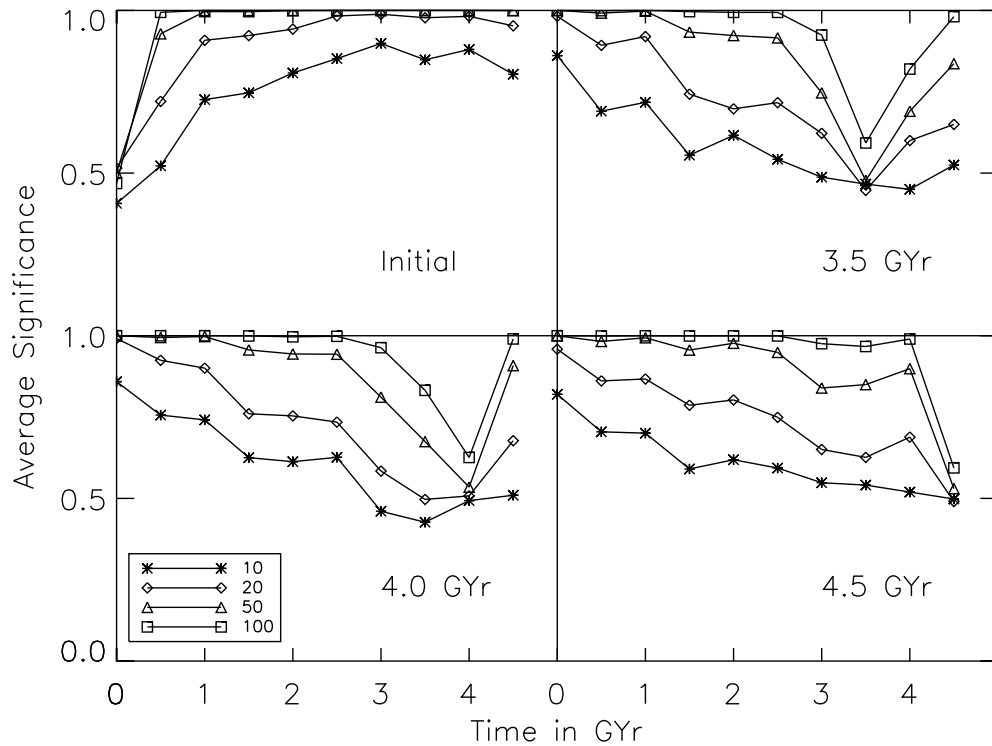


Figure 3.5 Correlations of eccentricity distributions with each other. As explained in the text, a random sample of particles is chosen from two ages and compared using the Kuiper variant of the K-S test. The probability that the two distributions are different is represented by the significance. The cross-comparisons with all ages are shown for the initial distribution (upper left) and the distributions at 3.5 GYr (upper right), 4.0 GYr (lower left), and 4.5 GYr (lower right). As expected the significance of being drawn from different populations is least when the distribution at each age is compared with itself. The different symbols represent the number of particles drawn from each distribution as shown in the legend. About 50-100 resonant objects are needed to strongly distinguish ages that differ by only half a billion years.

Chapter 4

Orbits and Masses of the Satellites of Dwarf Planet Haumea (2003 EL61)

This chapter has been published in its entirety under the same title by authors D. Ragozzine and M. E. Brown in the *Astronomical Journal*, 2009, Volume 137, pp. 4766-4776. Reproduced by permission of the American Astronomical Society.

Abstract

Using precise relative astrometry from the Hubble Space Telescope and the W. M. Keck Telescope, we have determined the orbits and masses of the two dynamically interacting satellites of the dwarf planet (136108) Haumea, formerly 2003 EL61. The orbital parameters of Hi'iaka, the outer, brighter satellite, match well the previously derived orbit. On timescales longer than a few weeks, no Keplerian orbit is sufficient to describe the motion of the inner, fainter satellite Namaka. Using a fully-interacting three point-mass model, we have recovered the orbital parameters of both orbits and the mass of Haumea and Hi'iaka; Namaka's mass is marginally detected. The data are not sufficient to uniquely determine the gravitational quadrupole of the non-spherical primary (described by J_2). The nearly co-planar nature of the satellites, as well as an inferred density similar to water ice, strengthen the hypothesis that Haumea experienced a giant collision billions of years ago. The excited eccentricities and mutual inclination point to an intriguing tidal history of significant semi-major axis evolution through satellite mean-motion resonances. The orbital solution indicates that Namaka and Haumea are currently undergoing mutual events and that the mutual event season will last for the next several years.

4.1 Introduction

The dwarf planet (136108) Haumea, formerly 2003 EL61, and about 3/4 of other large Kuiper belt objects (KBOs) have at least one small close-in satellite (Weaver et al., 2006; Brown et al., 2006; Brown & Suer, 2007). All of these larger KBOs are part of the excited Kuiper belt, where the detectable binary fraction among smaller KBOs is much lower, only a few percent (Stephens & Noll, 2006). In contrast, the cold classical population (inclinations $\lesssim 5^\circ$) has no large KBOs (Levison & Stern, 2001; Brown, 2008), but prevalent widely separated binaries with nearly equal masses (Noll et al., 2008b). The differences between the types and frequency of Kuiper belt binaries may point to different binary formation mechanisms. Small satellites of large KBOs appear to be formed by collision, as proposed for the Pluto system (Canup, 2005; Stern et al., 2006), Eris and Dysnomia (Brown & Schaller, 2007, but see Greenberg & Barnes, 2008), and Haumea (Barkume et al., 2006; Brown et al., 2007; Fraser & Brown, 2009), but smaller KBO binaries have more angular momentum than can be generated in typical impacts and are apparently formed by some other mechanism (e.g., Weidenschilling, 2002; Goldreich et al., 2002; Funato et al., 2004; Astakhov et al., 2005; Nesvorny, 2008). Both mechanisms of binary formation require higher number densities than present in the current Kuiper belt, as modeled explicitly for the Haumea collision by Levison et al. (2008).

The collisional origin of Haumea’s two satellites — the outer, brighter satellite Hi’iaka (S1) and the inner, fainter satellite Namaka (S2) — is inferred from several related observations. Haumea has a moderate-amplitude light-curve and the shortest rotation period (3.9155 hours) among known objects of its size (Rabinowitz et al., 2006). The rapid rotation requires a large spin angular momentum, as imparted by a large oblique impact. Using the mass of Haumea derived by the orbit of Hi’iaka (Brown et al., 2005, hereafter B05), assuming Haumea’s rotation axis is nearly perpendicular to the line-of-sight (like the satellites’ orbits), and assuming the shape is that of a Jacobi ellipsoid (a homogeneous fluid), the photometric light curve can be used to determine the size, shape, albedo, and density of Haumea (Rabinowitz et al., 2006; Lacerda & Jewitt, 2007, but see Holsapple, 2007). It is estimated that Haumea is a tri-axial ellipsoid with approximate semi-axes of $500 \times 750 \times 1000$ km with a high albedo (0.73) and density (2.6 g/cm^3), as determined by Rabinowitz et al. (2006). This size and albedo are consistent with Spitzer radiometry (Stansberry et al., 2008). The inferred density is near that of rock and higher than all known KBOs implying an atypically small ice fraction.

Haumea is also the progenitor of the only known collisional family in the Kuiper belt (Brown et al., 2007). It seems that the collision that imparted the spin angular momentum also fragmented and removed the icy mantle of the proto-Haumea (thus increasing its density) and ejected these fragments into their own heliocentric orbits. The Haumea family members are uniquely identified by deep water ice spectra and optically neutral color (Brown et al., 2007), flat phase curves (Rabinowitz et al., 2008), and tight dynamical clustering (Ragozzine & Brown, 2007). The dynamical clustering

is so significant that Ragozzine & Brown (2007) were able to correctly predict that 2003 UZ117 and 2005 CB79 would have deep water ice spectra characteristic of the Haumea family, as verified by Schaller & Brown (2008). The distribution of orbital elements matches the unique signature of a collisional family, when resonance diffusion (e.g., Nesvorný & Roig, 2001) is taken into account. Using this resonance diffusion as a chronometer, Ragozzine & Brown (2007) find that the Haumea family-forming collision occurred at least 1 GYr ago and is probably primordial. This is consistent with the results of Levison et al. (2008), who conclude that the Haumea collision is only probable between two scattered-disk objects in the early outer solar system when the number densities were much higher.

In this work, we have derived the orbits and masses of Haumea, Hi'iaka, and Namaka. In Section 2, we describe the observations used to determine precise relative astrometry. The orbit-fitting techniques and results are given in Section 3. Section 4 discusses the implications of the derived orbits on the past and present state of the system. We conclude the discussion of this interesting system in Section 5.

4.2 Observations and Data Reduction

Our data analysis uses observations from various cameras on the Hubble Space Telescope (HST) and the NIRC2 camera with Laser Guide Star Adaptive Objects at the W. M. Keck Observatory. These observations are processed in different ways; here we describe the general technique and below we discuss the individual observations. Even on our relatively faint targets ($V \approx 21, 22$), these powerful telescopes can achieve relative astrometry with a precision of a few milliarcseconds. The Julian Date of observation, the relative astrometric distance on-the-sky, and the estimated astrometric errors are reported in Table 4.1.

Table 4.1. Observed Astrometric Positions for the Haumea System

Julian Date	Date	Telescope	Camera	Δx_H arcsec	Δy_H arcsec	$\sigma \Delta x_H$ arcsec	$\sigma \Delta y_H$ arcsec	Δx_N	Δy_N	$\sigma \Delta x_N$	$\sigma \Delta y_N$
2453397.162	2005 Jan 26	Keck	NIRC2	0.03506	-0.63055	0.01394	0.01394
2453431.009	2005 Mar 1	Keck	NIRC2	0.29390	-1.00626	0.02291	0.02291	0.00992	0.52801	0.02986	0.02986
2453433.984	2005 Mar 4	Keck	NIRC2	0.33974	-1.26530	0.01992	0.01992
2453518.816	2005 May 28	Keck	NIRC2	-0.06226	0.60575	0.00996	0.00996
2453551.810	2005 Jun 30	Keck	NIRC2	-0.19727	0.52106	0.00498	0.00996	-0.03988	-0.65739	0.03978	0.03978
2453746.525	2006 Jan 11	HST	ACS/HRC	-0.20637	0.30013	0.00256	0.00256	0.04134	-0.18746	0.00267	0.00267
2453746.554	2006 Jan 11	HST	ACS/HRC	-0.20832	0.30582	0.00257	0.00257	0.03867	-0.19174	0.00267	0.00267
2454138.287	2007 Feb 6	HST	WFPC2	-0.21088	0.22019	0.00252	0.00197	-0.02627	-0.57004	0.00702	0.00351
2454138.304	2007 Feb 6	HST	WFPC2	-0.21132	0.22145	0.00095	0.00204	-0.03107	-0.56624	0.00210	0.00782
2454138.351	2007 Feb 6	HST	WFPC2	-0.21515	0.23185	0.00301	0.00206	-0.03009	-0.55811	0.00527	0.00564
2454138.368	2007 Feb 6	HST	WFPC2	-0.21402	0.23314	0.00192	0.00230	-0.03133	-0.56000	0.00482	0.00663
2454138.418	2007 Feb 6	HST	WFPC2	-0.21705	0.24202	0.00103	0.00282	-0.03134	-0.54559	0.00385	0.00376
2454138.435	2007 Feb 6	HST	WFPC2	-0.21449	0.24450	0.00323	0.00254	-0.02791	-0.54794	0.00571	0.00524
2454138.484	2007 Feb 6	HST	WFPC2	-0.21818	0.25301	0.00153	0.00224	-0.02972	-0.53385	0.00797	0.01330
2454138.501	2007 Feb 7	HST	WFPC2	-0.21807	0.25639	0.00310	0.00291	-0.03226	-0.53727	0.00531	0.00400
2454138.551	2007 Feb 7	HST	WFPC2	-0.22173	0.26308	0.00146	0.00230	-0.03429	-0.53079	0.00497	0.00582
2454138.567	2007 Feb 7	HST	WFPC2	-0.21978	0.26791	0.00202	0.00226	-0.03576	-0.52712	0.00270	0.00479
2454469.653	2008 Jan 4	HST	WFPC2	0.23786	-1.27383	0.00404	0.00824	-0.02399	-0.28555	0.00670	0.00831
2454552.897	2008 Mar 27	Keck	NIRC2	0.19974	-0.10941	0.00930	0.00956
2454556.929	2008 Mar 31	Keck	NIRC2	0.32988	-0.77111	0.00455	0.00557	0.00439	-0.76848	0.01239	0.01280
2454556.948	2008 Mar 31	Keck	NIRC2	0.33367	-0.77427	0.00890	0.00753	0.01363	-0.76500	0.01976	0.01252
2454556.964	2008 Mar 31	Keck	NIRC2	0.33267	-0.77874	0.00676	0.00485	0.00576	-0.77375	0.01212	0.01283
2454557.004	2008 Mar 31	Keck	NIRC2	0.33543	-0.78372	0.00404	0.00592	0.00854	-0.77313	0.01199	0.00897
2454557.020	2008 Mar 31	Keck	NIRC2	0.33491	-0.78368	0.00374	0.00473	0.00075	-0.76974	0.00907	0.01015
2454557.039	2008 Mar 31	Keck	NIRC2	0.33712	-0.78464	0.00740	0.00936	0.00988	-0.77084	0.01793	0.01543
2454557.058	2008 Mar 31	Keck	NIRC2	0.33549	-0.78692	0.00868	0.00852	0.01533	-0.76117	0.00765	0.01571
2454557.074	2008 Mar 31	Keck	NIRC2	0.33128	-0.78867	0.01431	0.01411	0.00645	-0.76297	0.01639	0.01390
2454557.091	2008 Mar 31	Keck	NIRC2	0.33687	-0.79462	0.00803	0.00717	0.00708	-0.76986	0.01532	0.00787
2454593.726	2008 May 7	HST	NICMOS	-0.18297	1.08994	0.00354	0.00425	0.00243	-0.75878	0.00576	0.00761
2454600.192	2008 May 13	HST	WFPC2	0.10847	0.17074	0.00508	0.00427	-0.02325	0.19934	0.00480	0.01161
2454601.990	2008 May 15	HST	WFPC2	0.18374	-0.13041	0.00729	0.00504	-0.02293	0.50217	0.00618	0.00614
2454603.788	2008 May 17	HST	WFPC2	0.24918	-0.43962	0.00207	0.00574	-0.01174	0.59613	0.00366	0.00485
2454605.788	2008 May 19	HST	WFPC2	0.29818	-0.75412	0.00467	0.00966	0.00006	0.29915	0.00425	0.00613

Note. — Summary of observations of the astrometric positions of Hi'iaka (H) and Namaka (N) relative to Haumea. The difference in brightness (~ 6) and orbital planes allow for a unique identification of each satellite without possibility of confusion. The method for obtaining the astrometric positions and errors is described in Section 4.2 and Brown et al. (2005). On a few dates, the fainter Namaka was not detected because the observations were not of sufficiently deep or Namaka was located within the PSF of Haumea. This data is shown graphically in Figure 4.2 and the residuals to the fit shown in Figure 4.3. For reasons described in the text, only the HST data is used to calculate the orbital parameters, which are shown in Table 4.2.

Observations from Keck are reduced as in B05. Known bad pixels were interpolated over and each image divided by a median flat-field. The images were then pair-wise subtracted (from images taken with the same filter). The astrometric centroid of each of the visible objects is determined by fitting two-dimensional Gaussians. Converting image distance to on-the-sky astrometric distance is achieved using the recently derived pixel scale of Ghez et al. (2008), who calibrate the absolute astrometry of the NIRC2 camera and find a plate scale of $0.009963''/\text{pixel}$ (compared to the previously assumed value of $0.009942''/\text{pixel}$) and an additional rotation of 0.13° compared with the rotation information provided in image headers. Ghez et al. (2008) and Helminiak & Konacki (2008) find that the plate-scale and rotation are stable over the timescale of our observations. Error bars are determined from the scatter of the measured distances from each individual image; typical integration times were about 1 minute. When the inner satellite is not detected in individual images, but can be seen in the stacked image, then the position is taken from the stacked image, after individually rotating, and the error bars are simply scaled to the error bars of the outer satellite by multiplying by the square root of the ratio of signal/noise (~ 5). The minute warping of the NIRC2 fields¹ is much smaller than the quoted error bars.

HST benefits from a known and stable PSF and well-calibrated relative astrometry. This allows for precise measurements, even when the satellites are quite close to Haumea. For each of the HST observations, model PSFs were generated using Tiny Tim². The model PSFs assumed solar colors, as appropriate for Haumea and its satellites, and were otherwise processed according to the details given in *The Tiny Tim User's Guide*. All three PSFs were then fitted simultaneously to minimize χ^2 , with errors taken from photon and sky noise added in quadrature. Bad pixels and cosmic rays were identified by hand and masked out of the χ^2 determination. The distortion correction of Anderson & King (2003) for WFPC2 is smaller than our error bars for our narrow angle astrometry and was not included. Relative on-the-sky positions were calculated using the `xyad` routine of the IDL Astro Library, which utilizes astrometry information from the image headers.

The acquisition and analysis of the satellite images taken in 2005 at Keck are described in B05. However, there is a sign error in the R. A. Offsets listed in Table 1 of 2005; the values listed are actually the on-the-sky deviations (as visible from their Figure 1). Despite this typographical error, the fit of B05 was carried out correctly. The observed locations and estimated errors of the inner satellite are given in Brown et al. (2006). The astrometric positions reported in Table 4.1 are slightly different based on a reanalysis of some of the data as well as a new plate scale and rotation, discussed above. Based on our orbital solution and a reinvestigation of the images, we have determined that the May 28, 2005 observation of Namaka reported in Brown et al. (2006) was spurious; residual long-lived speckles from the adaptive optics correction are often difficult to distinguish from faint

¹See the NIRC2 Astrometry page at http://www2.keck.hawaii.edu/inst/nirc2/forReDoc/post_observing/dewarp/.

²Available at <http://www.stsci.edu/software/tinytim/tinytim.html>.

close-in satellites.

In 2006, HST observed Haumea with the High Resolution Camera of the Advanced Camera for Surveys (Program 10545). Two five minute integrations were taken at the beginning and end of a single orbit. The raw images were used for fitting, requiring distorted PSFs and distortion-corrected astrometry. The astrometric accuracy of ACS is estimated to be ~ 0.1 pixels to which we add the photon noise error in the positions of the three objects. The high precision of ACS allows for motion to be detected between these two exposures, so these errors are not based on the scatter of multiple measurements as with all the other measurements.

At the beginning of February 2007, Hubble observed Haumea for 5 orbits, obtaining highly accurate positions for both satellites (Program 10860). The motion of the satellites from orbit to orbit is easily detected, and motion during a single orbit can even be significant, so we subdivided these images into 10 separate “observations”. The timing of the observations were chosen to have a star in the field of view, from which the Tiny Tim PSF parameters are modeled in manner described in Brown & Trujillo (2004). The observations do not track Haumea, but are fixed on the star to get the best PSF which is then appropriately smeared for the motion of the objects. Even though these observations were taken with the Wide Field Planetary Camera — the ACS High-Resolution Camera failed only a week earlier — the PSF fitting works excellently and provides precise positions. Astrometric errors for these observations were determined from the observed scatter in positions after subtracting the best fit quadratic trend to the data, so that observed orbital motion is not included in the error estimate. We note here that combined deep stacks of these images revealed no additional outer satellites brighter than $\sim 0.25\%$ fractional brightness at distances out to about a tenth of the Hill sphere (i.e., about 0.1% of the volume where additional satellites would be stable).

In 2008, we observed Haumea with Keck NIRC2 on the nights of March 28 and March 31. The observations on March 31 in H band lasted for about 5 hours under good conditions, with clear detections of both satellites in each image. These were processed as described above. Observations where Haumea had a large FWHM were removed; about 75% of the data was kept. As with the February 2007 HST data, we divided the observations into 10 separate epochs and determined errors from scatter after subtracting a quadratic trend. The motion of the outer satellite is easily detected, but the inner satellite does not move (relative to Haumea) within the errors because it is at southern elongation. The March 28 data was not nearly as good as the March 31 data due to poor weather conditions and only the outer satellite is clearly detected.

In early May 2008, HST observed Haumea using the NICMOS camera (Program 11169). These observations were processed as described above, though a few images with obvious astrometric errors (due to the cosmic rays which riddle these images) were discarded. These are the same observations discussed by Fraser & Brown (2009).

In mid-May 2008, we observed Haumea at five epochs using the Wide Field Planetary Camera

(WFPC2), over the course of 8 days (Program 11518). Each of these visits consisted of four ~ 10 minute exposures. These data, along with an observation in January 2008, were processed as described above. Although we expect that some of these cases may have marginally detected motion of the satellites between the four exposures, ignoring the motion only has the effect of slightly inflating the error bars for these observations. Namaka was too close to Haumea ($\lesssim 0.1''$) to observe in the May 12, 2008 image, which is not used.

The derived on-the-sky relative astrometry for each satellite, along with the average Julian Date of the observation and other information are summarized in Table 4.1. These are the astrometric data used for orbit fitting in this paper. In earlier attempts to determine the orbit of Namaka, we also obtained other observations. On the nights of April 20 and 21, 2006, we observed Haumea with the OSIRIS camera and LGSAO at Keck. Although OSIRIS is an integral-field spectrometer, our observations were taken in photometric mode. In co-added images, both satellites were detected on both nights. We also received queue-scheduled observations of Haumea with the NIRI camera on Gemini and the LGSAO system Altair. In 2007, our Gemini program resulted in four good nights of data on April 9 and 13, May 4, and June 5. In 2008, good observations were taken on April 20, May 27, and May 28. In each of the Gemini images, the brighter satellite is readily found, but the fainter satellite is often undetectable.

The accuracy of the plate scale and rotation required for including OSIRIS and Gemini observations is unknown, so these data are not used for orbit determination. We have, however, projected the orbits derived below to the positions of all known observations. The scatter in the Monte Carlo orbital suites (described below) at the times of these observations is small compared to the astrometric error bars of each observation, implying that these observations are not important for improving the fit. Predicted locations do not differ significantly from the observed locations, for any observation of which we are aware, including those reported in Barkume et al. (2006) and Lacerda (2008).

Using these observations, we can also do basic relative photometry of the satellites. The brightness of the satellites was computed from the height of the best-fit PSFs found to match the May 15, 2008 HST WFPC2 observation. Based on the well-known period and phase of the light curve of Haumea (Lacerda et al., 2008; D. Fabrycky, pers. comm.), Haumea was at its faintest during these observations and doesn't change significantly in brightness. Hi'iaka was found to be ~ 10 times fainter than Haumea and Namaka ~ 3.7 times fainter than Hi'iaka.

4.3 Orbit Fitting and Results

The orbit of Hi'iaka and mass of Haumea were originally determined by B05. From three detections of Namaka, Brown et al. (2006) estimated three possible orbital periods around 18, 19, and 35 days.

The ambiguity resulted from an under-constrained problem: at least 4-5 astrometric observations are required to fully constrain a Keplerian orbit. Even after additional astrometry was obtained, however, no Keplerian orbit resulted in a reasonable fit, where, as usual, goodness-of-fit is measured by the χ^2 statistic, and a reduced χ^2 of order unity is required to accept the orbit model. By forward integration of potential Namaka orbits, we confirmed that non-Keplerian perturbations due to Hi'iaka (assuming any reasonable mass) causes observationally significant deviations in the position of Namaka on timescales much longer than a month. Therefore, we expanded our orbital model to include fully self-consistent three-body perturbations.

4.3.1 Three Point-Mass Model

Determining the orbits and masses of the full system requires a 15-dimensional, highly non-linear, global χ^2 minimization. We found this to be impractical without a good initial guess for the orbit of Namaka to reduce the otherwise enormous parameter space, motivating the acquisition of multiple observations within a short enough timescale that Namaka's orbit is essentially Keplerian. Fitting the May 2008 HST data with a Keplerian model produced the initial guess necessary for the global minimization of the fully-interacting three point-mass model. The three point-mass model uses 15 parameters: the masses of the Haumea, Hi'iaka, and Namaka, and, for both orbits, the osculating semi-major axis, eccentricity, inclination, longitude of the ascending node, argument of periapse, and mean anomaly at epoch HJD 2454615.0 (= May 28.5, 2008). All angles are defined in the J2000 ecliptic coordinate system. Using these orbital elements, we constructed the Cartesian locations and velocities at this epoch as an initial condition for the three-body integration. Using a sufficiently small timestep (~ 300 seconds for the final iteration), a FORTRAN 90 program integrates the system to calculate the positions relative to the primary and the positions at the exact times of observation are determined by interpolation. (Observation times were converted to Heliocentric Julian Dates, the date in the reference frame of the Sun, to account for light-travel time effects due to the motion of the Earth and Haumea, although ignoring this conversion does not have a significant effect on the solution.) Using the JPL HORIZONS ephemeris for the geocentric position of Haumea, we vectorially add the primary-centered positions of the satellites and calculate the relative astrometric on-the-sky positions of both satellites. This model orbit is then compared to the data by computing χ^2 in the normal fashion. We note here that this model does not include gravitational perturbations from the Sun or center-of-light/center-of-mass corrections, which are discussed below.

Like many multi-dimensional non-linear minimization problems, searching for the best-fitting parameters required a global minimization algorithm to escape the ubiquitous local minima. Our algorithm for finding the global minimum starts with thousands of local minimizations, executed with the Levenberg-Marquardt algorithm `mpfit`³ using numerically-determined derivatives. These local

³An IDL routine available at <http://www.physics.wisc.edu/~craigm/idl/fitting.html>.

minimizations are given initial guesses that cover a very wide range of parameter space. Combining all the results of these local fits, the resultant parameter vs. χ^2 plots showed the expected parabolic shape (on scales comparable to the error bars) and these were extrapolated to their minima. This process was iterated until a global minimum is found; at every step, random deviations of the parameters were added to the best-fit solutions, to ensure a full exploration of parameter space. Because many parameters are highly correlated, the ability to find the best solutions was increased significantly by adding correlated random deviations to the fit parameters as determined from the covariance matrix of the best known solutions. We also found it necessary to optimize the speed of the evaluating of χ^2 from the 15 system parameters; on a typical fast processor this would take a few hundredths of a second and a full local minimization would take several seconds.

To determine the error bars on the fit parameters, we use a Monte Carlo technique (B05), as suggested in Press et al. (1992). Synthetic data sets are constructed by adding independent Gaussian errors to the observed data. The synthetic data sets are then fit using our global minimization routine, resulting in 86 Monte Carlo realizations; four of the synthetic data-sets did not reach global minima and were discarded, having no significant affect on the error estimates. One-sigma one-dimensional error bars for each parameter are given by the standard deviation of global-best parameter fits from these synthetic datasets. For each parameter individually, the distributions were nearly Gaussian and were centered very nearly on the best-fit parameters determined from the actual data. The error bars were comparable to error bars estimated by calculating where χ^2 increased by 1 from the global minimum (see Press et al., 1992).

First, we consider a solution using only the observations from HST. Even though these are taken with different instruments (ACS, NICMOS, and mostly WFPC2), the extensive calibration of these cameras allows the direct combination of astrometry into a single dataset. The best-fit parameters and errors are shown in Table 4.2. The reduced chi-square for this model is $\chi_{red}^2 = 0.64$ ($\chi^2 = 36.4$ with 57 degrees of freedom). The data are very well-fit by the three point mass model, as shown in Figures 4.2 and 4.3. A reduced χ^2 less than 1 is an indication that error bars are overestimated, assuming that they are independent; we note that using 10 separate “observations” for the Feb 2007 data implies that our observations are not completely independent. Even so, χ_{red}^2 values lower than 1 are typical for this kind of astrometric orbit fitting (e.g., Grundy et al., 2008). Each of the fit parameters is recovered, though the mass of Namaka is only detected with a $1.2\text{-}\sigma$ significance. Namaka’s mass is the hardest parameter to determine since it requires detecting minute non-Keplerian perturbations to orbit of the more massive Hi’iaka. The implications of the orbital state of the Haumea system are described in the next section. We also list in Table 4.3 the initial condition of the three-body integration for this solution.

The HST data are sufficient to obtain a solution for Hi’iaka’s orbit that is essentially the same as the orbit obtained from the initial Keck data in B05. Nevertheless, the amount and baseline of

Keck NIRC2 data is useful enough to justify adding this dataset to the fit. Simply combining these datasets and searching for the global minimum results in a significant degradation in the fit, going from a reduced χ^2 of 0.64 to a reduced χ^2 of ~ 1.10 , although we note that this is still an adequate fit. Adding the Keck data has the effect of generally lowering the error bars and subtly changing some of the retrieved parameters. Almost all of these changes are within the $\sim 1\text{-}\sigma$ error bars of the HST only solution, except for the mass estimate of Namaka. Adding the Keck data results in a best-fit Namaka mass a factor of 10 lower than the HST data alone. The largest mass retrieved from the entire Monte Carlo suite of solutions to the HST+Keck dataset is $\sim 8 \times 10^{17}$ kg, i.e., a Namaka/Haumea mass ratio of 2×10^{-4} , which is inconsistent with the brightness ratio of ~ 0.02 , for albedos less than 1 and densities greater than 0.3 g/cc. However, this solution assumes that the Keck NIRC2 absolute astrometry (based on the solution of Ghez et al. (2008), which is not directly cross-calibrated with HST) is perfectly consistent with HST astrometry. In reality, a small difference in the relative plate scale and rotation between these two telescopes could introduce systematic errors. Adding fitted parameters that adjust the plate scale and rotation angle does not help, since this results in overfitting, as verified by trial fitting of synthetic datasets. We adopt the HST-only solution, keeping in mind that the nominal mass of Namaka may be somewhat overestimated.

Using the Monte Carlo suite of HST-only solutions, we can also calculate derived parameters and their errors. Using Kepler’s Law (and ignoring the other satellite), the periods of Hi’iaka and Namaka are 49.462 ± 0.083 days and 18.2783 ± 0.0076 days, respectively, with a ratio of 2.7060 ± 0.0037 , near the 8:3 resonance. The actual mean motions (and resonance occupation) will be affected by the presence of the other satellite and the non-spherical nature of the primary (discussed below).

The mass ratios of the satellite to Haumea are 0.00451 ± 0.00030 and 0.00051 ± 0.00036 , respectively and the Namaka/Hi’iaka mass ratio is 0.116 ± 0.086 . The mutual inclination of the two orbits is $\phi = 13.41^\circ \pm 0.08^\circ$, where the mutual inclination is the actual angle between the two orbits, given by $\cos \phi = \cos i_H \cos i_N + \sin i_H \sin i_N \cos(\Omega_H - \Omega_N)$, where i and Ω are the inclination and longitude of ascending node. The origin of this significantly non-zero mutual inclination is discussed in Section 4.4.3.2. The mean longitude $\lambda \equiv \Omega + \omega + M$, is the angle between the reference line (J2000 ecliptic first point of Ares) and is determined well; the errors in the argument of periapse (ω) and mean anomaly (M) shown in Tabel 4.2 are highly anti-correlated. Our Monte Carlo results give $\lambda_H = 153.80 \pm 0.34$ degrees and $\lambda_N = 202.57 \pm 0.73$ degrees. Finally, under the nominal point-mass model, Namaka’s argument of periapse changes by about -6.5° per year during the course of the observations, implying a precession period of about 55 years; the non-Keplerian nature of Namaka’s orbit is detected with very high confidence.

Table 4.2. Fitted Parameters of the Haumea System

Object	Parameter	Value	Error	Units
Haumea	Mass	4.006	± 0.040	10^{21} kg
Hi'iaka	Mass	1.79	± 0.11	10^{19} kg
	Semi-major axis	49880	± 198	km
	Eccentricity	0.0513	± 0.0078	
	Inclination	126.356	± 0.064	degrees
	Longitude of ascending node	206.766	± 0.033	degrees
	Argument of periapse	154.1	± 5.8	degrees
	Mean anomaly	152.8	± 6.1	degrees
Namaka	Mass	1.79	± 1.48	10^{18} kg
	Semi-major axis	25657	± 91	km
	Eccentricity	0.249	± 0.015	
	Inclination	113.013	± 0.075	degrees
	Longitude of ascending node	205.016	± 0.228	degrees
	Argument of periapse	178.9	± 2.3	degrees
	Mean anomaly	178.5	± 1.7	degrees

Note. — Orbital parameters at epoch HJD 2454615.0. The nominal values are from the best fit to the HST data, while the (often correlated) error bars are the standard deviation of fitted values returned from a Monte Carlo suite of 86 datasets. These are the osculating orbital elements at this epoch; due to the three-body interactions, these values (especially the angles) change over the timescale of observations. All angles are referenced to the J2000 ecliptic coordinate system. See Table 4.3 for the Cartesian positions of the two satellites at this epoch.

Table 4.3. State Vector for the Haumea System

Object	x (m)	y (m)	z (m)	v_x (m/s)	v_y (m/s)	v_z (m/s)
Hi'iaka	-18879430	-36260639	-32433454	60.57621	1.85403	-34.81242
Namaka	-28830795	-13957217	-1073907	16.07022	-26.60831	-72.76764

Note. — Cartesian position and velocity of Haumea's satellites relative to Haumea in the J2000 ecliptic coordinate system at epoch HJD 2454615.0 corresponding to the best-fit orbital parameters shown in Table 4.2.

4.3.2 Including the J_2 of Haumea

The non-spherical nature of Haumea can introduce additional, potentially observable, non-Keplerian effects. The largest of these effects is due to the lowest-order gravitational moment, the quadrupole term (the dipole moment is 0 in the center of mass frame), described by J_2 (see, e.g., Murray & Dermott, 2000). Haumea rotates over 100 times during a single orbit of Namaka, which orbits quite far away at ~ 35 primary radii. To lowest order, therefore, it is appropriate to treat Haumea as having an “effective” time-averaged J_2 . Using a code provided by E. Fahnestock, we integrated trajectories similar to Namaka’s orbit around a homogeneous rotating tri-axial ellipsoid and have confirmed that the effective J_2 model deviates from the full model by less than half a milliarcsecond over three years.

The value of the effective J_2 ($\equiv -C_{20}$) for a rotating homogeneous tri-axial ellipsoid was derived by Scheeres (1994):

$$J_2 R^2 = \frac{1}{10}(\alpha^2 + \beta^2 - 2\gamma^2) \simeq 1.04 \times 10^{11} \text{m}^2 \quad (4.1)$$

where α, β , and γ are the tri-axial radii and the numerical value corresponds to a (498 x 759 x 980) km ellipsoid as inferred from photometry (Rabinowitz et al., 2006). We note that the physical quantity actually used to determine the orbital evolution is $J_2 R^2$; in a highly triaxial body like Haumea, it is not clear how to define R , so using $J_2 R^2$ reduces confusion. If R is taken to be the volumetric effective radius, then $R \simeq 652$ km and the $J_2 \simeq 0.244$. Note that the calculation and use of J_2 implicitly requires a definition of the rotation axis, presumed to be aligned with the shortest axis of the ellipsoid.

Preliminary investigations showed that using this value of $J_2 R^2$ implied a non-Keplerian effect on Namaka’s orbit that was smaller, but similar to, the effect of the outer satellite. The primary observable effect of both J_2 and Hi’iaka is the precession of apses and nodes of Namaka’s eccentric and inclined orbit (Murray & Dermott, 2000). When adding the three relevant parameters — $J_2 R^2$ and the direction of the rotational axis⁴ — to our fitting procedure, we found a direct anti-correlation between $J_2 R^2$ and the mass of Hi’iaka, indicating that these two parameters are degenerate in the current set of observations. The value of the reduced χ^2 was lowered significantly by the addition of these parameters, with the F-test returning high statistical significance. However, the best fits placed the satellites on polar orbits. We have verified that the fitted values of $J_2 R^2$ and the spin pole perpendicular to the orbital poles is due to over-fitting of the data. We generated simulated observations with the expected value of $J_2 R^2$ and with the satellites in nearly equatorial orbits. Allowing the global fitter to vary all the parameters resulted in an over-fitted solution that placed the satellites on polar orbits. Hence, allowing J_2 and the spin pole to vary in the fit is not justified; the effect of these parameters on the solution are too small and/or too degenerate to detect reliably.

⁴When adding J_2 , our three-body integration was carried out in the frame of the primary spin axis and then converted back to ecliptic coordinates.

Furthermore, since the model without these parameters already had a reduced χ^2 less than 1, these additional parameters were not warranted in the first place.

It is interesting, however, to consider how including this effect would change the determination of the other parameters. We therefore ran an additional set of models with a fixed J_2R^2 and fixing the spin pole (more accurately, the axis by which J_2 is defined) as the mass-weighted orbital pole of Hi'iaka and Namaka; since Hi'iaka is ~ 10 times more massive than Namaka, this puts Hi'iaka on a nearly equatorial orbit ($i \simeq 1^\circ$), as would be expected from collisional formation. Holding J_2R^2 fixed at $1.04 \times 10^{11} \text{ m}^2$, we reanalyzed the HST dataset using our global fitting routine. As expected, none of the parameters change by more than $1\text{-}\sigma$, except for the mass of Hi'iaka, which was reduced by almost 30% to $\sim 1.35 \times 10^{19} \text{ kg}$. (In fits where J_2R^2 was allowed to vary, the tradeoff between J_2R^2 and Hi'iaka's mass was roughly linear, as would be expected if the sum of these effects were forced to match the observationally determined precession of Namaka.) The data were well fit by the non-point mass model, with the forced J_2R^2 and spin pole solution reaching a global reduced χ^2 of 0.72. Since Haumea's high-amplitude light-curve indicates a primary with a large quadrupole component, the nominal mass of Hi'iaka in the point-mass case is almost certainly an overestimate of its true mass. More data will be required to disentangle the degeneracy between the mass of Hi'iaka and the J_2 of Haumea. Including J_2 and/or the Keck data do not improve the estimates of Namaka's mass.

4.4 Implications of Orbital Solutions

Taking the orbital solutions derived in the previous section, we can begin to answer questions relevant to the formation and evolution of this unique satellite system.

4.4.1 Mutual Events and Satellite Sizes

According to the orbit solution, the Haumea system is currently undergoing mutual events, as reported in (Fabrycky et al., 2008). (This is also true using the other orbit solutions, e.g., HST+Keck, with or without J_2 .) Using the known orbit, the angle between Namaka, Haumea, and the Earth (in the case of occultations) or the Sun (in the case of shadowing) falls well below the ~ 13 milliarcseconds ($\sim 500 \text{ km}$) of the projected shortest axis of Haumea. Observing multiple mutual events can yield accurate and useful measurements of several system properties as shown by the results of the Pluto-Charon mutual event season (e.g., Binzel & Hubbard, 1997). The depth of an event where Namaka occults Haumea leads to the ratio of albedos and, potentially, a surface albedo map of Haumea, which is known to exhibit color variations as a function of rotational phase, indicative of a variegated surface (Lacerda et al., 2008; Lacerda, 2008). Over the course of a single season, Namaka will traverse several chords across Haumea allowing for a highly accurate measurement of

Haumea’s size, shape, and spin pole direction (e.g., Descamps et al., 2008). The precise timing of mutual events will also serve as extremely accurate astrometry, allowing for an orbital solution much more precise than reported here. We believe that incorporating these events into our astrometric model will be sufficient to independently determine the masses of all three bodies and J_2R^2 . Our solution also predicts a satellite-satellite mutual event in July 2009 — the last such event until the next mutual event season begins around the year 2100. Our knowledge of the state of the Haumea system will improve significantly with the observation and analysis of these events. See <http://web.gps.caltech.edu/~mbrown/2003EL61/mutual> for up-to-date information on the Haumea mutual events. Note that both the mutual events and the three-body nature of the system are valuable for independently checking the astrometric analysis, e.g., by refining plate scales and rotations.

Using the best-fit mass ratio and the photometry derived in Section 4.2, we can estimate the range of albedos and densities for the two satellites. The results of this calculation are shown in Figure 4.4. The mass and brightness ratios clearly show that the satellites must either have higher albedos or lower densities than Haumea; the difference is probably even more significant than shown in Figure 4.4 since the nominal masses of Hi’iaka and Namaka are probably overestimated (see Section 4.3). The similar spectral (Barkume et al., 2006) and photometric (Fraser & Brown, 2009) properties of Haumea, Hi’iaka, and Namaka indicate that their albedos should be similar. Similar surfaces are also expected from rough calculations of ejecta exchange discussed by Stern (2009), though Benecchi et al. (2008) provide a contrary viewpoint. If the albedos are comparable, the satellite densities indicate a mostly water ice composition ($\rho \approx 1.0$ g/cc). This lends support to the hypothesis that the satellites are formed from a collisional debris disk composed primarily of water ice from the shattered mantle of Haumea. This can be confirmed in the future with a direct measurement of Namaka’s size from mutual event photometry. Assuming a density of water ice, the estimated radii of Hi’iaka and Namaka are ~ 160 km and ~ 80 km, respectively.

4.4.2 Long-term Orbital Integrations

It is surprising to find the orbits in an excited state, both with non-zero eccentricities and with a rather large mutual inclination. In contrast the regular satellite systems of the gas giants, the satellites of Mars, the three satellites of Pluto (Tholen et al., 2008), and asteroid triple systems with well known orbits (Marchis et al., 2005) are all in nearly circular and co-planar orbits. In systems of more than one satellite, perturbations between the satellites produce forced eccentricities and inclinations that will remain even with significant damping. If the excited state of the Haumea system is just a reflection of normal interactions, then there will be small free eccentricities and inclinations, which can be estimated by integrating the system for much longer than the precession timescales and computing the time average of these elements. Using this technique, and exploring the

entire Monte Carlo suite of orbital solutions, we find that the free eccentricity of Hi'iaka is ~ 0.07 , the free eccentricity of Namaka is ~ 0.21 , and the time-averaged mutual inclination is $\sim 12.5^\circ$. Non-zero free eccentricities and inclinations imply that the excited state of the system is not due to satellite-satellite perturbations. These integrations were calculated using the n-body code SyMBA (Levison & Duncan, 1994) using the regularized mixed variable symplectic method based on the mapping by Wisdom & Holman (1991). Integration of all the Monte Carlo orbits showed for ~ 2000 -years showed no signs of instability, though we do note that the system chaotically enters and exits the 8:3 resonance. The orbital solutions including $J_2 R^2 \simeq 1.04 \times 10^{11} \text{ m}^2$ were generally more chaotic, but were otherwise similar to the point-mass integrations.

These integrations did not include the effect of the Sun, which adds an additional minor torque to the system that is negligible ($\Delta\Omega \sim 10^{-5}$ degrees) over the timescale of observations. The effects of the sun on the satellite orbits on long-time scales were not investigated. While the relative inclination between the satellite orbits and Haumea's heliocentric orbit ($\sim 119^\circ$ for Hi'iaka and $\sim 105^\circ$ for Namaka) places this system in the regime where the Kozai effect can be important (Kozai, 1962; Perets & Naoz, 2008), the interactions between the satellites are strong enough to suppress weak Kozai oscillations due to the Sun, which are only active in the absence of other perturbations (Fabrycky & Tremaine, 2007).

We did not include any correction to our solution for possible differences between the center of light (more precisely, the center of fitted PSF) and center of mass of Haumea. This may be important since Lacerda et al. (2008) find that Haumea's two-peaked light curve can be explained by a dark red albedo feature, which could potentially introduce a systematic astrometric error. The February 2007 Hubble data and March 2008 Keck data, both of which span a full rotation, do not require a center-of-light/center-of-mass correction for a good fit, implying that the correction should be smaller than ~ 2 milliarcseconds (i.e., ~ 70 km). Examination of the all the astrometric residuals and a low reduced- χ^2 confirm that center-of-light/center-of-mass corrections are not significant at our level of accuracy. For Pluto and Charon, albedo features can result in spurious orbital astrometry because Pluto and Charon are spin-locked; this is not the case for Haumea. For Keck observations where Namaka is not detected (see Table 4.1), it is usually because of low signal-to-noise and Namaka's calculated position is not near Haumea. In the cases where Namaka's light contaminates Haumea, the induced photocenter error would be less than the observed astrometric error.

4.4.3 Tidal Evolution

All of the available evidence points to a scenario for the formation of Haumea's satellites similar to the formation of the Earth's moon: a large oblique collision created a disk of debris composed mostly of the water ice mantle of a presumably differentiated proto-Haumea. Two relatively massive moons coalesced from the predominantly water-ice disk near the Roche lobe. Interestingly, in studying

the formation of Earth’s Moon, about one third of the simulations of Ida et al. (1997) predict the formation of two moonlets with the outer moonlet ~ 10 times more massive than the inner moonlet. Although the disk accretion model used by Ida et al. (1997) made the untenable assumption that the remnant disk would immediately coagulate into solid particles, the general idea that large disks with sufficient angular momentum could result in two separate moons seems reasonable. Such collisional satellites coagulate near the Roche lobe (e.g., at distances of $\sim 3\text{--}5$ primary radii) in nearly circular orbits and co-planar with the (new) rotational axis of the primary. For Haumea, the formation of the satellites is presumably concurrent with the formation of the family billions of years ago (Ragozzine & Brown, 2007) and the satellites have undergone significant tidal evolution to reach their current orbits (B05).

4.4.3.1 Tidal Evolution of Semi-major Axes

The equation for the typical semi-major axis tidal expansion of a single-satellite due to primary tides is (Murray & Dermott, 2000):

$$\dot{a} = \frac{3k_{2p}}{Q_p} q \left(\frac{R_p}{a} \right)^5 n a \quad (4.2)$$

where k_{2p} is the second-degree Love number of the primary, Q_p is the primary tidal dissipation parameter (see, e.g., Goldreich & Soter, 1966), q is the mass ratio, R_p is the primary radius, a is the satellite semi-major axis, and $n \equiv \sqrt{\frac{GM_{\text{sat}}}{a^3}}$ is the satellite mean motion. As pointed out by B05, applying this equation to Hi’iaka’s orbit (using the new-found $q = 0.0045$) indicates that Haumea must be extremely dissipative: $Q_p \simeq 17$, averaged over the age of the solar system, more dissipative than any known object except ocean tides on the present-day Earth. This high dissipation assumes an unrealistically high $k_2 \simeq 1.5$, which would be achieved only if Haumea were perfectly fluid. Using the strength of a rocky body and the Yoder (1995) method of estimating k_2 , Haumea’s estimated k_{2p} is ~ 0.003 . Such a value of k_{2p} would imply a absurdly low and physically implausible $Q_p \ll 1$. Starting Hi’iaka on more distant orbits, e.g., the current orbit of Namaka, does not help much in this regard since the tidal expansion at large semi-major axes is the slowest part of the tidal evolution. There are three considerations, however, that may mitigate the apparent requirement of an astonishingly dissipative Haumea. First, if tidal forcing creates a tidal bulge that lags by a constant time (as in Mignard, 1980), then Haumea’s rapid rotation (which hardly changes throughout tidal evolution) would naturally lead to a significant increase in tidal evolution. In other words, if Q_p is frequency dependent (as it seems to be for solid bodies, see Efroimsky & Lainey, 2007), then an effective Q of ~ 16 may be equivalent to an object with a one-day rotation period maintaining an effective Q of 100, the typically assumed value for icy solid bodies. That is, Haumea’s higher-than-expected dissipation may be related to its fast rotation. Second, the above calculation used the volumetric radius $R_p \simeq 650$ km, in calculating the magnitude of the tidal bulge torque, where

we note that Equation 4.2 assumes a spherical primary. A complete calculation of the actual torque caused by tidal bulges on a highly non-spherical body is beyond the scope of this paper, but it seems reasonable that since tidal bulges are highly distance-dependent, the volumetric radius may lead to an underestimate in the tidal torque and resulting orbital expansion. Using $R_p \simeq 1000$ km, likely an overestimate, allows k_{2p}/Q_p to go down to 7.5×10^{-6} , consistent both with $k_{2p} \simeq 0.003$ and $Q_p \simeq 400$. Clearly, a reevaluation of tidal torques and the resulting orbital change for satellites around non-spherical primaries is warranted before making assumptions about the tidal properties of Haumea.

The third issue that affects Hi'iaka's tidal evolution is Namaka. While generally the tidal evolution of the two satellites is independent, if the satellites form a resonance it might be possible to boost the orbital expansion of Hi'iaka via angular momentum transfer with the more tidally affected Namaka. (Note that applying the semi-major axis evolution questions to Namaka requires a somewhat less dissipative primary, i.e., Q_p values ~ 8 times larger than discussed above.) Even outside of resonance, forced eccentricities can lead to higher dissipation in both satellites, somewhat increasing the orbital expansion rate. Ignoring satellite interactions and applying Equation 4.2 to each satellite results in the expected relationship between the mass ratio and the semi-major axis ratio of (Canup et al., 1999; Murray & Dermott, 2000):

$$\frac{m_1}{m_2} \simeq \left(\frac{a_1}{a_2} \right)^{13/2} \quad (4.3)$$

where evaluating the right-hand side using the determined orbits implies that $\frac{m_1}{m_2} \simeq 75.4 \pm 0.4$. This mass ratio is highly inconsistent with a brightness ratio of ~ 3.7 for the satellites, implying that the satellites have not reached the asymptotic tidal end-state. Equation 4.3 is also diagnostic of whether the tidally-evolving satellites are on converging or diverging orbits: that the left-hand side of Equation 4.3 is greater than the right-hand side implies that the satellites are on convergent orbits, i.e., the ratio of semi-major axes is increasing and the ratio of the orbital periods is decreasing (when not in resonance).

4.4.3.2 Tidal Evolution of Eccentricities and Inclinations

Turning now from the semi-major axis evolution, we consider the unexpectedly large eccentricities and non-zero inclination of the Namaka and Hi'iaka. None of the aforementioned considerations can explain the highly excited state of the Haumea satellite system. As pointed out by B05, a simple tidal evolution model would require that the eccentricities and, to some extent, inclinations are significantly damped when the satellites are closer to Haumea, as eccentricity damping is more efficient than semi-major axis growth. One would also expect that the satellites formed from a collision disk with low relative inclinations. So, while a mutual inclination of 13° is unlikely to occur

by random capture, a successful model for the origin of the satellites must explain why the satellites are relatively far from co-planar.

The unique current orbital state of the Haumea system is almost certainly due to a unique brand of tidal evolution. Terrestrial bodies are highly dissipative, but none (except perhaps some asteroid or KBO triple systems) have large significantly interacting satellites. On the other hand, gas giant satellite systems have multiple large interacting satellites, but very low dissipation and hence slow semi-major axis change. The change in semi-major axes is important because it causes a large change in the period ratio, allowing the system to cross many resonances, which can strongly change the nature of the system and its evolution. Even though Haumea is in a distinct niche of tidal parameter space, we can gain insights from studies of other systems, such as the evolution of satellites in the Uranian system (e.g., Tittlemore & Wisdom, 1988, 1989; Dermott et al., 1988; Malhotra & Dermott, 1990) or the interactions of tidally-evolving exoplanets (e.g., Wu & Goldreich, 2002; Ferraz-Mello et al., 2003). In addition, since the results of some Moon-forming impacts resulted in the creation of two moons (Ida et al., 1997), Canup et al. (1999) studied the tidal evolution of an Earth-Moon-moon system, in many ways similar to the Haumea system.

Using the results of these former investigations, we can qualitatively explain the excited state of the Haumean system. As the satellites were evolving outward at different rates, the ratio of orbital periods would periodically reach a resonant ratio. For example, as the current system is in/near the 8:3 resonance, it probably passed through the powerful 3:1 resonance in the relatively recent past. Since the satellites are on convergent orbits, they would generally get caught into these past resonances, even if their early eccentricities and inclinations were low. Note that this simple picture of resonance capture must be investigated numerically (as in, e.g., Tittlemore & Wisdom, 1988) and that higher-order resonances may act differently from lower-order resonances (Zhang & Hamilton, 2008). Further semi-major axis growth while trapped in the resonance rapidly pumps eccentricities and/or inclinations, depending on the type of resonance (e.g., Ward & Canup, 2006). This continues until the satellites chaotically escape from the resonance. Escaping could be a result of either excitation (related to secondary resonances, see Tittlemore & Wisdom, 1989; Malhotra & Dermott, 1990) and/or chaotic instability due to overlapping sub-resonances, split by the large J_2 of Haumea (Dermott et al., 1988). Outside of resonances, tidal dissipation in the satellites can damp eccentricities while the satellites are close to Haumea, but at their current positions, eccentricity damping is very ineffective even for highly dissipative satellites. Inclination damping is generally slower than eccentricity damping and was probably small even when the satellites were much closer to Haumea. Therefore a “recent” excitation by passage through a resonance (possibly the 3:1) can qualitatively explain the current orbital configuration, which has not had the time to tidally damp to a more circular co-planar state. Numerical integrations will be needed to truly probe the history of this intriguing system and may be able to constrain tidal parameters of Haumea, Hi’iaka, and/or

Namaka.

Note that early in the history of this system when the satellites were orbiting at much smaller semi-major axes ($a \lesssim 10R_p$), the tri-axial nature of the primary would have been much more important and could have significantly affected the satellite orbits (Scheeres, 1994). At some point during semi-major axis expansion secular resonances (such as the evection resonance) could also be important for exciting eccentricities and/or inclinations (Touma & Wisdom, 1998). Finally, tides raised on Haumea work against eccentricity damping; for certain combinations of primary and satellite values of k_2/Q , tides on Haumea can pump eccentricity faster than it is damped by the satellites (especially if Haumea is particularly dissipative). While eccentricity-pumping tides on Haumea may help in explaining the high eccentricities, producing the large mutual inclination (which is hardly affected by any tidal torques) is more likely to occur in a resonance passage, as with Miranda in the Uranian system (Tittlemore & Wisdom, 1989; Dermott et al., 1988).

4.5 Conclusions

Using new observations from the Hubble Space Telescope, we have solved for the orbits and masses of the two dynamically interacting satellites of the dwarf planet Haumea. A three-body model, using the parameters with errors given in Table 4.2, provides an excellent match to the precise relative astrometry given in Table 4.1. The orbital parameters of Hi'iaka, the outer, brighter satellite match well the orbit previously derived in Brown et al. (2005). The newly derived orbit of Namaka, the inner, fainter satellite has a surprisingly large eccentricity (0.249 ± 0.015) and mutual inclination to Hi'iaka of ($13.41^\circ \pm 0.08^\circ$). The eccentricities and inclinations are not due to mutual perturbations, but can be qualitatively explained by tidal evolution of the satellites through mean-motion resonances. The precession effect of the non-spherical nature of the elongated primary, characterized by J_2 , cannot be distinguished from the precession caused by the outer satellite in the current data.

The orbital structure of Haumea's satellites is unlikely to be produced in a capture-related formation mechanism (e.g., Goldreich et al., 2002). Only the collisional formation hypothesis (allowing for reasonable, but atypical, tidal evolution) can explain the nearly co-planar satellites (probably with low densities), the rapid spin and elongated shape of Haumea (Rabinowitz et al., 2006), and the Haumea collisional family of icy objects with similar surfaces and orbits (Brown et al., 2007).

The future holds great promise for learning more about the Haumea system, as the orbital solution indicates that Namaka and Haumea are undergoing mutual events for the next several years. This will provide excellent observational constraints on the size, shape, spin pole, density, and internal structure of Haumea and direct measurements of satellite radii, densities, and albedos. There are also interesting avenues for future theoretical investigations, especially into the unique nature of tidal evolution in the Haumean system. These insights into the formation and evolution

of the Haumean system can be combined with our understanding of other Kuiper belt binaries to investigate how these binaries form and to further decipher the history of the outer solar system.

Acknowledgments: We would like to thank Meg Schwamb, Aaron Wolf, Matt Holman, and others for valuable discussions and Eugene Fahnestock for kindly providing his code for gravity around tri-axial bodies. We also acknowledge observational support from Emily Schaller and Chad Trujillo. We especially acknowledge the encouragement and discussions of Dan Fabrycky. DR is grateful for the support of the Moore Foundation. This work was also supported by NASA Headquarters under the Earth and Space Sciences Fellowship and the Planetary Astronomy programs. This work is based on NASA/ESA Hubble Space Telescope program 11518 using additional data from programs 10545, 10860, and 11169. Support for all these programs was provided by NASA through grants HST-GO-10545, HST-GO-10860, HST-GO-11518, and HST-GO-11169 from the Space Telescope Science Institute (STScI), which is operated by the Association of Universities for Research in Astronomy, Inc., under NASA contract NAS 5-26555. Some data presented herein was obtained at the W. M. Keck Observatory, which is operated as a scientific partnership among the California Institute of Technology, the University of California, and the National Aeronautics and Space Administration. The observatory was made possible by the generous financial support of the W. M. Keck Foundation. The authors wish to recognize and acknowledge the very significant cultural role and reverence that the summit of Mauna Kea has always had within the indigenous Hawaiian community. We are most fortunate to have the opportunity to conduct observations of Haumea, Hi'iaka, and Namaka, which were named after Hawaiian goddesses.

Bibliography

- Anderson, J., & King, I. R. 2003, *Publications of the ASP*, 115, 113
- Astakhov, S. A., Lee, E. A., & Farrelly, D. 2005, *Monthly Notices of the RAS*, 360, 401.
[astro-ph/0504060](#)
- Barkume, K. M., Brown, M. E., & Schaller, E. L. 2006, *Astrophysical Journal, Letters*, 640, L87.
[arXiv:astro-ph/0601534](#)
- Benecchi, S. D., Noll, K. S., Grundy, W. M., Buie, M. W., Stephens, D. C., & Levison, H. F. 2008,
[ArXiv e-prints. 0811.2104](#)
- Binzel, R. P., & Hubbard, W. B. 1997, *Pluto and Charon*, ed. S.A. Stern, D.J. Tholen (U. Arizona Press:1997)
- Brown, M. E. 2008, *The Largest Kuiper Belt Objects (The Solar System Beyond Neptune)*, 335
- Brown, M. E., Barkume, K. M., Ragozzine, D., & Schaller, E. L. 2007, *Nature*, 446, 294
- Brown, M. E., Bouchez, A. H., Rabinowitz, D., Sari, R., Trujillo, C. A., van Dam, M., Campbell, R., Chin, J., Hartman, S., Johansson, E., Lafon, R., Le Mignant, D., Stomski, P., Summers, D., & Wizinowich, P. 2005, *Astrophysical Journal, Letters*, 632, L45
- Brown, M. E., & Schaller, E. L. 2007, *Science*, 316, 1585
- Brown, M. E., & Suer, T.-A. 2007, *IAU Circular*, 8812, 1
- Brown, M. E., & Trujillo, C. A. 2004, *Astronomical Journal*, 127, 2413
- Brown, M. E., van Dam, M. A., Bouchez, A. H., Le Mignant, D., Campbell, R. D., Chin, J. C. Y., Conrad, A., Hartman, S. K., Johansson, E. M., Lafon, R. E., Rabinowitz, D. L., Stomski, P. J., Jr., Summers, D. M., Trujillo, C. A., & Wizinowich, P. L. 2006, *Astrophysical Journal, Letters*, 639, L43. [arXiv:astro-ph/0510029](#)
- Canup, R. M. 2005, *Science*, 307, 546
- Canup, R. M., Levison, H. F., & Stewart, G. R. 1999, *Astronomical Journal*, 117, 603
- Dermott, S. F., Malhotra, R., & Murray, C. D. 1988, *Icarus*, 76, 295
- Descamps, P., Marchis, F., Pollock, J., Berthier, J., Vachier, F., Birlan, M., Kaasalainen, M., Harris, A. W., Wong, M. H., Romanishin, W. J., Cooper, E. M., Kettner, K. A., Wiggins, P., Kryszczyńska, A., Polinska, M., Coliac, J.-F., Devyatkin, A., Verestchagina, I., & Gorshanov, D. 2008, *Icarus*, 196, 578. [0710.1471](#)

- Efroimsky, M., & Lainey, V. 2007, *Journal of Geophysical Research (Planets)*, 112, 12003. 0709.1995
- Fabrycky, D., & Tremaine, S. 2007, *Astrophysical Journal*, 669, 1298. 0705.4285
- Fabrycky, D. C., Ragozzine, D., Brown, M. E., & Holman, M. J. 2008, *IAU Circular*, 8949, 1
- Ferraz-Mello, S., Beaugé, C., & Michtchenko, T. A. 2003, *Celestial Mechanics and Dynamical Astronomy*, 87, 99. [arXiv:astro-ph/0301252](#)
- Fraser, W. C., & Brown, M. E. submitted, 2009
- Funato, Y., Makino, J., Hut, P., Kokubo, E., & Kinoshita, D. 2004, *Nature*, 427, 518. [arXiv:astro-ph/0402328](#)
- Ghez, A. M., Salim, S., Weinberg, N. N., Lu, J. R., Do, T., Dunn, J. K., Matthews, K., Morris, M. R., Yelda, S., Becklin, E. E., Kremenek, T., Milosavljevic, M., & Naiman, J. 2008, *Astrophysical Journal*, 689, 1044. 0808.2870
- Goldreich, P., Lithwick, Y., & Sari, R. 2002, *Nature*, 420, 643. [arXiv:astro-ph/0208490](#)
- Goldreich, P., & Soter, S. 1966, *Icarus*, 5, 375
- Greenberg, R., & Barnes, R. 2008, *Icarus*, 194, 847
- Grundy, W. M., Noll, K. S., Buie, M. W., Benecchi, S. D., Stephens, D. C., & Levison, H. F. 2008, *ArXiv e-prints*. 0812.3126
- Helminiak, K., & Konacki, M. 2008, *ArXiv e-prints*. 0807.4139
- Holsapple, K. A. 2007, *Icarus*, 187, 500
- Ida, S., Canup, R. M., & Stewart, G. R. 1997, *Nature*, 389, 353
- Kozai, Y. 1962, *Astronomical Journal*, 67, 591
- Lacerda, P. 2008, *ArXiv e-prints*. 0811.3732
- Lacerda, P., Jewitt, D., & Peixinho, N. 2008, *Astronomical Journal*, 135, 1749. 0801.4124
- Lacerda, P., & Jewitt, D. C. 2007, *Astronomical Journal*, 133, 1393. [arXiv:astro-ph/0612237](#)
- Levison, H. F., & Duncan, M. J. 1994, *Icarus*, 108, 18
- Levison, H. F., Morbidelli, A., Vokrouhlický, D., & Bottke, W. F. 2008, *Astronomical Journal*, 136, 1079. 0809.0553
- Levison, H. F., & Stern, S. A. 2001, *Astronomical Journal*, 121, 1730. [astro-ph/0011325](#)
- Malhotra, R., & Dermott, S. F. 1990, *Icarus*, 85, 444
- Marchis, F., Descamps, P., Hestroffer, D., & Berthier, J. 2005, *Nature*, 436, 822
- Mignard, F. 1980, *Moon and the Planets*, 23, 185
- Murray, C. D., & Dermott, S. F. 2000, *Solar System Dynamics* (Cambridge University Press)
- Nesvorný, D. 2008, in *AAS/Division for Planetary Sciences Meeting Abstracts*, vol. 40 of *AAS/Division for Planetary Sciences Meeting Abstracts*, 38.02
- Nesvorný, D., & Roig, F. 2001, *Icarus*, 150, 104
- Noll, K. S., Grundy, W. M., Stephens, D. C., Levison, H. F., & Kern, S. D. 2008, *Icarus*, 194, 758. 0711.1545

- Perets, H. B., & Naoz, S. 2008, ArXiv e-prints. 0809.2095
- Press, W. H., Teukolsky, S. A., Vetterling, W. T., & Flannery, B. P. 1992, Numerical recipes in FORTRAN. The art of scientific computing (Cambridge: University Press, —c1992, 2nd ed.)
- Rabinowitz, D. L., Barkume, K., Brown, M. E., Roe, H., Schwartz, M., Tourtellotte, S., & Trujillo, C. 2006, *Astrophysical Journal*, 639, 1238. arXiv:astro-ph/0509401
- Rabinowitz, D. L., Schaefer, B. E., Schaefer, M., & Tourtellotte, S. W. 2008, *Astronomical Journal*, 136, 1502. 0804.2864
- Ragozzine, D., & Brown, M. E. 2007, *Astronomical Journal*, 134, 2160. 0709.0328
- Schaller, E. L., & Brown, M. E. 2008, *Astrophysical Journal, Letters*, 684, L107. 0808.0185
- Scheeres, D. J. 1994, *Icarus*, 110, 225
- Stansberry, J., Grundy, W., Brown, M., Cruikshank, D., Spencer, J., Trilling, D., & Margot, J.-L. 2008, *Physical Properties of Kuiper Belt and Centaur Objects: Constraints from the Spitzer Space Telescope (The Solar System Beyond Neptune)*, 161
- Stephens, D. C., & Noll, K. S. 2006, *Astronomical Journal*, 131, 1142. arXiv:astro-ph/0510130
- Stern, S. A. 2009, *Icarus*, 199, 571. 0805.3482
- Stern, S. A., Weaver, H. A., Steffl, A. J., Mutchler, M. J., Merline, W. J., Buie, M. W., Young, E. F., Young, L. A., & Spencer, J. R. 2006, *Nature*, 439, 946
- Tholen, D. J., Buie, M. W., Grundy, W. M., & Elliott, G. T. 2008, *Astronomical Journal*, 135, 777. 0712.1261
- Tittemore, W. C., & Wisdom, J. 1988, *Icarus*, 74, 172
— 1989, *Icarus*, 78, 63
- Touma, J., & Wisdom, J. 1998, *Astronomical Journal*, 115, 1653
- Ward, W. R., & Canup, R. M. 2006, *Science*, 313, 1107
- Weaver, H. A., Stern, S. A., Mutchler, M. J., Steffl, A. J., Buie, M. W., Merline, W. J., Spencer, J. R., Young, E. F., & Young, L. A. 2006, *Nature*, 439, 943. astro-ph/0601018
- Weidenschilling, S. J. 2002, *Icarus*, 160, 212
- Wisdom, J., & Holman, M. 1991, *Astronomical Journal*, 102, 1528
- Wu, Y., & Goldreich, P. 2002, *Astrophysical Journal*, 564, 1024. arXiv:astro-ph/0108499
- Yoder, C. F. 1995, *Astrometric and Geodetic Properties of Earth and the Solar System*, 1
- Zhang, K., & Hamilton, D. P. 2008, *Icarus*, 193, 267

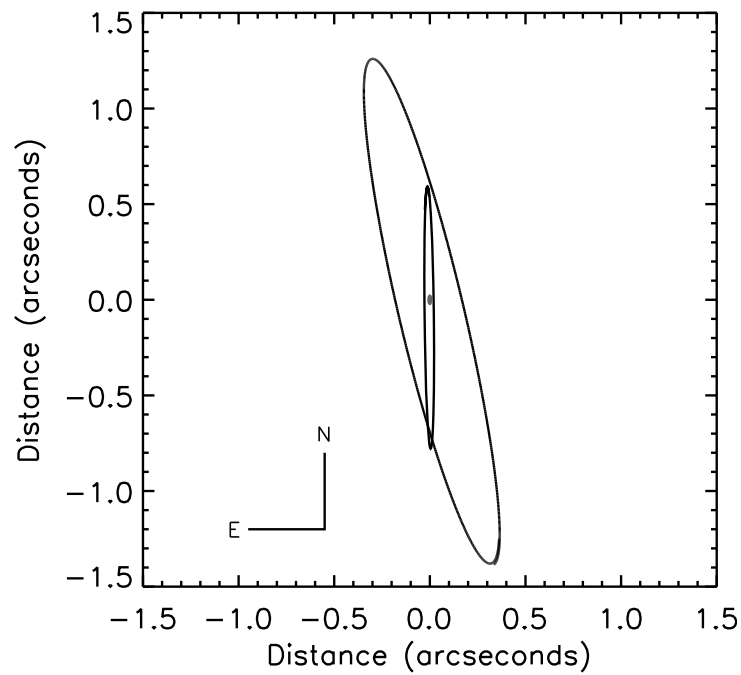


Figure 4.1 Relative positions of the satellites as viewed from Earth. The outer orbit corresponds to the brighter Hi'iaka and the inner orbit corresponds to the fainter Namaka. In the center is Haumea, drawn to scale, assuming an ellipsoid cross-section of 500 x 1000 km (Rabinowitz et al., 2006) with the long axis oriented North-South. The apparent orbit changes due to parallax and three-body effects; this is the view near March 2008. See Figure 4.2 for model and data positions throughout the observation period (2005-2008).

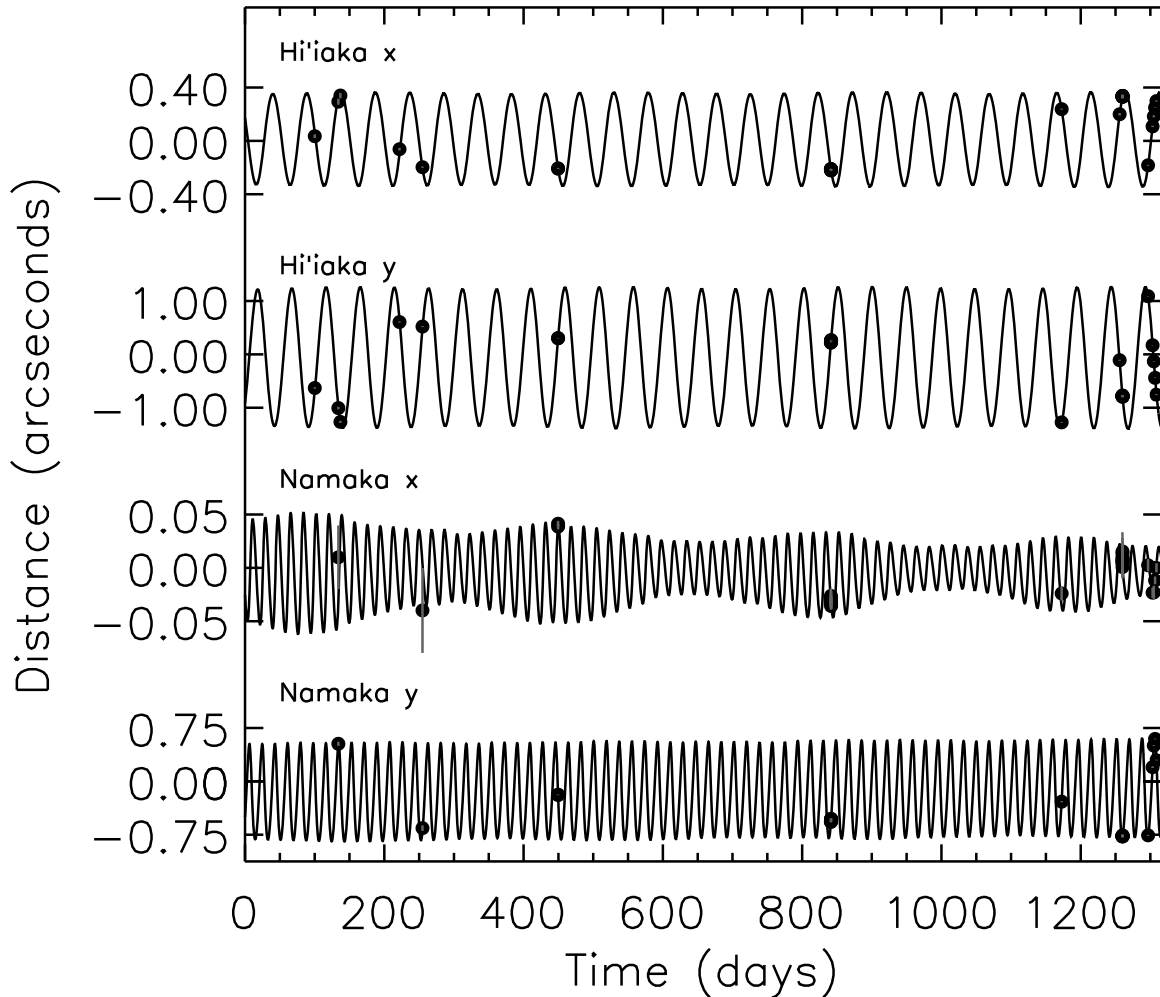


Figure 4.2 Observed positions and model positions of Hi'iaka and Namaka. From top to bottom, the curves represent the model on-the-sky position of Hi'iaka in the x -direction (i.e., the negative offset in Right Ascension), Hi'iaka in the y -direction (i.e., the offset in Declination), Namaka in the x -direction, and Namaka in the y -direction, all in arcseconds. Points represent astrometric observations as reported in Table 4.1. Error bars are also shown as gray lines, but are usually much smaller than the points. The three-point mass model shown here is fit to the HST-data only, with a reduced χ_{red}^2 of 0.64. The residuals for this solution are shown in Figure 4.3. Note that each curve has its own scale bar and that the curves are offset for clarity. The model is shown for 1260 days, starting on HJD 2453297.0, ~ 100 days before the first observation and ending just after the last observation. Visible are the orbital variations (~ 49.5 days for Hi'iaka and ~ 18.6 days for Namaka), the annual variations due to Earth's parallax, and an overall trend due to a combination of Haumea's orbital motion and the precession of Namaka's orbit.

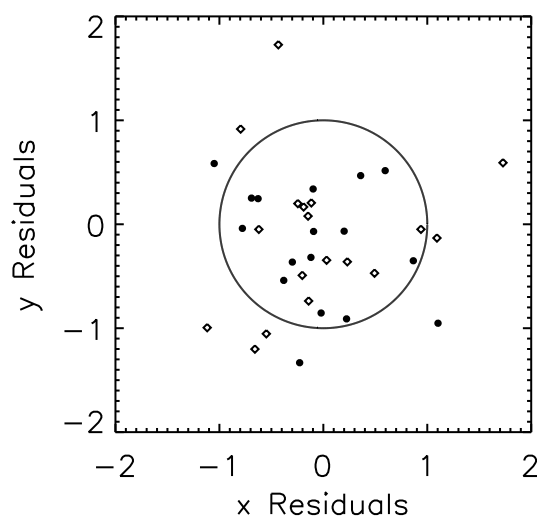


Figure 4.3 Normalized residuals of the three-point mass fit to HST-data only. Plotted is $(\Delta x_{\text{mod}} - \Delta x_{\text{obs}})/\sigma_{\Delta x}$ versus $(\Delta y_{\text{mod}} - \Delta y_{\text{obs}})/\sigma_{\Delta y}$ for Hi'iaka (diamonds) and Namaka (circles). Points that lie within the circle indicate where the model and observations vary by less than 1 error bar. See also Figure 4.2. The residuals are roughly evenly spaced and favor neither Hi'iaka nor Namaka, implying that there are no major systematic effects plaguing the three-body fit. As reported in the text this solution has a reduced χ^2_{red} of 0.64.

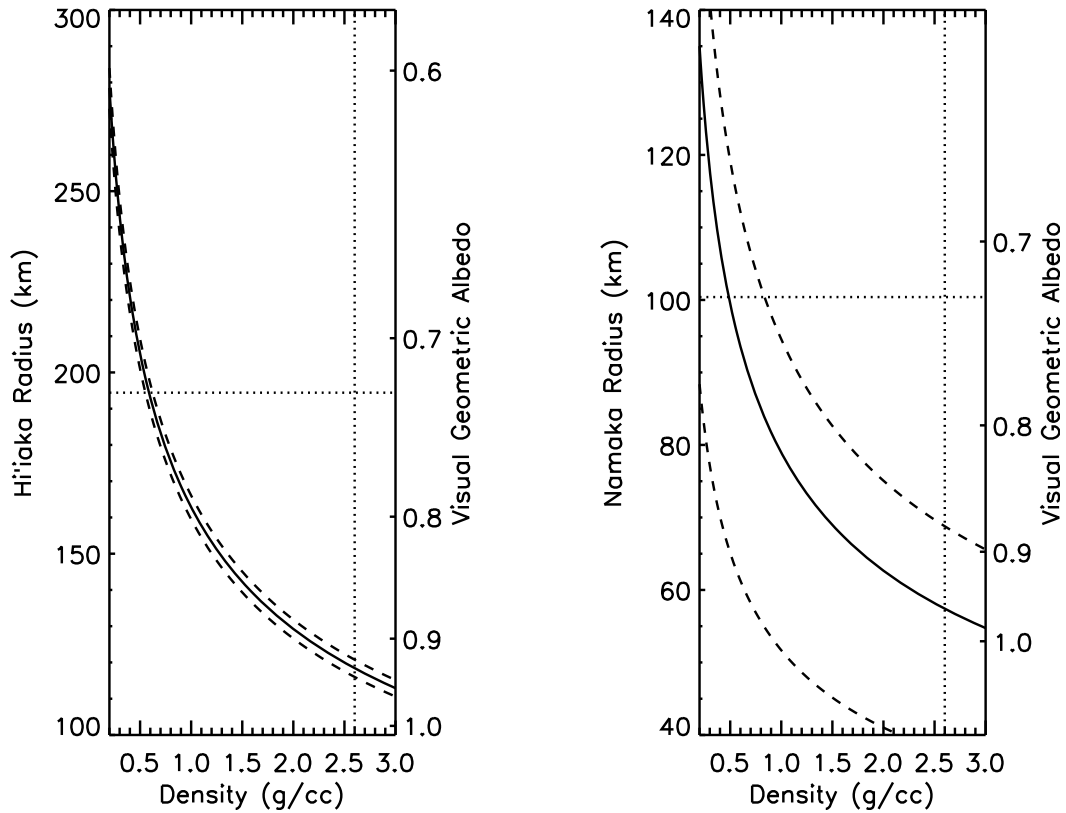


Figure 4.4 Relationship between radius, density, and albedo for Hi'iaka (left) and Namaka (right). A range of possible albedos and densities can reproduce the determined mass and brightness ratios of Hi'iaka and Namaka, which are assumed to be spherical. The solid lines show the relationship for the nominal masses, reported in Table 4.2, with dotted lines showing the 1- σ mass error bars. Note that the mass of both Hi'iaka and Namaka may be overestimated (due to insufficient data, see Section 4.3). The albedo and density of the Rabinowitz et al. (2006) edge-on model for Haumea are shown by dotted lines. Both satellites must have lower densities and/or higher albedos than Haumea. The similar spectral (Barkume et al., 2006) and photometric (Fraser & Brown, 2009) properties of Haumea, Hi'iaka, and Namaka indicate that their albedos should be similar. Under the assumption that the satellites have similar albedos to Haumea, the densities of the satellites indicate that they are primarily composed of water ice ($\rho \approx 1.0$ g/cc). Low satellite densities would bolster the hypothesis that the satellites formed from the collisional remnants of the water ice mantle of the differentiated proto-Haumea. Observation of Haumea-Namaka mutual events will allow for much more precise and model-independent measurements of Namaka's radius, density, and albedo.

Chapter 5

On the Tidal Evolution of Kuiper Belt Binaries

Abstract

The formation and evolution of binary Kuiper belt objects (KBOs) is closely intertwined with the history of the outer solar system. The interpretation of the currently observed characteristics of these binaries must include an understanding of effects that can significantly modify their orbital properties. Two major sources of potential modification include tidal dissipation and perturbations from the Sun. As a first step in understanding these effects, we describe the results of a new orbital evolution model that accounts for tidal dissipation at arbitrary eccentricity, the importance of Kozai cycles induced by the Sun, and orbital precession due to non-hydrostatic asymmetries of small solid bodies. In particular, we find that Kozai Cycles with Tidal Friction (KCTF) can significantly shrink the orbits of KBO binaries and may produce systems that would otherwise appear to be formed by collisions, with the Orcus-Vanth binary as the primary example. The unique observational signatures of KCTF are discussed along with other consequences of orbital and tidal evolution of KBO binary orbits.

5.1 Introduction

Investigating the origins of binary Kuiper belt objects (KBOs) holds significant promise for improving our understanding of the formation of the outer solar system. Although only ~ 60 KBO binaries are known, with only ~ 20 well-characterized orbits, there are already several observational trends that may be unique clues into processes active in the early solar system (Noll et al., 2008a,b). Brown et al. (2006) found that the binary fraction of large KBOs is significantly higher than the binary fraction of smaller KBOs, a result which continues to be true as more binaries are found (Brown, 2008). Noll et al. (2008b) recently reported that the binary fraction of non-resonant KBOs with low heliocentric inclinations ($29.3 \pm_{6.3}^{7.2}$ %) is strikingly different from the binary fraction of high inclination KBOs of similar sizes ($2.9 \pm_{2.4}^{6.5}$ %). Since there is also a strong trend of increasing binary frequency at small separations (Noll et al., 2008a), these binary fractions are certainly underestimates since the observations cannot resolve binaries at the smallest separations. The relative brightness of binary components is heavily skewed towards equal-brightness binaries, a result that appears to be robust despite some observational bias (Noll et al., 2008a). Finally, Benecchi et al. (2009) have found that the visible colors of KBO binary components are the same, even though the range of colors is as large as the range of colors for (apparently) single objects.

To describe the wide range of binaries, two general classes of binary formation mechanisms have been proposed, which we call the collision and capture mechanisms. Small satellites of large KBOs appear to be formed by collision, as proposed for the Pluto (Canup, 2005; Stern et al., 2006) and Haumea (Ragozzine & Brown, 2009) systems. Smaller KBO binaries appear to have more angular momentum than can be generated in typical impacts and are apparently formed by some other mechanism which does not involve direct contact (e.g., Weidenschilling, 2002; Goldreich et al., 2002; Funato et al., 2004; Astakhov et al., 2005; Nesvorny, 2008). All proposed mechanisms of binary formation require higher number densities than present in the current Kuiper belt and were mostly active in the dynamically cold primordial planetesimal disk. Later excitation of this primordial disk sculpted the Kuiper belt seen today (e.g., Morbidelli et al., 2008). The two different models of binary formation predict different kinds of binaries. Collisionally-formed binaries will have low angular momenta and an isotropic inclination distribution (since the final inclination is given mostly by the random impact location). Binaries formed through capture will have higher amounts of angular momentum and a more bimodal inclination distribution around $i \simeq 0^\circ, 180^\circ$ (Schlichting & Sari, 2008b). In some regards, the two different binary formation mechanisms map well to the two different classes of binaries, with small satellites in tight circular orbits around large KBOs formed by collision and equal mass binaries with wide orbits formed by capture. Nevertheless, several important details require further investigation.

In particular, the current orbital properties of KBOs may not represent the initial orbital distri-

bution. Without a clear understanding of the processes that can modify KBO binary orbits, there is no sure way to extrapolate the present-day observational trends backwards in time in order to gain insights into binary formation mechanisms. Potentially important processes that can modify KBO binary orbits include: 1) close interactions with the giant planets that transported KBOs from the primordial planetesimal disk to their current position in an excited Kuiper belt; 2) interactions with passing and colliding KBOs both early in the solar system and in the present-day Kuiper belt (Stern et al., 2003; Collins & Sari, 2008); 3) orbital perturbations of the binary orbit due to the planets and the Sun (Perets & Naoz, 2008, hereafter PN09); and 4) tidal interactions that can change binary orbital elements over long timescales. In this work, we undertake a preliminary investigation of the last two processes, specifically the orbital and tidal evolution of KBO binaries, including perturbations from the Sun. We note that many of the same techniques and results are relevant to the orbital evolution of asteroid binaries (PN09).

The tidal evolution of KBO binaries is not like the tidal evolution of planetary satellites and requires a substantially different approach. The main reasons for these differences in KBO binaries including the following, some of which were pointed out by Noll et al. (2008a).

- In many KBO binaries, the primary and secondary are of comparable size. Most discussions and derivations of tidal evolution assume one object is much larger than the other.
- The eccentricities of these systems can be relatively high ($e \gtrsim 0.2$), requiring the use of oft-neglected higher-order terms in the tidal evolution equations (e.g., Wisdom, 2008).
- The ratio of the strength of primary and secondary tides may be unlike other systems, leading to atypical results. For example, tides in a fast-spinning primary may easily be strong enough to cause the orbital eccentricity to grow in time, unlike the typical decrease in eccentricity that is usually expected.
- The tidal dissipation parameters (k_2 and Q , described below) are unconstrained for these icy bodies even to within an order of magnitude.

For the above reasons, the tidal evolution of KBO binaries has not been modeled in any significant detail, with the exceptions of early studies of the Pluto-Charon system (e.g., Dobrovolskis et al., 1997), recent studies of how Pluto’s small additional moons Nix and Hydra can be placed into the tidal evolution story, and a study of the evolution of Eris-Dysnomia system (Greenberg & Barnes, 2008, hereafter GB08). The purpose of the present paper is to take the next steps in modeling the tidal evolution of these binaries. Our goal is not necessarily to accurately reproduce the exact tidal history of any particular pair. Rather, we are aiming to develop a self-consistent general model which can explore a wide variety of physically-plausible tidal histories. Imperfections in the model must be understood in this context.

We will use the Orcus-Vanth binary (Brown et al., 2009) as a case study for investigating the tidal evolutionary histories of KBO binaries. This interesting binary is the focus of this chapter because this system falls in an intermediate regime between the two types of KBO binaries: Orcus is an intermediate size KBO (500 km radius) with an intermediate binary mass ratio (few percent). While there are indications that this system formed by collision, we show below that it is possible to reproduce the current orbital characteristics by starting on a wider orbit typical of capture binaries. Though the majority of this chapter focuses on this system, many of the results are generally applicable to KBO binaries as well as asteroid binaries (PN09).

Did the Orcus-Vanth system form by collision or capture? To answer this question, we will need to understand tidal evolution of KBO binaries at arbitrary eccentricities and mass ratios. Using the orbital and tidal evolution framework of (Eggleton & Kiseleva-Eggleton, 2001), with modifications relevant to small solid bodies, we can make preliminary investigations into important processes that may have significantly modified the orbital characteristics of KBO binaries since their formation.

We will first discuss the collisional model, including tidal evolution outwards from near the Roche lobe. This is followed by general considerations of tidal evolution inwards from a wider capture-like orbit. We then show how adding perturbations from the Sun can induce Kozai cycles which, combined with tidal friction, can significantly shrink orbital separations. The orbital and tidal evolution model is then introduced, with full model details given in the Appendix. Applying this model to Orcus and Vanth, we find that the current properties of this system can be reached from a wide variety of initial orbits. Finally, we discuss the potentially observable signatures of this evolution and the general implications of our results on the study of KBO binaries.

5.2 Collisional Formation and Tidal Evolution Outwards

5.2.1 Parameters of the Orcus-Vanth System

The total mass of the Orcus-Vanth system was determined from Kepler's third law by Brown et al. (2009) to be $M_{tot} \equiv m_1 + m_2 = 6.36 \pm 0.06 \times 10^{20}$ kg. Stansberry et al. (2008) use thermal modeling of *Spitzer* data to find that the radius of Orcus is about 473 ± 37 km. These authors did not account for the presence of the unresolved satellite, which has a fractional brightness in the visible of about 8% (Brown, 2008). Using this range of radii yields a density for Orcus of $1.4_{-0.3}^{+0.4}$ g cm⁻³, where the error is entirely dominated by the radius error. The albedo of Orcus is about 20%. Assuming that Vanth and Orcus have the same albedos and densities, a brightness ratio of 8% corresponds to a mass ratio of $0.08^{3/2} = 0.023$. However, the albedo of Vanth could be up to 5 times higher or lower than the albedo of Orcus and its density may be lower by a factor of ~ 2 . This leads to a wide range of theoretically possible mass ratios from 0.001 (high albedo, low density) to 0.25 (low albedo, same density). Similarly, the radius of the satellite could range from 60 to 300 kilometers.

While it is unlikely that Vanth occupies either extreme of these ranges, its mass ratio and radius are quite uncertain. Except where noted, we will use the following parameters for the Orcus-Vanth system: $m_1 = 6.21 \times 10^{20}$ kg, $\mu \equiv m_2/m_1 = 0.023$, $R_1 = 473$ km, $R_2 = 134$ km, and $\rho = 1.4$ g cm $^{-3}$. (Note that we use μ for the mass ratio instead of the reduced mass and we reserve the symbol q to mean the orbital periaapse distance.) The orbital parameters determined by Brown et al. (2009) are a semi-major axis of $a = 8985$ km and an eccentricity upper-limit of $e < 0.003$. The current heliocentric orbital parameters are typical for an excited Plutino with $a_{\text{helio}} = 39.3$ AU, $e_{\text{helio}} = 0.222$, and $i_{\text{helio}} = 20.6^\circ$.

In our consideration of tidal evolution, we will also need to estimate the relevant tidal parameters for Orcus and Vanth: the Love number, k_2 (which describes the response of the material to a second-order potential) and the tidal dissipation parameter, Q (which describes the fraction of total energy dissipated during tidal flexure). The value of Q is not well known, but is often assumed to be ~ 100 for terrestrial and icy bodies (Goldreich & Soter, 1966). A standard way for estimating k_2 is to use the relation derived from comparing material strength to self-gravity (Goldreich & Soter, 1966):

$$k_2 \approx \frac{3/2}{1 + \frac{19\mu_r R}{2\rho GM}} \quad (5.1)$$

where μ_r is the rigidity of the body, typically assumed to be 4×10^9 N-m for ice, but which could easily vary by orders of magnitude. Using the nominal parameters, we find that $k_{2,\text{Orcus}} \simeq 0.0048$ and $k_{2,\text{Vanth}} \simeq 0.0004$, e.g., low k_2 values typical of small rigid bodies. For small KBO binaries that are rubble piles, e.g., which have significant void space on the interior, the analysis of Goldreich & Sari (2009) implies that k_2 can be enhanced, particularly when the objects are small ($R \lesssim 100$ km). Many small KBOs are thought to have significant porosity, as inferred from low densities, and tidal evolution may be quite enhanced in these bodies. Orcus and Vanth are relatively large KBOs, so we will neglect these effects.

5.2.2 Tidal Evolution Outwards

Suppose that Orcus-Vanth family formed in a collision. In this sense, the system would resemble the Pluto-Charon system. Canup (2005), who modeled the Pluto-Charon collision in detail, suggested that the normalized angular momentum, $J \equiv L/L'$, is a useful criterion for understanding the formation of a binary, where L is the current orbital and spin angular momentum and $L' \equiv \sqrt{GM_{\text{tot}}R_{12}}$ where R_{12} is the radius of an equivalent spherical object containing the total system mass, M_{tot} . Applying this to the Orcus-Vanth system, assuming that both objects are spinning at the orbital frequency ($P = 9.58$ days) and using the nominal mass ratio, we find $J = 0.1$; the relatively low value (e.g., $J \lesssim 0.4$) indicates that the angular momentum budget can be readily achieved in a sub-catastrophic collision. In fact, the mass ratio and normalized angular momentum of Orcus-Vanth

are very similar to the Earth-Moon system ($\mu_{EM} = 0.012$ and $J_{EM} = 0.11$) for which formation by giant impact is preferred. However, we must note that the full range of possible mass ratios allows for a wide variety of J values from $J \simeq 0.01$ for a high albedo satellite to $J \simeq 0.7$ for a low albedo satellite. This wide range results from the total orbital angular momentum, which generally dominates the spin angular momentum:

$$L_{\text{orb}} = \frac{m_1 m_2}{m_1 + m_2} \sqrt{G(m_1 + m_2)a(1 - e^2)} = \frac{\mu}{1 + \mu^2} M_{\text{tot}} \sqrt{GM_{\text{tot}}a(1 - e^2)} \quad (5.2)$$

where the second equality shows the dependence to the unknown mass ratio. If Vanth's albedo is three times smaller than Orcus, then $q \simeq 0.1$ and $J \simeq 0.37$, which is very similar to the normalized angular momentum of Pluto and Charon; $J_{PC} = 0.38$ using the most recent values for the Pluto-Charon system (Tholen et al., 2008). Canup (2005) finds a variety of SPH models for the giant impact formation of Pluto-Charon that are able to reproduce both the relatively large mass ratio $q > 0.1$ and a normalized angular momentum of $J \sim 0.4$. These models involve equal-mass impactors with high impact parameters and it seems that binaries with $J > 0.4$ cannot be effectively created in non-catastrophic collisions.

In the collision model, Vanth was initially in a nearly circular orbit, coplanar with the equator of Orcus, with a semimajor axis just beyond the Roche limit ($\sim 3R_p$). As in the case of Haumea, the post-collision Orcus should be rapidly rotating from the collision. Tidal torques would then transfer angular momentum from Orcus' spin to the binary orbit. (Vanth's spin angular momentum is also contributed to the orbit, but this effect is relatively small.) Vanth's orbit would continue to expand until the spin rate of Orcus reached the orbital frequency and Orcus and Vanth attained the double synchronous state (DSS). Most systems tidally evolve towards DSS, though it may not be a stable end-state for some systems (e.g., when the spin rate is slower than the initial orbital frequency, in which case the end state is often an inward spiral). Whether DSS is actually achieved during the age of the solar system depends on the rate of tidal evolution. Since the rate of semi-major axis evolution is proportional to the mass ratio, binaries with large satellites (like Pluto-Charon, which is in DSS) tend to reach DSS more rapidly than binaries with small satellites (like the Earth-Moon system, which would take ~ 50 Gyr to reach DSS).

Using the nominal values for Orcus and Vanth, the standard equation for semi-major axis evolution (MD99) can be integrated to show that for Orcus and Vanth, DSS is reached in about Q times 3 million years, similar to Pluto-Charon (Dobrovolskis et al. 1997). This speed is only slightly modified by using different tidal models. Eccentricity damping and obliquity decay are also very rapid, which can be shown analytically and which we have verified with direct simulations. In other words, if Vanth were formed in a collision, then for a reasonable set of tidal parameters, we would expect to see the system today in a circular orbit with the spin angular momenta aligned with the orbital

angular momentum, and rotation rates equal to the orbital period of 9.58 days. If the Orcus-Vanth mass ratio is smaller than the nominal value, it can take much longer to reach DSS.

It is important to note that, if one or both of the binary components are spinning supersynchronously, tides can increase the eccentricity of the mutual binary orbit (e.g., Goldreich & Sari, 2009). Even collisional systems that started evolution with small semi-major axes could plausibly have large non-zero eccentricities due to tides. As tides continue to damp energy, however, the spins of the components slow and eventually reach a phase where tides reduce the eccentricity and the orbit will damp back to circularity. Since KBO systems may be in the intermediate regime, the observation of an eccentric orbit does not rule out formation by collision.

Is there observational evidence that Orcus and Vanth are in the double synchronous state? Unlike the Pluto-Charon system, the current configuration of Orcus and Vanth are such that the orbit pole is pointing nearly at Earth. If the rotation pole is aligned with the orbit pole, rotational photometric variability due to a variegated surface or aspherical shape would be negligibly small from our viewing angle. This is consistent with light curve measurements of Sheppard (2007) who find no variability in the light curve. Rabinowitz et al. (2007) report an unusually-shaped large-amplitude ($\Delta m \simeq 0.18$) light curve for Orcus, though their results may suffer from aliasing due to observing cadence of a long-duration observational campaign. Future more in-depth observations will be needed to clarify these results. If correct, the lack of photometric variability from Orcus is consistent with the expected pole-on orientation. Since the tidal timescale at the current separation is so short compared to the age of the solar system, it would require an unusual formation or tidal history to explain an Orcus-Vanth system that is not currently in the double synchronous state.

5.3 Tidal Evolution Inwards

Even if Orcus and Vanth are currently in the double synchronous state, this does not rule out tidal evolution from larger capture-like orbits. Since tidal evolution can shrink semi-major axes and damp eccentricities, it is possible that KBO binary orbits were wider and more eccentric in the past (GB08). Since an initial formation by capture (and subsequent dynamical friction) is inferred for other wide KBO binaries, it is not precluded in the case of Orcus and Vanth. However, a consideration of how these initial conditions were obtained is beyond the scope of this paper. In particular, the orbital and tidal evolution of KBO binaries while they are still in the dense planetesimal disk is not addressed. Our initial conditions start after the end of dynamical friction when the KBO binary has obtained its current heliocentric orbit, billions of years ago.

Under the capture formation model (e.g., Goldreich et al., 2002; Astakhov et al., 2005; Lee et al., 2007; Schlichting & Sari, 2008a), Orcus and Vanth would have originally been on independent heliocentric orbits in the primordial planetesimal disk. Upon entering one another's Hill sphere,

either dynamical friction due to small bodies or the passage of another large body removes enough energy to permanently bind the two objects together. Subsequent dynamical friction can continue to remove energy from the binary, significantly shrinking the semi-major axis from $a \sim R_H \simeq 4000R_p$, the minimum Hill radius of Orcus-Vanth, to $a \simeq 18R_p$ seen today. As the orbital evolution of binaries during the dynamical friction phase has not been studied in detail, a wide variety of final configurations are theoretically plausible. These will correspond to the initial conditions before tidal evolution. In particular, we will consider initial conditions that resemble known KBO binary orbits: semi-major axes of several tens of primary radii and a wide range of eccentricities and inclinations (Noll et al., 2008a; Grundy et al., 2009).

There are a few general conclusions that can be drawn about the past orbital history of KBO binaries by making the reasonable assumption that tides conserve total angular momentum and that other processes acting on KBOs are not important for the angular momentum budget. (Including the effect of the Sun can lead to a non-conservation of angular momentum of the KBO binary and are discussed below; perturbations from passing KBOs may also be important.) Setting aside spin angular momentum, the orbital angular momentum of a binary is given by Equation 5.2 above. If orbital angular momentum is conserved, then $a(1 - e^2) = a(1 - e)(1 + e)$ is conserved and the initial periape distance $q_{\text{init}} = a_{\text{init}}(1 - e_{\text{init}})$ must be smaller than the current periape as long as a has decreased. Including now the effect of spin angular momentum, we note that, although KBO spin periods are still not well characterized, formation arguments and observational evidence (Sheppard et al., 2008) support the idea that KBOs are not slow rotators compared to the typical binary orbit periods. So when a KBO binary forms, there is usually significant angular momentum in the spins of the components which can be transferred to the orbit over time through tidal torques. As long as these spins have some component in the prograde direction, the initial orbital angular momentum is smaller than seen today, which implies that the initial periape distance must lie even closer than the case where spins are not considered. In other words, for an initial capture orbit to evolve into an orbit with smaller semi-major axis, the initial periape must generally be closer than the current periape and sometimes much closer, which we have also observed numerically in our model (described below). This limits the range of initial orbits that will evolve due to tides into the currently observed orbit.

5.4 Kozai Cycles with Tidal Friction

Based on the discussion above, if the initial orbit of Orcus and Vanth had a large semi-major axis typical of capture-like binaries (a/R_p of 50-100), this initial orbit should have had a periape lower than the current periape $q = 19R_p$. This implies quite large initial eccentricities, e.g., $0.6 \lesssim e \lesssim 0.9$. It is not clear whether the gravitational capture and subsequent dynamical friction or other

perturbations can readily generate such large eccentricities and low periapses.

Secular perturbations due to the Sun can sometimes create large eccentricities and low periapses through Kozai oscillations (PN09). Kozai oscillations or Kozai cycles are large variations in eccentricity and inclination which can occur when the relative inclination between the heliocentric orbit and the binary mutual orbit, referred to as i throughout this paper, exceeds a critical value (typically $40^\circ \lesssim i \lesssim 140^\circ$) as originally pointed out by Kozai (1962) and Lidov (1962). These oscillations cause the eccentricity and inclination of the KBO binary to exchange on long timescales (set by the specific parameters of the system), while keeping $\sqrt{1 - e^2} \cos i$ constant (Kozai, 1962).

It is useful to consider a coordinate system centered on the barycenter of the KBO binary orbit. In this system, the Sun's orbit about the binary is just the heliocentric orbit of the binary about the Sun. Averaging over the orbit of the Sun in the quadrupole approximation (higher order terms are very small for KBO binaries; Ford et al., 2000), the amplitude of Kozai oscillations depends on the initial relative inclination and binary KBO eccentricity, while the mass and distance of the third body perturber are only important in setting the Kozai oscillation timescale (Kiseleva et al., 1998):

$$\tau_{\text{Kozai}} \simeq \frac{2}{3\pi} \frac{P_{\text{helio}}^2}{P} (1 - e_{\text{out}}^2)^{3/2} \quad (5.3)$$

Including the effect of Kozai oscillations in the evolution of KBO binaries is important because many KBO binaries are subject to these oscillations (PN09) and *the high eccentricity phases of these oscillations can significantly lower the periapse distance, leading to strong tidal evolution of otherwise distant bodies*. This effect is known as Kozai Cycles with Tidal Friction (KCTF) and may be an important way of modifying KBO binaries, as it is for close stellar binaries and some hot Jupiter exoplanets (Mazeh & Shaham, 1979; Kiseleva et al., 1998; Fabrycky & Tremaine, 2007).

KCTF is an effective way of reducing orbital size and works in the following way. A wide KBO binary starts out with a periapse too high for significant tidal evolution, but at a significant relative inclination, i , to the binary's heliocentric orbit. Kozai oscillations due to the perturbations of the Sun cause an increase in eccentricity which can in many cases lead to quite small periapse distances during the maximum eccentricity phase. During the high eccentricity phases, tidal damping at periapse is significantly enhanced, which shrinks the orbit, but may not initially affect Kozai oscillations. This process continues until the periapse is low enough that apsidal precession due to other sources of apsidal precession are strong enough to suppress Kozai cycles (see below) and the orbit freezes near its high eccentricity state. Continued damping circularizes the orbit near the periapse position, leading to a circular orbit at a much smaller semi-major axis than the original orbit. KCTF can significantly lower the orbital periapse as it avoids the angular momentum argument described above: Kozai oscillations only conserve the z component of the binary's orbital angular momentum and smaller final orbits can be made by simply changing the initial inclination.

There are three requirements that KCTF must meet in order to significantly shrink a binary orbit. First, the initial relative inclination and eccentricity must fall in the regime where Kozai oscillations are significant: typically $40^\circ \lesssim i \lesssim 140^\circ$, though this range can be broadened somewhat in the presence of non-zero initial eccentricity. This is true of many KBO (and asteroid) binaries (PN09), including Orcus and Vanth, which currently have a relative inclination of $i \simeq 66^\circ$. Second, the minimal periaapse achieved by the Kozai cycle must be in a range where tidal forces (which depend on the radii, Love numbers, and tidal Q values) between the two objects are significant. Otherwise, the eccentricity and inclination simply oscillate without any long-term trend. There are probably many KBO binaries that fall in this regime and we note that even with tides are not important, KBO binary orbits can be significantly modified due to the Kozai effect.

Finally, additional minor perturbations to the orbital orientation must be small because Kozai cycles are caused by very slight perturbations that add coherently on secular timescales. In particular, the change in eccentricity due to the Kozai effect, $\dot{e} \propto \sin 2\omega$, can be averaged to zero if ω is precessing too quickly. Even in the presence of minor additional apsidal precession, the weak third-body perturbations are inefficient and Kozai cycles are suppressed. It can be shown analytically and numerically that if the periaapse precession period due to other perturbations is shorter than the Kozai cycle timescale (Equation 5.3) by more than a factor of ~ 2 , the Kozai effect is significantly suppressed (Fabrycky & Tremaine, 2007). That is, in the presence of additional apsidal precession, the amplitude of eccentricity and inclination oscillations is quickly minimized, preventing KCTF. (Such suppression also significantly shortens the period, by as much as an order of magnitude, of any residual Kozai oscillations.)

Additional satellites are very effective at suppressing Kozai cycles (e.g., Innanen et al., 1997, but see Takeda et al., 2008), so KCTF cannot directly form the Haumea or Pluto multiple systems, though these are both in the Kozai inclination regime. For solid body binaries without additional satellites, the dominant source of apsidal precession is usually due to a permanent quadrupole moment (characterized by J_2) of the primary and/or secondary. We define this J_2 as the quadrupole due only to permanent asymmetry supported by the non-zero material strength of KBOs, i.e., it is the non-hydrostatic component of the gravitational quadrupole. The fluid quadrupole of tidal and rotational bulges is taken care of through additional terms, though we find that these quadrupoles are only important if the permanent asymmetry is extremely small (see Appendix). This work extends the preliminary analysis of PN09, who considered purely fluid bodies, by including precession due to J_2 and the resultant suppression of Kozai cycles.

Whatever the source of additional precession, the effect is to reduce the e and i amplitude of Kozai oscillations, potentially disabling KCTF. When $\dot{\omega}_{\text{others}} \tau_{\text{Kozai}} \gg 1$, Kozai cycles are effectively turned off. When $\dot{\omega}_{\text{others}} \tau_{\text{Kozai}} \ll 1$, then Kozai cycles are unimpeded and the amplitude is determined by only the initial eccentricity and inclination. Again, note that the mass and distance of the Sun do

not effect the amplitude of Kozai cycles, but only the period of oscillation (approximately the same as τ_{Kozai}). When $\dot{\omega}_{\text{Kozai}}\tau_{\text{Kozai}} \sim 1$, then the amplitude of Kozai cycles is attenuated. In this case, a full dynamical model (used below) is generally needed to determine whether KCTF can significantly shrink and circularize binary orbits.

Besides the importance of Kozai oscillations and KCTF, the perturbations of the Sun play another important role that affects the spin and orbital evolution of KBO binaries. Since the Sun induces additional apsidal and nodal precession of the KBO binary, including the Sun changes the equilibrium spin states of the system, generally known as Cassini states. For more information on Cassini states, see, e.g., Peale (1974) or Fabrycky et al. (2007). There are multiple equilibrium positions for each spin axis called Cassini states 1-4 which depend strongly on all sources of orbital precession. Tidal evolution will quickly bring the spin axes to one of these states (though state 3 is unstable to further tidal evolution). Unless the obliquity is 0° , bodies in Cassini states still raise tidal bulges and the resulting orbital evolution modifies the location of the Cassini states themselves (Fabrycky et al., 2007). The obliquities of the bodies at any particular time, then, depend on the initial conditions and the amount of tidal evolution. In the absence of the Sun (but keeping precession due to J_2 and rotational and tidal bulges) and in the presence of significant tidal dissipation, the equilibrium obliquity between the spin axis and the binary mutual orbit axis will eventually end up in Cassini state 1 with a nearly zero obliquity (Fabrycky et al., 2007). In our integrations, we have found that including a highly-inclined Sun tends to drive the system into high-obliquity Cassini states, sometimes with very large obliquities (even greater than 90°). Though these high-obliquity Cassini states are unstable on very long timescales, the rate of tidal evolution is strongly affected after capture into a Cassini state, and including the spin evolution of the bodies is important for capturing the correct evolution. Note that solar modifications of Cassini States can be important at any relative inclination, independently of Kozai oscillations. Though beyond the capability of current observations, precise measurements of the spin poles of KBO binary components could reveal non-zero Cassini obliquities, which would constitute an indirect measurement of the value of J_2 .

5.5 Orbital Evolution Models

We have shown above that an orbital and tidal evolution model appropriate for KBO binaries require both validity at arbitrary eccentricity and the ability to include the effects of the Sun.

Let us now discuss specific tidal evolution models. The only attempt of which we are aware to investigate the tidal evolution of KBO binaries in high eccentricity orbits is that of GB08. These authors point out the important possibility of tidal evolution from a capture orbit for Dysnomia, the small moon of dwarf planet Eris (Brown & Schaller, 2007). Though our work supports their general conclusion, that tidal evolution inwards could create the tight circular orbit of Dysnomia,

there are some serious flaws in the tidal model they employ (GB08 Equation 1). The tidal evolution equations used are taken from Jackson et al. (2008) (not including minor corrections mentioned by Jackson et al., 2009), who combined tidal evolution equations from Kaula (1968) and Goldreich & Soter (1966). One unincorporated aspect of the original equations is the well-known change in sign of the tidal evolution depending on whether the binary orbital period is supersynchronous or subsynchronous with respect to the spin rate. The evolution of spin rates (and conservation of total angular momentum) is not considered at all. Finally and most importantly, the equations used neglect eccentricity terms of order e^4 and higher, as well as non-zero inclinations. At moderate eccentricities ($e \gtrsim 0.2$), these "higher-order" terms actually dominate the evolution because the coefficients of these terms are much larger than 1. For example, Wisdom (2008) finds that the energy dissipation rate (related to the eccentricity damping rate) is enhanced over the rate predicted by GB08 by a factor of 10^4 at $e \simeq 0.8$, the initial eccentricity estimated by GB08 for Eris and Dysnomia. The reason for this enhancement is to account for the fact that the strength of tidal interactions is a strong function of separation, e.g., r^{-6} . When computing the total torque averaged over one orbital revolution, $\langle r^{-6} \rangle$, it is clear that interactions at periastron $q = a(1 - e)$ completely dominate the evolution, even when accounting for the fact that the satellite spends the least time near periastron. To adequately account for this physical phenomenon requires keeping higher order eccentricity terms; otherwise, substituting $a \approx r$ massively underestimates the strength of tides in highly elliptical orbits (e.g., Kaula, 1964; Mignard, 1980; Eggleton & Kiseleva-Eggleton, 2001; Wisdom, 2008).

GB08 justify the choice of low-eccentricity equations by correctly noting that tidal dissipation at large eccentricities is not well understood (some issues involved in high- e dissipation are discussed in Appendix A below). However, their model does not avoid this problem: it is simply a model in which all the eccentricity coefficients of order higher than 2 have coefficients equal to exactly zero, which does not capture the importance of tidal dissipation at periastron discussed above. Although these authors are correct in pointing out that tidal evolution from large semi-major axes can result in circular orbits, they actually underestimate significantly the tidal damping time.

We choose a different tidal evolution model to describe the orbital history. The equations of Eggleton & Kiseleva-Eggleton (2001, hereafter EKE) are used as the framework to model the full orbital and spin evolution of the binary system. The evolution equations are more fully described in Appendix A, with only the most relevant points explained here. The EKE model uses the equilibrium tide model to calculate the rate of tidal evolution and is valid at any mass ratio and eccentricity (though at the very highest eccentricities, when pericenter orbital frequency rivals solid body oscillation frequencies, a dynamical tide model may be more appropriate than the equilibrium tide model). Since the spin evolution is also tracked, the effects of non-zero obliquity, spin orientation, and spin rate are all accounted for, accurately including the appropriate direction of tidal evolution for subsynchronous, synchronous, and supersynchronous orbits.

These equations describe the secular evolution obtained after averaging over the orbital period, e.g., it does not contain any dependence on the orbital phase. Throughout the integration, the EKE equations describe the evolution of the apsidal and nodal precession of the orbit, the evolution of the semi-major axis and eccentricity, and the orientation of the spins of both bodies in inertial space. As presented, the EKE equations include the effects of the rotational and tidal bulges of both bodies, general relativity, perturbations from a distant third body (averaged over the orbit of that body to the quadrupole order), and tidal damping. Though the EKE equations were derived for stellar systems (hence the inclusion of general relativity), it can easily be extended to other binary systems as it makes no assumptions about the masses (or relative masses) of the three bodies. Integration of the EKE equations self-consistently accounts for Kozai oscillations, Cassini states, and tidal evolution, though there are some issues with the tidal evolution model used (see Appendix).

We have modified the EKE equations to be more appropriate for Kuiper belt binaries; see the Appendix for the full description of the model. We have added the effect of a gravitational quadrupole due to permanent asymmetry in a solid body, characterized in terms of an effective J_2 . For the vast majority of KBOs, this additional J_2 term will dominate the rate of apsidal and nodal precession. Hence, the inclusion of J_2 is very effective at suppressing Kozai oscillations.

We have also restructured the tidal dissipation terms in terms of tidal dissipation parameter Q , as appropriate for solid bodies (Fabrycky et al., 2007). The EKE model also calculates perturbations to the binary orbit due to a distant third body and we have added the effect of the Sun on these binary orbits. The influence of the Sun can make major modifications to the orbital and tidal evolution of KBO binaries, as described above.

5.6 Application of KCTF Model to Orcus-Vanth

One of the most important, but unknown, properties of Orcus and Vanth is J_2 . Since the current orbit is very nearly circular ($e < 0.003$ Brown et al., 2009), it is reasonable to assume that Kozai cycles are suppressed in the current system. We find that increasing apsidal precession by adding a permanent asymmetry of Orcus of $J_2 \simeq 4 \times 10^{-6}$ is sufficient to suppress Kozai cycles in the currently observed system. This J_2 corresponds to moving only a few meters of material from the pole to the equator of a perfectly spherical object; the actual value of J_2 is probably much higher. One source of permanent asymmetry may be a frozen-in rotational bulge from early formation that has not relaxed. We can estimate J_2 from such a bulge using $J_2 = k_2 q_r / 3$ where $q_r = \nu^2 R^3 / GM$, ν is the spin frequency, and k_2 here is the Love number of the body before the bulge freezes. The initial rotation rate was probably somewhat near breakup (2.9 hour spin period) where $q_r \approx 1$, easily yielding J_2 as high as ~ 0.001 or higher. Unfortunately, there is no clear way to estimate the J_2 of KBOs, whose shapes are very poorly known. Again, we point out that our use of J_2 is to

represent the non-hydrostatic quadrupole moment due solely to the permanent asymmetry; this is not necessarily the J_2 that would be measured astrometrically by observing apsidal precession in the system unless the permanent asymmetry is the dominant source of quadrupolar precession (which is likely; see Appendix A).

Using our model, we have performed several integrations with a wide variety of initial conditions and subsequent evolutions. This exploration was performed with two goals: 1) to gain a general understanding of the variety of orbital evolution regimes possible and 2) to approximately reproduce the Orcus-Vanth system (circular orbit with $a \approx 9000$ km and $i \approx 66^\circ$) from a much wider initial orbit through KCTF.

To describe the evolution of various systems, it will be useful to define a few quantities: q_{Kozai} , a_{J_2} , q_{min} and q_{tides} . For a particular KBO binary the true values of these quantities depends on a variety of unknown factors and can only be estimated.

If the initial eccentricity is zero, then the minimum periapse achievable is $q_{\text{Kozai}} = a(1 - \sqrt{1 - \frac{5}{3} \cos^2 i_{\text{init}}})$, where i_{init} is the initial inclination; for i_{init} near 90° , the minimum unsuppressed periapse can be made arbitrarily small.

Significant suppression of Kozai oscillations occurs when $\dot{\omega}_{J_2} \tau_{\text{Kozai}} \simeq 2$, evaluated at $e = 0$, which we have verified numerically and matches the result of Fabrycky & Tremaine (2007). Using Equations 5.7 and 5.3 we can estimate the semi-major axis at which point Kozai suppression would begin, a_{J_2} , assuming that J_2 is the dominant source of precession:

$$a_{J_2} \approx (J_2 R^2 R_H^3 (1 - e_{\text{helio}}^2)^{3/2})^{1/5} \quad (5.4)$$

where $R_H \equiv \left(\frac{m_1 + m_2}{3M_{\text{Sun}}}\right)^{1/3} a_{\text{helio}}$ is the Hill radius of the binary. For example, in the Orcus-Vanth system with $J_2 \simeq 0.001$, this yields $a_{J_2} \approx 43R_p$. When $a \simeq a_{J_2}$, Kozai cycles are suppressed, and the actual minimum periapse achieved may be higher than q_{Kozai} . Call the actual minimum periapse achieved in suppressed Kozai cycles q_{min} , which depends mostly on the initial semi-major axis, inclination, and J_2 . Finally, let q_{rtides} be the periapse distance where tidal effects can significantly affect the KBO binary. This will depend mostly on the unknown tidal parameters k_2 and Q .

The values of q_{min} and q_{tides} , along with the initial spin angular momenta of the binary components, are generally the most important parameters in determining the final outcome of orbital evolution. For example, the initial eccentricity, argument of periapse, or longitude of ascending node of the KBO binary do not significantly modify the final orbit achieved. The relative values of q_{min} and q_{tides} can be used to qualitatively describe the early evolution until Kozai cycles are suppressed and further evolution is determined mostly by conservation of angular momentum.

If q_{tides} is much closer than q_{min} , then tides are not strong enough to affect the binary orbit and Kozai cycles proceed unimpeded. This can occur when Q is high (weak tidal dissipation) or J_2 is

high (efficient Kozai suppression).

If, on the other hand, q_{tides} is much higher than q_{min} , then during the course of the first Kozai cycle, the periaapse reaches the regime where tides are important. These tides can shrink the periaapse and quickly bring the semi-major axis below a_{J_2} , turning off Kozai cycles. When tides are not as strong, they can slowly shrink the orbit over several Kozai cycles, eventually reaching a regime where the semi-major axis has been lowered enough to suppress Kozai cycling ($a \lesssim a_{J_2}$). Once the Kozai effect is inactive, tidal evolution occurs according to conservation of angular momentum. As discussed above, damping the eccentricity then leads to an overall increase in periaapse. Furthermore, during Kozai cycles, the spin rates and directions of the two bodies are not strongly affected. So the initial spin angular momentum, now efficiently coupled to the orbit through tides, also acts to increase the semi-major axis and periaapse, as long as the spins are somewhat prograde.

It is interesting to note that the final semi-major axis achieved with KCTF is about the same as the final semi-major axis achieved with tidal evolution outwards from the Roche lobe: in both cases, the final position is located at a distance where tidal effects are important $\sim q_{\text{tides}}$. For the same reason, when tidal evolution at the current position of Vanth is relatively strong, both tidal evolution outwards and tidal evolution inwards have sufficient time in the age of the solar system to produce the binary properties seen today.

When KCTF was active in our integrations, we found a wide variety of possible final semi-major axes, $3R_p \lesssim a \lesssim 30R_p$, with a preference for lower values. One example of a system that, through Kozai Cycles with Tidal Friction, shrinks significantly in semi-major axis is shown in Figure 5.1. Unlike in the case of collisions, tidal evolution inwards from a capture orbit does not produce a binary with a specific value of J . That the observed value of J matches well to the value expected from collision models would be essentially a coincidence if the system tidally evolved inward from a capture-like orbit.

The final inclination of the binary is essentially frozen in when the periaapse is low enough that Kozai cycles become completely suppressed. This often happens when the eccentricity is maximized, which most often occurs when the inclination is near the critical angle, i.e., $i \approx 40^\circ$ or 140° (Fabrycky & Tremaine, 2007). This is the case in the integration shown in Figure 5.1. Higher inclinations can occur when the oscillation amplitudes are suppressed, the initial eccentricities are high, or if tides are particularly strong (when $q_{\text{tides}} \gg q_{\text{min}}$) so that Kozai cycles can be broken before the maximal eccentricity is reached. Note that, when including the aspects of spin evolution, it is possible to have final inclinations outside the Kozai range and it is also possible for prograde orbits to “roll over” and become retrograde orbits. This ability of Kozai cycles to significantly change the inclination distribution of KBO binaries will unfortunately make it difficult to identify the primordial inclination distribution predicted by Schlichting & Sari (2008b).

Our simulations are able to produce Orcus-Vanth binaries in circular orbits with a range of semi-

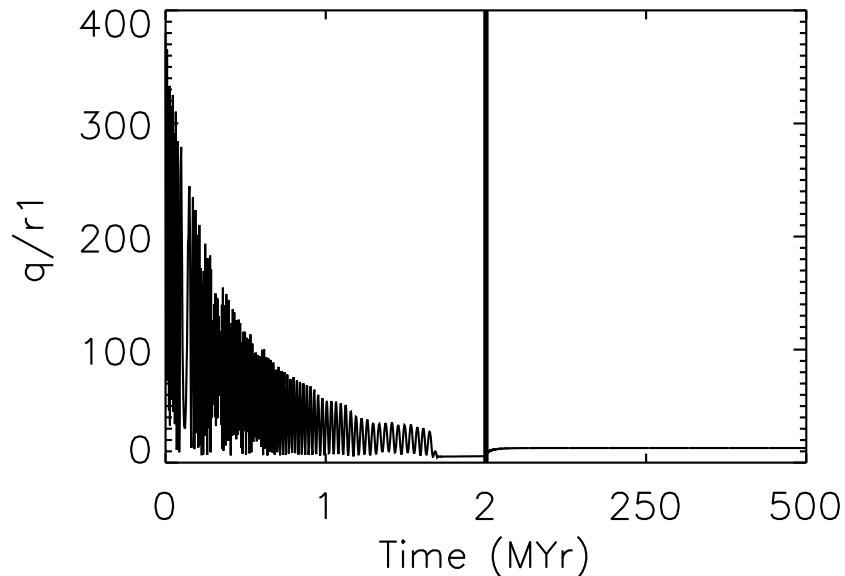


Figure 5.1 **Evolution of the Periapse of a KBO Binary undergoing KCTF.** We used our model for the orbital and tidal evolution of KBO binaries to explore a variety of initial conditions, in order to attempt to reproduce the Orcus-Vanth binary. The time evolution of the periape ($q = a(1 - e)$, q/R_p is shown) for one of our integrations is shown above. Note the difference in the time axis between the left and right side of the graph. In this integration, the physical properties of the binary components matched that of Orcus and Vanth, including a J_2 of 0.0004 and 0.005 respectively. The initial semi-major axis, eccentricity, and inclination were $950 R_p$, 0.6, and 82.7° respectively, so that the initial orbital periape would have been $380 R_p$ or nearly 200000 km. At this separation, tidal evolution is completely negligible. However, because the initial inclination is in the Kozai regime, Kozai cycles significantly modify the eccentricity, allowing the system to reach very low periape values. These Kozai oscillations are initially very rapid and slow as the orbital period shrinks due to tidal evolution, which is effective when the periape reaches $\sim 20 R_p$. Aided by a reduction in periape due to the Kozai cycles, the orbit shrinks significantly, reaching $a \simeq 100 R_p$ within 1.7 MYr. At this point, additional precession from J_2 is able to suppress Kozai cycles and the orbit stabilizes, as always, with a high eccentricity and low periape. In this case, the final inclination is about 34° ; it is typical that Kozai cycles will cease at the highest value of eccentricity, corresponding to the lowest value of inclination (which is usually near the critical inclination of $\sim 40^\circ$). Further evolution is dominated by tidal dissipation, which raises the periape due to conservation of angular momentum (Equation 5.2) until the orbit becomes nearly circular after about 50 MYr. The spins of both components are in Cassini states and the Cassini obliquity damps to nearly zero on the same timescale. The final system looks similar to the Orcus-Vanth binary today, except for the lower mutual inclination (34° instead of 66°). Further exploration of parameter space indicates that reasonable variations in initial conditions could easily increase the final inclination of the simulated Orcus-Vanth to match the observed inclination.

major axes and inclinations that span the observed values. Since the orbital evolution is somewhat chaotic and the parameter space of initial conditions is very large, we have not identified a specific model that reproduces the currently observed system. However, the results we do find give no indication that it would be difficult or impossible to produce this system from capture-like initial conditions during the age of the solar system.

During the tidal dissipation phase of evolution, we have found that the spin state of the primary and/or secondary will typically go to an equilibrium Cassini State. Most tidally-affected bodies in the solar system are in the low-obliquity Cassini state 1, with the notable exception of the Earth’s Moon which is in Cassini state 2. Cassini state 2 is usually available either when the obliquity starts relatively high and/or perturbations from the Sun are relatively strong at large semi-major axes. Many of our integrations put the bodies, especially the primary, in Cassini state 2. This is especially true when J_2 is relatively high. As the eccentricity damps to nearly zero and the semi-major axis shrinks at the expense of spin angular momentum, the primary (or secondary) can sometimes maintain the large Cassini state 2 obliquity for long times. In some cases, there is a phase of KCTF evolution where the orbit is nearly circular, but the angle between the spin of Orcus and the binary orbital angular momentum is still substantial. This is an important observational consequence of KCTF, as Cassini state 2 is not likely to be reached by systems that form in a collision and tidally evolve outward. The converse is not true; that is, if a KBO binary is found to have low obliquity (as may be the case for Orcus) it does not imply that KCTF was not active, e.g., tides may have been sufficiently strong to force the transition into Cassini state 1 (Fabrycky et al., 2007).

5.7 Discussion: General effects of KCTF on KBO binaries

Besides the Orcus-Vanth system, we have also applied our model to the Eris-Dysnomia system, which also has a relative inclination in the Kozai regime: $i \simeq 78^\circ$ or $i \simeq 102^\circ$ in the two possible orbit solutions (Brown & Schaller, 2007). We did not explore this system in detail, but reach the same conclusion as GB08: theoretically, Eris and Dysnomia could have started on a much wider, more eccentric orbit and through Kozai cycles and tidal friction, ended in the orbital orientation seen today. The large heliocentric inclination of Eris ($i_{\text{helio}} = 44.2^\circ$) was presumably created in an early scattering event and illustrates the possibility that changes in the heliocentric orbit of the KBO binary could potentially affect whether the relative inclination (which depends on both the heliocentric inclination and the binary orbit pole direction) is susceptible to Kozai oscillations.

With the current information, it appears that the Orcus-Vanth and Eris-Dysnomia binaries could have formed through either collision or capture. In the future, with more binaries and better observations, the observational signatures of KCTF will be more testable. These signatures include

the following (see also PN09).

- Binaries whose orbits are indicative of KCTF evolution.
- Close binaries on nearly circular orbits with substantial obliquities.
- An underabundance of KBO binaries with relatively large periods and nearly perpendicular inclinations along with an overabundance of short-period binaries with inclinations near the critical Kozai inclination (e.g., Figure 8 of Fabrycky & Tremaine 2007).

We caution that there are significant observational biases present in the current distribution of KBO binaries in that all relative inclinations are not sampled evenly. For example, systems that have low relative inclinations always present nearly edge-on orbits with respect to Earth-based observations, while systems with high relative inclinations are usually face-on as seen from Earth. Since KBO binaries are discovered when the components are significantly separated ($\gtrsim 0.2$ arcseconds) during a single Hubble observation, there is a greater likelihood for edge-on secondaries to be unresolvable when observed at a single random epoch, especially for binary separations near the limiting resolution.

On the other hand, for some specific KBO systems, it will be possible to rule out KCTF as an important source of orbit modification. This is most easily done with the observation of an additional satellite, both because these satellites suppress Kozai oscillations and also because they limit the orbital evolution possible under the reasonable assumption that satellite orbits never crossed in the past. This rules out the evolution of satellites of Pluto and Haumea by KCTF alone (but see the “orbital collision” model below). The presence of an extant collisional family like the Haumea family (Brown et al., 2007) would be another clear sign that the binary was formed by a collision that occurred after the Kuiper belt attained its current structure. Finally, with long-term astrometric observations of some binary systems, a direct detection or upper limit of J_2 can provide insight into the likelihood of past evolution due to KCTF.

Tidal dissipation (inwards or outwards) of the orbital and rotational energy of KBO binaries only produce minor temperature enhancements; for the Orcus-Vanth binary, the average temperature increase due to orbital energy is less than 1 Kelvin while the average temperature increase due to spin energy could have been as high as 10 Kelvin. Smaller KBOs will dissipate even less energy. Since this energy is deposited over very long timescales, tidal dissipation generally has little effect of the thermal properties of KBOs and binaries that evolved inwards or outwards will not have identifiable surface features due to tidal heating. On the other hand, giant impacts can strongly affect the interior and surface states of these systems, though the unique observable consequences of such collisions is unclear.

We hypothesize that a hybrid scheme of KCTF-induced collisions may be possible and important for forming KBO binaries. In this case, KCTF increases the eccentricity and drops the periape to

very low values, as long as Kozai cycles are not suppressed (e.g., $a \gtrsim a_{J_2}$). Even for very low J_2 values, this generally occurs at periapses above the Roche limit, unless a is very large (hundreds of primary radii). In these very high eccentricity phases, it may be possible for the orbit to evolve to an unstably low periapse. This may be assisted by small non-tidal perturbations, e.g., passing or impacting KBOs, which could lower the periapse beyond that achieved by Kozai cycles alone. Once the periapse descends into the Roche lobe, an equilibrium tidal model fails, but it seems unlikely that continued interactions between objects on highly elongated orbits with very low periapses will be able to avoid eventual collision. Unlike a collision between two unbound objects, the relative velocity of the bodies in such an “orbital collision” is lower than the escape velocity from the primary by a factor of about $\sqrt{\frac{1+e}{2}}$. Such a grazing weak collision can still result in a disk from which new satellites would coalesce; these satellites may then evolve outwards due to tides.

It is interesting to note that such a formation mechanism is apparently consistent with the successful simulations of Canup (2005), which explored the giant impact that produced the Pluto-Charon system using a Smoothed Particle Hydrodynamics method. Canup (2005) found an entire suite of simulations between equal size objects on trajectories with $v_{imp} = v_{esc}$ and nearly grazing impact parameters ($0.83 < b < 0.96$) that successfully produced disks or intact moons with the angular momentum and mass ratio that would evolve into the current Pluto-Charon system. These are similar to the impact parameters that would result from a decaying highly eccentric orbit. It is interesting to note that the prevalence of KBO capture binaries of nearly equal masses, coupled with the likelihood of Kozai cycles at high relative inclinations may imply that such orbital collisions are not uncommon. Furthermore, this method naturally produces impact velocities near the mutual escape velocity, regardless of the surrounding dynamical environment. (The orbital collision model is not favored for binaries where the inferred impact velocity is significantly larger than the escape velocity.)

The opposite effect is also possible: KCTF can unbind KBO binaries if the system properties are right. When the initial inclination of a binary is near 90° , the maximal eccentricity reached due to Kozai oscillations can be very high. Goldreich (1963) pointed out that tidal effects on very high eccentricity orbits are likely to increase both the semi-major axis and the eccentricity. In our integrations, we found that KCTF can occasionally lead to orbits that quickly increase in semi-major axis and eccentricity, gaining angular momentum from the spins of the component until the binary disassociates. This is the tidally-evolved extension of the “Kozai-Hill” instability mechanism of PN09, who note that high eccentricity phases of Kozai oscillations can lead to orbital apoapse distances exceeding the Hill radius.

5.8 Conclusions

There is strong circumstantial evidence that Orcus’s satellite Vanth formed in giant collision. Here we have proposed an alternative explanation for the current orbital state: starting on a wider capture-like orbit, Kozai perturbations due to the Sun cause the eccentricity (and inclination) to oscillate with large amplitudes, occasionally bringing the periaapse low enough to be affected by tidal evolution. This process continues until tidal dissipation brings the periaapse low enough to suppress Kozai oscillations, after which the orbit circularizes and the spin angular momenta of Orcus and Vanth are converted to orbital angular momentum. Similar processes may be important for a wide variety of KBO binaries. Kozai Cycles with Tidal Friction (KCTF) may significantly modify KBO binary orbits from their initial distribution.

Though it is difficult to prove or exclude the possibility of KCTF for single systems, the ensemble of KBO binaries may contain the signatures of KCTF evolution, e.g., a lack of wide binaries at relative inclinations near $i = 90^\circ$. More observational and theoretical study of both individual KBO binaries and the entire population will be able to elucidate the importance of KCTF for creating the currently observed distribution. Many of the conclusions we have drawn for KBO binaries are also applicable to asteroid binaries (PN09).

Tidal and orbital evolution can clearly make significant modifications to the primordial binary orbit distribution. Understanding the effect of Kozai oscillations and tidal dissipation on the currently observed properties of KBO binaries will help debias the interpretation of the origins of KBO binaries. In particular, the observation of a short-period circular orbit for Orcus and Vanth can not be immediately attributed to a purely collisional origin.

Acknowledgements: We would like to thank Dan Fabrycky for kindly providing the initial version of the EKE code and for helpful discussions. We also thank Michael Efroimsky, Alejandro Soto, and Aaron Wolf for valuable discussions. This work was supported by NASA Headquarters under the Earth and Space Sciences Fellowship and the Planetary Astronomy programs.

5.9 Appendix: The Orbital Evolution Model

5.9.1 Introduction to EKE Framework

We use the orbital and tidal evolution framework of (Eggleton & Kiseleva-Eggleton, 2001, hereafter EKE), which was originally developed for stellar systems, but with the minor adaptations described below, can be applied to solid body binaries. For more information on this framework, see Eggleton et al. (1998); Mardling & Lin (2002); Fabrycky & Tremaine (2007); Fabrycky et al. (2007). The original unmodified integration code was kindly provided by D. Fabrycky.

The EKE equations describe the evolution of 4 vectors: \vec{e} , \vec{h} , $\vec{\Omega}_1$, and $\vec{\Omega}_2$, which represent

the Laplace-Runge-Lenz eccentricity vector, the orbital angular momentum vector, and the spin vectors of both bodies, respectively. The magnitude of \vec{e} is the eccentricity, e , and the direction points in the direction of periape. The evolution of semi-major axis is evaluated indirectly through $h = \sqrt{G(M_1 + M_2)a(1 - e^2)}$. These coordinate system used to describe these vectors is the orbital orientation of the outer binary, called $(\vec{E}, \vec{Q}, \vec{H})$ in EKE, where \vec{Q} is a vector perpendicular to the eccentricity vector for the outer binary, which is needed to form a perpendicular right-handed triad of unit vectors. In the original EKE formalism, $(\vec{E}, \vec{Q}, \vec{H})$ is not necessarily an inertial reference frame, but since we assume that the heliocentric orbit is fixed (and is not significantly changed by interactions in the KBO binary), this is an appropriate approximation (Fabrycky & Tremaine, 2007).¹ Note that the quantities we are interested in are independent of the reference frame. The EKE equations describe the force and torque couples needed to evolve the 12 components of \vec{e} , \vec{h} , $\vec{\Omega}_1$, and $\vec{\Omega}_2$. As our implementation of the integration uses a variable timestep and automatically stops when the system reaches the double synchronous state (DSS), the time needed to integrate for the age of the solar system varies from a few seconds to days, depending on the initial conditions and parameters of the integration.

There are two modifications made to the EKE equations that are needed to adapt the system for solid bodies. The first is an addition of apsidal and nodal precession terms due to the quadrupole moment of any permanent asymmetry, J_2 . For small solid bodies, material strength can support permanent mass anomalies and significantly non-spherical shapes. The second is writing the tidal dissipation in terms of Q .

5.9.2 Adding Permanent Asymmetries

Expanding a J_2 potential (Murray & Dermott, 2000) and using the notation of EKE, we find

$$X_{J_{2,1}} = \frac{3}{2} J_{2,1} \left(\frac{R_1}{a} \right)^2 \frac{n}{(1 - e^2)^2} \frac{\Omega_{1h} \Omega_{1e}}{\Omega_1^2} \quad (5.5)$$

$$Y_{J_{2,1}} = \frac{3}{2} J_{2,1} \left(\frac{R_1}{a} \right)^2 \frac{n}{(1 - e^2)^2} \frac{\Omega_{1h} \Omega_{1q}}{\Omega_1^2} \quad (5.6)$$

$$Z_{J_{2,1}} = \frac{3}{4} J_{2,1} \left(\frac{R_1}{a} \right)^2 \frac{n}{(1 - e^2)^2} \frac{2\Omega_{1h}^2 - \Omega_{1e}^2 - \Omega_{1q}^2}{\Omega_1^2} \quad (5.7)$$

where $\Omega^2 = |\vec{\Omega}|^2$ and Ω_{1i} is the projection of the spin vector onto axis i , as in EKE; the spin-related terms are used to correctly account for the case of non-zero obliquity. These terms are added to the X_1 , Y_1 , and Z_1 terms of EKE and this procedure is repeated for body 2, which may itself have a J_2 large enough to dominate the precession of the system. In the appropriate limits, these equations

¹We note here that some heliocentric orbits are not fixed in time due to the effects of other planets. In our model, the effects of other planets and passing KBOs are all ignored.

reproduce the expected J_2 evolution. In the set up of the EKE equations, these terms are used to calculate both the torque on the orbit due to the quadrupole and the corresponding back-torque of the orbit onto the quadrupole. Note that this J_2 is due solely to the permanent asymmetry supported by the material strength of these small solid bodies and that the effective J_2 of the tidal and rotational bulges is already accounted for through other terms.

Our prescription for including J_2 assumes that any permanent mass anomalies can be well-approximated by a degree-2 gravity field with an axis aligned with the rotational axis of the body². This is true for rapidly spinning solid bodies, in which case J_2 is an effective time-averaged J_2 , which for a tri-axial body has a value of $J_2 R^2 = 0.1(\alpha^2 + \beta^2 - 2\gamma^2)$, where α , β , and γ are the semi-radii of the ellipsoid (Scheeres, 1994; Ragozzine & Brown, 2009). When the spin frequency and orbital angular frequency at periaapse become comparable, or near higher-order spin-orbit resonances, this approximation begins to break down. Near synchronicity other unmodeled sources of tidal dissipation can become important, though their effect is to change slightly the time needed to achieve DSS (Dobrovolskis et al., 1997).

In the case of high-order spin-orbit resonances, tidal evolution can quickly break these resonances and ignoring them in our evolution should have no significant effect, especially if the final outcome is a circular orbit. We note that many KBO binaries have eccentric orbits: if tides are effective at slowing the spins of these bodies, they may be in high-order spin-orbit resonances. Recall that the purpose of including J_2 in the evolution is to provide a realistic source of natural apsidal precession that can suppress Kozai oscillations; after Kozai effects turn off early in the integration, J_2 has no significant impact on the remaining evolution, as it merely precesses the orientation of the orbit and spin poles. This has no long-term effect on tidal evolution rates outside of resonance.

We can compare the importance of a permanent asymmetry (J_2) and the next largest source of apsidal precession in highly eccentric orbits, which is usually precession due to instantaneous tidal bulges. If the rotation rate is significantly higher than the orbital period, the rotational bulges can be more important, depending on the eccentricity. The Z terms of the EKE framework describe apsidal precession, so we can compare $Z_{J_2,1}$ to the precession rate due to the instantaneous tidal bulge of body 1 (EKE):

$$\dot{\omega}_t = \frac{15}{2} k_2 \left(\frac{R_1}{a} \right)^5 n \frac{m_2}{m_1} \frac{(1 + \frac{3}{2}e^2 + \frac{1}{8}e^4)}{(1 - e^2)^5} \quad (5.8)$$

Considering only body 1 and assuming zero obliquity, it can be shown that these two will be comparable when

$$J_2 \simeq 5k_2 \left(\frac{R_1}{q} \right)^3 \frac{m_2}{m_1} \quad (5.9)$$

where q is the periaapse and where we have dropped the term $\frac{(1 + \frac{3}{2}e^2 + \frac{1}{8}e^4)}{(1+e)^3}$, which is nearly equal to 1 for all eccentricities. Because of the stronger dependence of apsidal precession (of both tidal

²Even small KBOs ($r \gtrsim 1$ km) are expected to rapidly reach principal axis rotation

and rotational bulges) on the distance $\frac{R_1}{a}$, they are only dominant when the periaapse is very low. Note that J_2 and k_2 can easily be of similar magnitude, even when the body is large enough to become spherical through hydrostatic equilibrium. In this case J_2 precession will dominate unless the periaapse is within the Roche lobe at ~ 2.5 primary radii. For stable orbits, J_2 precession will be the dominant source of apsidal precession unless the solid body has very little permanent asymmetry and k_2 is rather large, though recall that significant enhancements to k_2 are possible for small rubble piles (Goldreich & Sari, 2009). Since Kozai oscillations significantly change the orbital orientation, this dominance is robust even when the angle between the spin and binary orbital axis is non-zero (and J_2 precession is reduced). By conducting a large range of short-term integrations of the EKE model, we have confirmed that systems where $J_2 = 0$ can reach minimal periaapses of q_{\min} within the Roche lobe. Including even a tiny permanent asymmetry ($J_2 \simeq 10^{-7}$), suppresses Kozai oscillations and raises the maximal periaapse to outside the Roche lobe. Small bodies ($R \lesssim 200$ km), including most KBOs and all but the largest asteroids have sufficient material strength to defy hydrostatic equilibrium, resulting in very large J_2 values of order ~ 0.1 . We also confirm directly that adding J_2 never lowers the minimum periaapse and always acts to suppress the eccentricity and inclination amplitude of Kozai oscillations, while often increasing the oscillation frequency to ~ 10 times faster than the timescale given in Equation 5.3.

5.9.3 Tidal Q

The other modification appropriate for solid bodies is a change in the way solid body tides are treated. The original EKE formalism uses frictional timescales that can be expressed as a function of the viscous timescale of fluid stars. We modify the tidal friction timescale calculations in a way similar to Fabrycky et al. 2007:

$$\frac{1}{t_{F1}} = \frac{3n}{2} \frac{k_{2,1}}{Q_1} \left(\frac{R_1}{a} \right)^5 \frac{M_2}{M_1} \quad (5.10)$$

and similar equations for body 2 (which has the mass factor $\frac{M_1}{M_2}$). Tidal torques are proportional to t_F^{-1} .

The EKE model of tides assumes that the time lag of all tidal components are equal and constant in time. As discussed in Efroimsky & Lainey (2007), this corresponds to a frequency dependent Q with $Q \propto \chi^\alpha$, where χ is the tidal frequency (e.g., $2|\sqrt{\Omega_1^2} - n|$ for the diurnal tide) and where $\alpha = -1$ corresponds to the frequency dependence assumed by EKE. This same frequency dependence is also used in the model of Mignard (1980) and others. A wide variety of geophysical data for the Earth give $\alpha \simeq 0.3 \pm 0.1$ (Efroimsky & Lainey, 2007) and it is thought that a similar value would be relevant for icy bodies (Michael Efroimsky, personal communication, 2009). Hence, the negative frequency-dependence of Q assumed in the EKE model is unlike the geophysically-motivated positive frequency-dependence of Efroimsky & Lainey (2007) and also unlike the constant Q model of Goldreich & Soter

(1966) on which GB08 is modeled. Different frequency dependences of the component tides is the explanation for differing coefficients in the tidal evolution equations. Note that significant changes in the rotational and orbital frequencies under KCTF can be quite large, so that the value of α is important for determining the exact evolution. We experimented with incorporating a variable frequency dependence ($Q \propto \chi^\alpha$) and found that the main change was usually in the timescale of orbital evolution; as noted in the text, once the system breaks out of the Kozai resonance, the final parameters of the double synchronous state are determined solely by conservation of angular momentum.

Despite possible issues with Q , the EKE model accounts for the fact that, at high eccentricity, significant tidal damping at periaapse enhances the tidal evolution rate over the above (which depends on a). Since the tidal torque is proportional to r^{-6} , the majority of tidal interactions occur near periaapse (even when accounting for the fact that the orbit spends the least time near periaapse). Using the EKE expansions derived for arbitrary eccentricity and obliquity significantly improves the accuracy of evolution over GB08 who use the low-eccentricity approximations of these equations in a regime where they are not valid.

5.9.4 Potential Improvements to the Model

To more accurately track tidal histories, the Kaula (1964) method of expanding the tidal potential into individual Fourier components would be superior. Then, each tide can be assigned the appropriate frequency dependence and the sign of the torque of each individual tidal component can be correctly accounted for. The Kaula (1964) expansion of tidal friction, with corrections and improvements from Efroimsky & Williams (2008), could be readily incorporated in the EKE framework, which would avoid some of the problems relating to tracking the correct inclination reference frame. To do this properly would involve one less averaging than taken in Kaula (1964), to account for the effect of the Kozai resonance on the argument of periaapse, as pointed out in Efroimsky & Williams (2008).

Even this improved model would suffer from the difficulties encountered in all averaged models: they can not correctly handle resonances involving unresolved frequencies. For example, since our model averages over the orbital motion of the Sun, our model ignores the potentially important contribution of the evection resonance, when the orbital precession frequency is resonant with the heliocentric orbital period (Touma & Wisdom, 1998). Passage through this resonance can excite the system and this excitation is not included in our integrations. We do check the apsidal and nodal precession periods throughout our integration and find that these timescales are generally much longer than the heliocentric orbital period when the satellite is tidally evolving inwards. It can be

shown that for a nearly-circular orbit, the evection resonance occurs at a semi-major axis of

$$a_{in} \simeq \left(\frac{27}{4} (J_2 R^2)^2 R_H^3 \right)^{1/7} \quad (5.11)$$

which is about 10 primary radii for the Orcus system, assuming $J_2 \simeq 0.005$. Unless J_2 is much higher, the 1:1 evection resonance is probably not important for tidal evolution inward from a larger orbit.

By far the largest drawback to our tidal model, which would only be partly remedied by using a full Fourier expansion of the tidal potential, is that the physics of tidal dissipation is not fully understood. Although most popular, tidal models that use Q implicitly assume that the bodies respond linearly to perturbations; once tidal stresses significantly exceed the yield stress of the body or if tidal components at different frequencies interact non-linearly, a hydrodynamical model should be used to calculate tidal perturbations. It may be true that the end result of such a model may be approximated by an “effective” Q value with a certain frequency dependence. Very close passes, significant lateral heterogeneity in the binary components, feedback between energy dissipation and tidal parameters, or other non-linear effects are also likely important in reconstructing precise tidal histories. Even in the Earth-Moon system, there is insufficient observational and theoretical data to fully reconstruct the orbital history of the binary system. Despite these drawbacks, we believe that the inclusion of a better tidal model would not change the general result that KCTF can be important for the orbital evolution of KBO binaries. Furthermore, investigations of the orbits of KBO binaries will only provide more constraints and insights into the relevant tidal physics; future analyses may be able to identify and accurately model the most important aspects of the tidal evolution of these systems.

Bibliography

- Astakhov, S. A., Lee, E. A., & Farrelly, D. 2005, *Monthly Notices of the RAS*, 360, 401
- Benecchi, S. D., Noll, K. S., Grundy, W. M., Buie, M. W., Stephens, D. C., & Levison, H. F. 2009, *Icarus*, 200, 292
- Brown, M. E. *The Largest Kuiper Belt Objects (The Solar System Beyond Neptune)*, 335–344
- Brown, M. E., Barkume, K. M., Ragozzine, D., & Schaller, E. L. 2007, *Nature*, 446, 294
- Brown, M. E., Other, A., & Other, A. 2009
- Brown, M. E. & Schaller, E. L. 2007, *Science*, 316, 1585
- Brown, M. E., van Dam, M. A., Bouchez, A. H., Le Mignant, D., Campbell, R. D., Chin, J. C. Y., Conrad, A., Hartman, S. K., Johansson, E. M., Lafon, R. E., Rabinowitz, D. L., Stomski, Jr., P. J., Summers, D. M., Trujillo, C. A., & Wizinowich, P. L. 2006, *Astrophysical Journal, Letters*, 639, L43
- Canup, R. M. 2005, *Science*, 307, 546
- Collins, B. F. & Sari, R. 2008, *Astronomical Journal*, 136, 2552
- Dobrovolskis, A. R., Peale, S. J., & Harris, A. W. *Dynamics of the Pluto-Charon Binary (Pluto and Charon)*, 159
- Efroimsky, M. & Lainey, V. 2007, *Journal of Geophysical Research (Planets)*, 112, 12003
- Efroimsky, M. & Williams, J. G. 2008, *ArXiv e-prints*
- Eggleton, P. P., Kiseleva, L. G., & Hut, P. 1998, *Astrophysical Journal*, 499, 853
- Eggleton, P. P. & Kiseleva-Eggleton, L. 2001, *Astrophysical Journal*, 562, 1012
- Fabrycky, D. & Tremaine, S. 2007, *Astrophysical Journal*, 669, 1298
- Fabrycky, D. C., Johnson, E. T., & Goodman, J. 2007, *Astrophysical Journal*, 665, 754
- Ford, E. B., Kozinsky, B., & Rasio, F. A. 2000, *Astrophysical Journal*, 535, 385
- Funato, Y., Makino, J., Hut, P., Kokubo, E., & Kinoshita, D. 2004, *Nature*, 427, 518
- Goldreich, P. 1963, *Monthly Notices of the RAS*, 126, 257
- Goldreich, P., Lithwick, Y., & Sari, R. 2002, *Nature*, 420, 643
- Goldreich, P. & Sari, R. 2009, *Astrophysical Journal*, 691, 54
- Goldreich, P. & Soter, S. 1966, *Icarus*, 5, 375
- Greenberg, R. & Barnes, R. 2008, *Icarus*, 194, 847

- Grundy, W. M., Noll, K. S., Buie, M. W., Benecchi, S. D., Stephens, D. C., & Levison, H. F. 2009, *Icarus*, 200, 627
- Innanen, K. A., Zheng, J. Q., Mikkola, S., & Valtonen, M. J. 1997, *Astronomical Journal*, 113, 1915
- Jackson, B., Barnes, R., & Greenberg, R. 2009, ArXiv e-prints
- Jackson, B., Greenberg, R., & Barnes, R. 2008, *Astrophysical Journal*, 678, 1396
- Kaula, W. M. 1964, *Reviews of Geophysics and Space Physics*, 2, 661
- . 1968, *An introduction to planetary physics - The terrestrial planets*, ed. W. M. Kaula
- Kiseleva, L. G., Eggleton, P. P., & Mikkola, S. 1998, *Monthly Notices of the RAS*, 300, 292
- Kozai, Y. 1962, *Astronomical Journal*, 67, 591
- Lee, E. A., Astakhov, S. A., & Farrelly, D. 2007, *Monthly Notices of the RAS*, 379, 229
- Lidov, M. L. 1962, *Planetary Space Science*, 9, 719
- Mardling, R. A. & Lin, D. N. C. 2002, *Astrophysical Journal*, 573, 829
- Mazeh, T. & Shaham, J. 1979, *Astronomy and Astrophysics*, 77, 145
- Mignard, F. 1980, *Moon and the Planets*, 23, 185
- Morbidelli, A., Levison, H. F., & Gomes, R. *The Dynamical Structure of the Kuiper Belt and Its Primordial Origin (The Solar System Beyond Neptune)*, 275–292
- Murray, C. D. & Dermott, S. F. 2000, *Solar System Dynamics* (Cambridge University Press)
- Nesvorny, D. 2008, in *AAS/Division for Planetary Sciences Meeting Abstracts*, Vol. 40, AAS/Division for Planetary Sciences Meeting Abstracts, 38.02
- Noll, K. S., Grundy, W. M., Chiang, E. I., Margot, J.-L., & Kern, S. D. *Binaries in the Kuiper Belt (The Solar System Beyond Neptune)*, 345–363
- Noll, K. S., Grundy, W. M., Stephens, D. C., Levison, H. F., & Kern, S. D. 2008b, *Icarus*, 194, 758
- Peale, S. J. 1974, *Astronomical Journal*, 79, 722
- Perets, H. B. & Naoz, S. 2008, ArXiv e-prints
- Rabinowitz, D. L., Schaefer, B. E., & Tourtellotte, S. W. 2007, *Astronomical Journal*, 133, 26
- Ragozzine, D. & Brown, M. E. 2009, *Astronomical Journal*, 137, 4766
- Scheeres, D. J. 1994, *Icarus*, 110, 225
- Schlichting, H. E. & Sari, R. 2008a, *Astrophysical Journal*, 673, 1218
- . 2008b, *Astrophysical Journal*, 686, 741
- Sheppard, S. S. 2007, *Astronomical Journal*, 134, 787
- Sheppard, S. S., Lacerda, P., & Ortiz, J. L. *Photometric Lightcurves of Transneptunian Objects and Centaurs: Rotations, Shapes, and Densities*, ed. M. A. Barucci, H. Boehnhardt, D. P. Cruikshank, & A. Morbidelli, 129–142
- Stansberry, J., Grundy, W., Brown, M., Cruikshank, D., Spencer, J., Trilling, D., & Margot, J.-L. *Physical Properties of Kuiper Belt and Centaur Objects: Constraints from the Spitzer Space Telescope (The Solar System Beyond Neptune)*, 161–179

- Stern, S. A., Bottke, W. F., & Levison, H. F. 2003, *Astronomical Journal*, 125, 902
- Stern, S. A., Weaver, H. A., Steffl, A. J., Mutchler, M. J., Merline, W. J., Buie, M. W., Young, E. F., Young, L. A., & Spencer, J. R. 2006, *Nature*, 439, 946
- Takeda, G., Kita, R., & Rasio, F. A. 2008, *Astrophysical Journal*, 683, 1063
- Tholen, D. J., Buie, M. W., Grundy, W. M., & Elliott, G. T. 2008, *Astronomical Journal*, 135, 777
- Touma, J. & Wisdom, J. 1998, *Astronomical Journal*, 115, 1653
- Weidenschilling, S. J. 2002, *Icarus*, 160, 212
- Wisdom, J. 2008, *Icarus*, 193, 637